

AFIT/DS/ENP/95-J



OPTIMAL WAVEFRONT RECONSTRUCTION FOR A  
COHERENT DIFFRACTED FIELD

DISSERTATION

Presented to the Faculty of the School of Engineering  
of the Air Force Institute of Technology  
Air University  
In Partial Fulfillment of the  
Requirements for the Degree of  
Doctor of Philosophy

William Wolfgang Arrasmith, B.S., M.S.  
Captain

19950811 056

June, 1995

Approved for public release; distribution unlimited

DTIC QUALITY INSPECTED 5

JK

OPTIMAL WAVEFRONT RECONSTRUCTION FOR A  
COHERENT DIFFRACTED FIELD

William Wolfgang Arrasmith, B.S., M.S.

Captain

Approved:

|                            |                |
|----------------------------|----------------|
| <u>Michael C. Ruggmann</u> | <u>5-26-95</u> |
| <u>Ryan M. Wells</u>       | <u>5-26-95</u> |
| <u>Frederick E. Lutz</u>   | <u>5/26/95</u> |
| <u>Mark E. Ooley</u>       | <u>5/26/95</u> |

Robert A. Calico, JR.

Robert A. Calico, JR.

Dean

### *Acknowledgements*

I would like to thank the many people who have provided me with insights, inspiration, and support during the course of this work. I whole-heartedly thank my advisors, Dr.'s Mike Roggemann, Byron Welsh, and Ted Luke, for their guidance and direction and for patiently putting up with my idiosyncrasies. I thank Dr. Dave Voelz and Dr. Paul Idell for sharing their insights with me and helping me through some critical moments. I thank the faculty of the Physics department here at AFIT for encouraging me along the way (special thanks go to Dr. Dave Weeks, Dr. Jeff Martin, Dr. Cliff Dungey and Dr. Bill Bailey). Thanks to Diana, Nancy, and Karen for moral support, great conversation, and giving me a good laugh every once in a while. Thanks, also, to my fellow doctoral students (especially Jeff Druessel and Monte Turner) for acting as sounding boards for my ideas. I sincerely thank my wife, Lena, for her love and understanding and for picking up the slack when times got hectic. I thank my kids, Christina and Kari, and the rest of my family for giving me a perspective on what is really important. Ultimately, I thank God for allowing me the opportunity to come here and do this work.

|                     |  |
|---------------------|--|
| Accession For       |  |
| NTIS                | CRA&I <input checked="checked" type="checkbox"/> |
| DTIC                | TAB <input type="checkbox"/>                     |
| Unannounced         | <input type="checkbox"/>                         |
| Justification ..... |  |
| By .....            |  |
| Distribution /      |  |
| Availability Codes  |  |
| Dist                | Avail and/or Special                             |
| A-1                 |  |

William Wolfgang Arrasmith

## *Table of Contents*

|   | Page |
|---|------|
| Acknowledgements . . . . .  | iii  |
| List of Figures . . . . .   | vi   |
| Abstract . . . . .  | xv   |
| I. Introduction . . . . .   | 1    |
| 1.1 Problem Statement . . . . .   | 1    |
| 1.2 Overview . . . . .  | 1    |
| 1.3 Summary of Significant Contributions and Results . . . . .          | 7    |
| 1.4 Overview of Dissertation . . . . .                                  | 8    |
| II. Background . . . . .  | 11   |
| 2.1 Sheared Coherent Interferometric Photography . . . . .              | 11   |
| 2.2 Conventional Least Squares Reconstructors . . . . .                 | 17   |
| 2.3 Image Formation and Measurement Plane Statistics . . . . .          | 22   |
| III. Theory . . . . .   | 30   |
| 3.1 Phase Reconstructor and Generalized Error Metric . . . . .          | 31   |
| 3.2 Measurement Plane Phase Covariance . . . . .                        | 35   |
| 3.3 Minimum Variance Reconstruction Matrix . . . . .                    | 36   |
| 3.4 Reconstruction Matrix for New Least Squares Reconstructor . . . . . | 37   |
| 3.5 Minimum Variance Implementation and Testing . . . . .               | 40   |
| 3.6 Additive Noise . . . . .  | 51   |

|  | Page |
|--|------|
| IV. Results . . . . .                              | 53   |
| 4.1 Reconstructions of Smooth Objects . . . . .    | 58   |
| 4.2 Simple Diffuse Reflector . . . . .             | 64   |
| 4.3 Extended Diffuse Reflectors . . . . .          | 68   |
| 4.4 Performance and Sensitivity Analysis . . . . . | 89   |
| 4.5 Summary . . . . .                              | 117  |
| V. Conclusions . . . . .                           | 119  |
| 5.1 Results and Conclusions . . . . .              | 119  |
| 5.2 Contributions . . . . .                        | 123  |
| 5.3 Future research directions . . . . .           | 124  |
| Bibliography . . . . .                             | 127  |

## *List of Figures*

| Figure |   | Page |
|--------|---|------|
| 1.     | Illumination geometry. . . . .  | 12   |
| 2.     | Measurement plane grid. . . . .   | 18   |
| 3.     | Branch cut in measurement plane phase. . . . .  | 21   |
| 4.     | Object to Measurement Plane Coordinate System. . . . .  | 24   |
| 5.     | Modeling process. . . . .   | 42   |
| 6.     | (a) True phase and (b) reconstructed phase for deterministic off-axis point source object. . . . .  | 46   |
| 7.     | Off-axis point source phase error squared. . . . .  | 47   |
| 8.     | (a) True phase and (b) reconstructed phase for double point source object with $1.7333 \mu\text{rad}$ separation. . . . .                                   | 49   |
| 9.     | Double point source (a) true image and (b) reconstructed image for point source separation of $1.7333 \mu\text{rads}$ . . . . .                             | 50   |
| 10.    | Average reflectivity distribution for $1.7333 \mu\text{rad}$ deterministic doughnut object. . . . .   | 59   |
| 11.    | Measurement plane phase maps of (a) true phase and (b) reconstructed phase for $1.733 \mu\text{rad}$ deterministic doughnut object. . . . .                 | 60   |
| 12.    | Plots of (a) true image and (b) reconstructed image for $1.733 \mu\text{rad}$ deterministic doughnut object. . . . .  | 61   |
| 13.    | Average reflectivity for $1.733 \mu\text{rad}$ deterministic tri-bar object. . . .  | 62   |
| 14.    | Measurement plane phase maps of (a) true phase and (b) reconstructed phase for $1.733 \mu\text{rad}$ deterministic tri-bar object. . . . .                  | 63   |
| 15.    | Image plane maps of (a) true image and (b) reconstructed image for $1.733 \mu\text{rad}$ deterministic tri-bar object. . . . .                              | 64   |
| 16.    | Average reflectivity distribution for a random double point source object with $0.8667 \mu\text{rad}$ separation. . . . .                                   | 65   |
| 17.    | Measurement plane phase maps of (a) true phase and (b) reconstructed phase for $0.8667 \mu\text{rad}$ separation random double point source object. . . . . | 66   |

| Figure  | Page |
|---|------|
| 18. (a) True image and (b) reconstructed image for random double point source object with $0.8667 \mu\text{rad}$ separation. The measurement plane sampling density was 8 by 8 evenly spaced samples in a 3 m by 3 m square collecting aperture. The number of independent image frames used to average was 1. . . . .  | 67   |
| 19. (a) True image and (b) reconstructed image for random double point source object with $0.8667 \mu\text{rad}$ separation. The measurement plane sampling density was 8 by 8 evenly spaced samples in a 3 m by 3 m square collecting aperture. The number of independent image frames used to average were 100. . . . .   | 68   |
| 20. Overlay of true image slice and reconstructed image slice for random double point source object with $0.8667 \mu\text{rad}$ separation. The number of independent image frames used to average were 100. . . . .  | 69   |
| 21. True (a) and reconstructed image (b) for extended random object with Gaussian average reflectivity profile . . . . .  | 70   |
| 22. Minimum theoretical aperture averaged mean squared phase error for minimum variance (solid line) and least squares (long dashes) formalisms. Also included is the aperture averaged input phase variance (short dashes). Gaussian average reflectivity profiles with infinite spatial extent were used in determining the theoretical aperture averaged mean squared phase error for all values of $\beta$ . . . . .  | 71   |
| 23. Aperture averaged mean squared phase error for theoretical (lower solid line) and simulated (long dashes) minimum variance results. Aperture averaged mean squared phase error for theoretical (dash dot) and simulated (upper solid line) results for the new least squares reconstructor. The aperture averaged input phase variance is also shown (dotted line). The reference phase map was used to provide the phase differences. Gaussian average reflectivity profiles with infinite spatial extent were used in both the theoretical and simulated determination of the aperture averaged mean squared phase error. The horizontal axis is the sampling parameter, $\beta$ . The measurement plane sampling density was 8 by 8 evenly spaced samples in a 3 m by 3 m square collecting aperture. For the simulation results, the number of independent measurement plane frames used to determine $\langle \epsilon^2 \rangle_s$ was 100. . . . . | 75   |

24. Aperture averaged mean squared phase error for theoretical (solid line) and simulated (dash dot) minimum variance results. Aperture averaged mean square phase error for theoretical (solid with asterisk) and simulated (long dashes) results for the new least squares reconstructor. The aperture averaged input phase variance is also shown (dotted line). The true phase map was used to provide phase differences consistent with the SCIP detection process. Gaussian average reflectivity profiles with infinite spatial extent were used in both the theoretical and simulated determination of the aperture averaged mean squared phase error. The horizontal axis is the sampling parameter,  $\beta$ . The measurement plane sampling density was 8 by 8 evenly spaced samples in a 3 m by 3 m square collecting aperture. For the simulation results, the number of independent measurement plane frames used to determine  $\langle \epsilon^2 \rangle_s$  was 100. . . . . 77
25. Comparison of simulated aperture averaged mean squared phase error for minimum variance (solid line) and G & R least squares results (long dashes). The aperture averaged input phase variance is also shown (short dashes). The phase differences were determined from the measurement plane reference phases. The horizontal axis is the sampling parameter,  $\beta$ . The measurement plane sampling density was 8 by 8 evenly spaced samples in a 3 m by 3 m square collecting aperture. The number of independent measurement plane frames used to determine  $\langle \epsilon^2 \rangle_s$  were 100. The theoretical average reflectivity profile of the objects used to estimate  $M_{jn}$  were Gaussian with infinite extent. The simulated average reflectivity profile was matched to the theoretical for both the G & R least squares and minimum variance simulations. . . . . 78



| Figure |  | Page |
|--------|--|------|
| 26.    | Comparison of simulated aperture averaged mean squared phase error for minimum variance (solid line) and G & R least squares results (long dashes). The aperture averaged input phase variance is also shown (short dashes). Phase differences were determined from the measurement plane true phases. The horizontal axis is the sampling parameter, $\beta$ . The measurement plane sampling density was 8 by 8 evenly spaced samples in a 3 m by 3 m square collecting aperture. The number of independent measurement plane frames used to determine $\langle \epsilon^2 \rangle_s$ were 100. The theoretical average reflectivity profile of the object used to estimate $M_{jn}$ was a Gaussian with infinite extent. The simulated average reflectivity profile was matched to the theoretical for both the G & R least squares and minimum variance simulations. | 80   |
| 27.    | (a) True and (b) reconstructed phase for 0.8667 $\mu\text{rad}$ extended object with Gaussian reflectance. . . . .   | 82   |
| 28.    | (a) True and (b) reconstructed phase for 1.300 $\mu\text{rad}$ extended object with Gaussian reflectance. . . . .  | 83   |
| 29.    | (a) True and (b) reconstructed phase for 1.7333 $\mu\text{rad}$ extended object with Gaussian reflectance. . . . .   | 84   |
| 30.    | (a) True and (b) reconstructed phase for 3.467 $\mu\text{rad}$ extended object with Gaussian reflectance. . . . .  | 85   |
| 31.    | (a) Branch cut and (b) unwrapped branch cut for 0.4333 $\mu\text{rad}$ extended object with Gaussian reflectance. . . . .  | 87   |
| 32.    | Minimum variance reconstructed phase for 0.4333 $\mu\text{rad}$ extended object with Gaussian average reflectivity profile. . . . .  | 88   |

33. Minimum aperture averaged mean squared phase error for theoretical (bottom solid line) and simulated (long dashes) minimum variance results. Minimum aperture averaged mean square phase error for theoretical (top solid) and simulated (dash - dot) results for the new least squares reconstructor. The aperture averaged input phase variance is also shown (dotted line). The true phase map was used to provide phase differences. Gaussian average reflectivity profiles with infinite spatial extent were used in the theoretical development of the aperture averaged mean squared phase error. Truncated Gaussian average reflectivity profiles were used for the simulated objects. The horizontal axis is the sampling parameter,  $\beta$ . The measurement plane sampling density was 8 by 8 evenly spaced samples in a 3 m by 3 m square collecting aperture. For the simulation results, the number of independent measurement plane frames used to determine  $\langle \epsilon^2 \rangle_s$  were 100. 91
34. Minimum aperture averaged mean squared phase error for the minimum variance (solid line) and G & R least squares (long dashes) formalisms. Also included is the input aperture averaged mean squared error (short dashes). The horizontal axis is the sampling parameter,  $\beta$ . Gaussian average reflectivity profiles with infinite spatial extent were used in the determination of the optimal reconstruction matrix for minimum variance simulation. Truncated Gaussian average reflectivity profiles were used for the simulated objects in both the minimum variance and G & R least squares methods. . . . . 93
35. Average reflectivity distribution for a random + object with 1.300  $\mu\text{rad}$  angular subtense. . . . . 94
36. Measurement plane phase maps of (a) true phase and (b) reconstructed phase for 1.300  $\mu\text{rad}$  random cross object. The simulated average reflectivity profile was the product of a unit amplitude + object subtending 1.300  $\mu\text{rads}$  and a Gaussian envelope function. The simulated average reflectivity was zero outside the boundaries of the object support. The theoretical object average reflectivity was assumed a Gaussian with infinite spatial extent. The  $e^{-1}$  width of the theoretical object average reflectivity was 1.300  $\mu\text{rads}$ . . . . . 96

| Figure  | Page |
|---|------|
| 37. Measurement plane phase error squared for 1 frame of 1.300 $\mu$ rad random cross. . . . .  | 97   |
| 38. (a) True image and (b) reconstructed image for cross object with 1.300 $\mu$ rad finite extent. The measurement plane sampling density was 8 by 8 evenly spaced samples in a 3 m by 3 m square collecting aperture. The number of independent image frames used to average was 100. .   | 98   |
| 39. Image error squared for an object with a Gaussian average reflectivity profile and spatial structure in the form of a +. The object had a 1.300 $\mu$ rad angular subtense. The quantities, $I_t(x)$ , and, $I_r(x)$ , are the true and reconstructed image irradiance at a point, respectively. . . . .  | 99   |
| 40. Average reflectivity distribution for a random $\times$ object with 1.300 $\mu$ rad angular subtense. . . . .   | 100  |
| 41. (a) true image and (b) reconstructed image for $\times$ object with 1.300 $\mu$ rad finite extent. The measurement plane sampling density was 8 by 8 evenly spaced samples in a 3 m by 3 m square collecting aperture. The number of independent image frames used to average was 100. .  | 102  |
| 42. Image error squared for an object with a Gaussian average reflectivity profile and spatial structure in the form of an $\times$ . The object had a 1.300 $\mu$ rad angular subtense. The quantities, $I_t(x)$ , and, $I_r(x)$ , are the true and reconstructed image irradiance at a point, respectively. . . . .                                 | 103  |
| 43. Average reflectivity distribution for a random cross object with 1.300 $\mu$ rad angular subtense and a constant average reflectivity. The theoretical object average reflectivity was a Gaussian with infinite extent. The simulated object average reflectivity was constant over the support regions of the object and zero elsewhere. . . . . | 104  |
| 44. Measurement plane phase maps of (a) true phase and (b) reconstructed phase for 1.300 $\mu$ rad random cross object. . . . .   | 105  |
| 45. Measurement plane phase error squared for 1 frame of 1.300 $\mu$ rad random cross. . . . .  | 106  |
| 46. (a) True image and (b) reconstructed image for cross object with 1.300 $\mu$ rad finite extent. The measurement plane sampling density was 8 by 8 evenly spaced samples in a 3 m by 3 m square collecting aperture. The number of independent image frames used to average was 100. .   | 107  |

| Figure   | Page |
|--|------|
| 47. Image error squared for 100 frames of 1.300 $\mu\text{rad}$ random cross object. The quantities, $I_t(x)$ , and, $I_r(x)$ , are the image plane irradiances at a point for the true image irradiance and the reconstructed image irradiance, respectively. . . . .   | 108  |
| 48. Aperture averaged mean squared phase error as a function of mismatch between expected object size and actual object size. Optimal reconstruction matrix was determined for an object subtending 1.7333 $\mu\text{rad}$ . Horizontal axis shows percentage of mismatch between the assumed object size and the actual object size. The dotted line shows the aperture averaged input phase variance for a 1.7333 $\mu\text{rad}$ object. The solid line shows $\langle \epsilon^2 \rangle$ as a function of expected to actual object size mismatch. The dashed line shows $\langle \epsilon^2 \rangle$ for a perfect object size estimation. The theoretical average reflectivity profile was a Gaussian with infinite extent and the simulated average reflectivity profile was a truncated Gaussian. . . . . | 110  |
| 49. Theoretical minimum variance aperture averaged mean squared phase error as a function of noise level and sampling parameter, $\beta$ . Additive white Gaussian noise levels were 0 (bottom line), 0.2 (second line from bottom), 1 (third line from bottom), and 2 (top line) radians squared. . . . .   | 111  |
| 50. Theoretical new least squares aperture averaged mean squared phase error as a function of noise level and sampling parameter, $\beta$ . Additive white Gaussian noise levels were 0 (bottom line), 0.2 (second line from bottom), 1 (third line from bottom), and 2 (top line) radians squared. . . . .  | 112  |

51. Simulated aperture averaged mean squared phase error for minimum variance and G & R least squares methods as a function of noise level and sampling parameter,  $\beta$ . Additive white Gaussian noise levels were 0.2 radians squared. The bottom solid line indicates the simulated aperture averaged squared phase error for the minimum variance reconstructor and no noise. The dashed line second from the bottom represents the minimum variance simulated aperture averaged mean squared phase error with  $\sigma_n^2 = 0.2$  radians squared. The third line from the bottom is the simulated G & R least squares results and no noise. The fourth line from the bottom shows the simulated performance of a G & R least squares reconstructor with the same noise variance as the minimum variance reconstructor. The top line shows the aperture averaged input phase variance for no noise. . . . . 114
52. Simulated aperture averaged mean squared phase error for minimum variance and G & R least squares methods as a function of noise level and sampling parameter,  $\beta$ . Additive white Gaussian noise levels were 1.0 radians squared. The bottom solid line indicates the simulated squared error for the minimum variance reconstructor and no noise. The dashed line second from the bottom represents the minimum variance simulated aperture averaged mean squared phase error with  $\sigma_n^2 = 0.2$  radians squared. The third line from the bottom is the simulated G & R least squares results and no noise. The fourth line from the bottom shows the simulated performance of a G & R least squares reconstructor with the same noise variance as the minimum variance reconstructor. The top line shows the aperture averaged input phase variance for no noise. . . . . 115

53. Simulated aperture averaged mean squared phase error for minimum variance and G & R least squares methods as a function of noise level and sampling parameter,  $\beta$ . Additive white Gaussian noise levels were 2.0 radians squared. The bottom solid line indicates the simulated squared error for the minimum variance reconstructor and no noise. The dashed line second from the bottom represents the minimum variance simulated aperture averaged mean squared phase error with  $\sigma_n^2 = 0.2$  radians squared. The third line from the bottom is the simulated G & R least squares results and no noise. The fourth line from the bottom shows the simulated performance of a G & R least squares reconstructor with the same noise variance as the minimum variance reconstructor. The top line shows the aperture averaged input phase variance for no noise. . . . . 116

*Abstract*

In sheared coherent beam interferometric imaging, an estimate of the average reflectivity profile of the object can be computed from measurements of point-to-point phase differences in the far field interference pattern and a suitable phase reconstruction technique. The phase difference information is encoded in the irradiance of three identical, shifted and superimposed speckled laser beam patterns. A minimum variance phase reconstruction technique is presented to estimate the phase of the field in the measurement plane from the phase differences and evaluate its performance. Prior knowledge of the phase covariance is used in the minimum variance reconstructor. Analytic calculations and computer simulations are used to evaluate phase reconstruction errors as a function of object coherence area and spatial sample spacing in the measurement plane. The performance of the minimum variance reconstructor is compared to two least squares reconstructor implementations. Theoretical performance comparisons are made between the minimum variance reconstructor and a new implementation of the least squares formalism. The new least squares reconstructor uses the same error metric as the minimum variance reconstructor but does not use any statistical information in estimating the measurement plane phase function. Comparisons of the minimum variance reconstructor with a conventional implementation of the least squares formalism are also made. The performance of the minimum variance reconstructor is demonstrated for objects which are optically smooth as well as optically rough. A small random double point source object is used to demonstrate the near diffraction limited resolution of the minimum variance wavefront reconstructor. Phase and image reconstructions are demonstrated for extended objects. Computer simulation is used to illustrate the performance of the minimum variance reconstructor in the presence of additive white Gaussian noise and estimation errors.

# OPTIMAL WAVEFRONT RECONSTRUCTION FOR A COHERENT DIFFRACTED FIELD

## *I. Introduction*

### *1.1 Problem Statement*

The problem addressed in this dissertation is how to do optimal wavefront reconstruction in a synthetic aperture coherent imaging system. The problem is addressed by developing a new minimum variance wavefront reconstructor which uses object support information and the measurement plane phase covariance to estimate a two-dimensional phase map in the Fraunhofer plane of the object. Computer simulations are used to compare the actual performance of the minimum variance reconstructor to its theoretical performance, and to compare the actual performance of the minimum variance reconstructor to the conventional least squares reconstructor.

### *1.2 Overview*

Atmospheric turbulence effects limit the resolution which can be obtained in images of space objects [1]. If incoherent imaging is performed without use of adaptive optics or a post detection image reconstruction technique the angular resolution which can be obtained is given approximately by  $\frac{\bar{\lambda}}{r_0}$ , where  $r_0$  is the Fried seeing parameter, and  $\bar{\lambda}$  is the average wavelength of the light. The angular resolution obtained by diffraction-limited imaging is approximately  $\frac{\bar{\lambda}}{D}$ , where  $D$  is the telescope diameter. For space object imaging,  $r_0$  is typically much smaller than  $D$ , with  $10 \leq \frac{D}{r_0} \leq 50$  being typical. Pre-detection correction techniques, such as adaptive optics [2, 3], and post-detection image processing techniques [4] can substantially improve resolution beyond the  $\frac{\bar{\lambda}}{r_0}$  limit imposed by atmospheric turbulence. How-



ever, the ultimate limit of resolution for a filled aperture telescope imaging system is imposed by the diameter of the telescope.

Active imaging techniques, which use laser illumination, can be used to form synthetic apertures that have much greater effective size than the diameter of filled aperture telescopes which can currently be fabricated [5]. Such systems can be used to form images of space objects within the useful range of the illuminating laser for applications such as monitoring the location and orientation of Earth-orbiting satellites and space debris. The paradigm of operation for an active imaging system is as follows. A laser, or a set of phase coupled lasers, are used to illuminate the object. Radiation scattered from the object is measured in a distant plane. These measurements are then processed to reconstruct an image of the object. Most sensor systems and processing algorithms exploit the fact that the far field of the scattering object is proportional to the Fourier transform of the reflectance of the object. However, the irradiance distribution of the scattered laser field suffers from coherent speckle effects.

One synthetic aperture method, referred to as Sheared Coherent Interferometric Photography (SCIP), uses a three beam shearing interferometer system to encode information about phase differences between spatial points on the scattered wavefront as temporal variations of the irradiance in the far field [5]. Notice that (a) the measurement points are very sparse within the aperture, and (b) the synthetic aperture size is the area enclosed by the sparse set of measurement points. Information about the modulus of the Fourier transform of the object is provided directly by the irradiance measurements. The phase differences must be processed to recover the phase of the Fourier transform of the object field. The phase reconstruction process is complicated by the fact that, while the complex field in the measurement plane must be continuous, the phase of the field in the measurement plane can be discontinuous because of real zeros in the irradiance and because of the possibility of  $2\pi$  phase ambiguities which are difficult to resolve.

The reconstructor presented here provides continuous phase reconstructions. However, the phase of the field in the aperture plane can have  $2\pi$  phase discontinuities which arise when the phasor representing the complex field in the aperture crosses between the second and third quadrants of the complex plane. To overcome this problem and provide a continuous phase for comparison, a computationally efficient algorithm for unwrapping the  $2\pi$  phase discontinuities [6] is used and the resulting unwrapped phase is compared to the phase map obtained from the minimum variance reconstructor. The phase in the aperture plane can also be affected by the presence of real zeros in the field which arise from coherent speckle effects. Such points are referred to as branch cuts. The phase of the field along a branch cut is discontinuous and the phase difference across a branch cut is  $\pm 2\pi$ . The reconstructor presented here provides continuous phase estimates across the  $2\pi$  discontinuities associated with branch cuts.

Some previous phase reconstructors have been iterative in nature, based on the fact that the phase around any closed loop in the measurement plane must sum to zero in the absence of noise and real zeros in the field [7, 8]. Hence, these phase reconstruction techniques have treated the phase reconstruction process as a deterministic problem. However, the phase reconstruction process is essentially a stochastic problem, with randomness arising from uncertainty about the micro-state of the reflective surface of the object. The phase reconstruction problem can thus be addressed using statistical methods. In this dissertation, a minimum variance phase reconstructor based on the correlation properties of the phase of a scattered laser field is described. The reconstructor explicitly minimizes the aperture averaged mean squared phase error. The complex field in the far field diffraction region of the object has been shown to obey circularly complex Gaussian statistics [9]. The probability density function of the phase of the far field and the spatial correlation function of the phase in the far field of the object have been previously calculated [10, 11]. This phase correlation function is used in the development of a minimum variance

technique [12] to estimate the phase in the measurement plane of a coherent imaging system. The reconstructed phase is combined with modulus information to form an estimate of the complex field. An image is obtained by Fourier transforming the measurement plane field, and averaging is used in image space to reduce measurement noise, reduce speckle effects, and improve image quality.

The minimum variance reconstructor is implemented, and its performance is assessed by theoretical calculations and computer simulation. For the input phase differences provided by the SCIP detection process, the measurement is found to be insensitive to  $2\pi$  phase discontinuities. Continuous phase estimates are provided in the region of branch cuts, which arise from real zeros in the measurement plane field. An off-axis point source object is used to demonstrate that the minimum variance reconstructor works for a simple, deterministic test case. The off-axis point source object gives rise to a tilted plane in the measurement plane phase map. Reconstructing the tilted phase plane demonstrates that the scaling and implementation (throughput) aspects of the minimum variance reconstructor are correct and that the minimum variance reconstructor can reconstruct the off-axis point source object. The key statistical expressions in the minimum variance reconstructor are the measurement plane phase covariances. The phase covariances are checked by implementing the key matrices in the reconstructor in validation software and comparing the resulting matrix elements.

After demonstrating that the minimum variance reconstructor works for a simple deterministic object and correctly determines the measurement plane phase covariances, the performance of the reconstructor is assessed for differing cases. The first case describes the performance of the minimum variance reconstructor under ideal conditions (no measurement noise, no randomness in the object phase, and no estimation errors in object size). These conditions apply to an object which is smooth on the scale of an optical wavelength (optically smooth) with no measurement noise. The object average reflectivity profile used in the theoretical determination of the

optimal reconstructor was assumed to be Gaussian with infinite extent. In simulating the optically smooth object, the Gaussian average reflectivity profile was set to zero outside the boundaries of the object support to create a truncated Gaussian average reflectivity distribution. The truncated Gaussian average reflectivity profile used in the simulation models the discontinuous average reflectivity profile along the boundaries of the object.

The performance of the minimum variance reconstructor is assessed for the case of optically smooth objects. The optically smooth object can be considered a special case of the random scattering problem where the randomization of the amplitude and phase are negligible. The results for optically smooth objects are expected to be better than the results for optically rough objects for equivalent imaging conditions. The performance of the minimum variance reconstructor is demonstrated for two types of optically smooth objects. The first object has an average reflectivity profile which is the product of a unit amplitude annular ring and a 2D Gaussian function. The second object consists of the product of three equally spaced unit amplitude horizontal bars and a Gaussian function.

After evaluating the performance of the minimum variance reconstructor for the non-random case, a geometrically simple extended object is evaluated which is rough on the scale of an optical wavelength. The object average reflectivity is represented by two random radiating point sources. The random double point source object is used to determine the resolution of the optical system. The individual point sources are symmetrically placed about the optical axis of the imaging system. Reconstructed images resulting from averaging 100 independent image plane irradiance realizations are used to demonstrate that nearly diffraction limited images are reconstructed by the minimum variance reconstructor. Besides demonstrating the resolution of the optical system, the reconstructed image of the random double point source object shows the ability of the minimum variance reconstructor to image simple optically rough objects.

After presenting the results for the simple random scatterer, the performance of the minimum variance reconstructor is assessed for optically rough extended objects with optimal viewing conditions consisting of no measurement noise, and no errors in estimating the object size or object average reflectivity profiles. An image for a small extended object is reconstructed and compared to the averaged coherent image obtained from a filled  $3 \text{ m} \times 3 \text{ m}$  square collecting aperture. The theoretical and simulated object average reflectivity profiles were both modeled as 2D Gaussian functions with infinite spatial extent. The simulated reconstructed image is determined by averaging 100 independent image frames generated by using the minimum variance formalism and noise free phase difference measurements. The average coherent image is obtained by averaging 100 independent images where each image frame is formed by Fourier transforming the true aperture plane field.

The spatial sampling required to obtain good phase reconstructions is related to the size and shape of the object. Spatial sampling effects were investigated as a function of the sampling parameter,  $\beta = \frac{L}{\sqrt{A_c}}$ , where  $L$  is the separation of the sampling points in the measurement plane, and  $A_c$  is the coherence area of the object. It should be noted that the sampling parameter,  $\beta$ , does not factor out of the analysis of the minimum variance wavefront reconstructor, but rather derives from the physical intuition that the coherence area and the required sampling are closely related. Measurement plane two-dimensional phase maps are reconstructed for several values of the sampling parameter,  $\beta$ , and compared to the expected measurement plane phase through simulation. Good measurement plane phase reconstructions are demonstrated for  $\beta$  in the range  $0 < \beta \leq 0.47$ . The aperture averaged mean squared phase error is determined, and theoretical comparisons between the minimum variance and a new least squares reconstructor shows better performance for the minimum variance reconstructor. Simulated aperture averaged mean squared phase errors are determined as a function of  $\beta$  for the minimum variance and least squares methods. The simulated aperture averaged mean squared phase error is determined

for the minimum variance wavefront reconstructor and is compared to the simulated aperture averaged mean squared phase error for both the new least squares wavefront reconstructor and a conventional least squares wavefront reconstructor. Besides understanding the performance of the minimum variance wavefront reconstructor for perfect viewing conditions, the effects of noise and errors in the estimation process (such as errors in estimating the object size and average reflectivity) are of interest.

The performance of the minimum variance reconstructor is presented for extended targets and under conditions where imperfect model information is available. Mismatches between the theoretical and simulated object average reflectivity profiles are characterized. The theoretical object average reflectivity is assumed a Gaussian with infinite spatial extent and the simulated object average reflectivity profile is assumed to be a truncated Gaussian. The aperture averaged mean squared phase error is determined for both the minimum variance and least squares methods for this average reflectivity mismatched case. Both the new least squares wavefront reconstructor and a conventional least squares reconstructor are used in the evaluation of the aperture averaged mean squared phase error.

Spatial features are included in the simulated average reflectivity profiles of the extended objects. The extended objects have average reflectivity profiles in the shape of an  $\times$  and a  $+$ . Mismatches between the theoretical and simulated object average reflectivity shape are shown to have a negligible effect. Mismatches between the theoretical and simulated object sizes were characterized in terms of the aperture averaged mean squared phase error. The performance of the minimum variance wavefront reconstructor is demonstrated in the presence of white Gaussian noise.

### *1.3 Summary of Significant Contributions and Results*

This section describes the most important results obtained during the course of this research. An enumerated list of the contributions and key results is as follows:

1. The minimum variance wavefront reconstructor is the first coherent wavefront reconstructor which uses statistical information (in the form of measurement plane phase covariances) to estimate the wavefront in the measurement plane of a coherent imaging system. The impact of measurement noise and imprecise knowledge of the object average reflectivity profile was evaluated.
2. The minimum variance reconstructor, unlike previously published least squares reconstructors, allows for interpolation between sparsely sampled reconstructed measurement plane phase estimates.
3. The performance of the minimum variance reconstructor in terms of the theoretical and simulated aperture averaged mean squared phase error is shown to be superior to the performance of both a previously published conventional least squares reconstructor and an alternative least squares reconstructor implemented here.
4. A new least squares reconstructor was developed which provides for interpolation between reconstructed measurement plane phase estimates.
5. Measurement plane phase reconstructions are demonstrated for values of  $\beta$  in the range of  $0 \leq \beta \leq 0.47$ . The theoretical and simulated object average reflectivities used in reconstructing the measurement plane phases were both Gaussian with infinite spatial extent.
6. The minimum variance technique provides near diffraction limited images for a sparsely sampled measurement plane aperture (8 by 8 evenly spaced samples in a 3 m square aperture).

#### *1.4 Overview of Dissertation*

The remainder of the dissertation is organized as follows. Chapter II provides background information. The SCIP technique summary in section 2.1 describes how the atmospheric noise free phase differences are obtained. The use of the SCIP phase

differences in a conventional least squares wavefront reconstructor is presented in section 2.2. The least squares reconstructor provides a two-dimensional phase map in the measurement plane of the optical system. The phase map and amplitude information are used to estimate the measurement plane field. Section 2.3 discusses how the measurement plane field is used in the the image formation process.

Chapter III presents the theoretical framework for the minimum variance wavefront reconstructor. Section 3.1 develops the error metric used in the performance estimation process. To evaluate the error metric, expressions for the measurement plane phase covariance and a reconstruction matrix are required. Section 3.2 discusses the determination of the measurement plane phase covariances. Section 3.3 describes the derivation of the minimum variance reconstructor. Section 3.4 describes the derivation of a new least squares reconstructor which has the same error metric as the minimum variance wavefront reconstructor. Theoretical expressions for the aperture averaged mean squared phase error for the minimum variance and least squares formalisms are derived in Section 3.1.

Chapter IV presents the results. Section 4.1 shows the performance of the minimum variance wavefront reconstructor for the case of noise free optically smooth objects. The optically smooth object case is expected to have better performance than the random object case for similar imaging conditions. Section 4.2 uses the random double point source object to demonstrate that the reconstructor works for simple extended objects that are rough on the scale of an optical wavelength. Section 4.2 is also used to demonstrate that the minimum variance wavefront reconstructor can be used to create images with diffraction limited information. Section 4.3 treats optically rough extended objects under optimal viewing conditions (no noise and no estimation errors). Section 4.4 evaluates the performance of the minimum variance reconstructor for optically rough extended objects under conditions where imperfect model information is available. Mismatches between the model and actual object average reflectivity are related to the performance of the minimum variance wavefront



reconstructor. The aperture averaged mean squared phase error is shown to be larger for the case when the model and the object are imperfectly matched. Mismatches between the theoretical and simulated size of the object average reflectivity profile are shown to have minor effects on the reconstructed images under a wide range of conditions. Finally, the performance of the minimum variance reconstructor in the presence of additive, Gaussian, white noise is addressed.

Chapter V presents the conclusions, summarizes the significant contributions, and addresses future areas of research.

## II. Background

This section provides the specialized background information required for the rest of the dissertation. Section 2.1 discusses the SCIP imaging technique which provides phase differences on a measurement plane grid of points for every pupil frame. The SCIP generated phase differences are used as inputs into a wavefront reconstructor. Conventional coherent least squares wavefront reconstructors are discussed in Section 2.2. Section 2.3 discusses the image formation process and shows that for coherent imaging, the time averaged image is identical to that obtained with the incoherent optical transfer function.

### 2.1 Sheared Coherent Interferometric Photography

When a scattering surface which is rough on the scale of an optical wavelength is illuminated by a laser, a random complex-valued electromagnetic field appears in the far field with point statistics described by circularly complex Gaussian statistics [9]. In the far field region of the object a speckled irradiance distribution is observed [13]. The SCIP technique is a method for measuring phase differences on a grid of points in an aperture. The SCIP technique is a synthetic aperture technique in the sense that no filled aperture is required. Rather, the aperture is defined by the area enclosed by a set of irradiance measurement devices. Phase difference information is encoded in temporal variations in the irradiance measurements. The measured phase differences provide the input to the wavefront reconstructor.

The measurement geometry is shown in Figure 1. Three illuminating laser beams are spatially separated from one another as illustrated in Figure 1. The three beams are used to simultaneously illuminate an object located in the far field of the illumination plane. The separation of the illuminating beams are in orthogonal directions, and are denoted by the vector separations  $\vec{s}_x$  and  $\vec{s}_y$ . In addition to the spatial separation, two of the beams are frequency shifted with respect to the

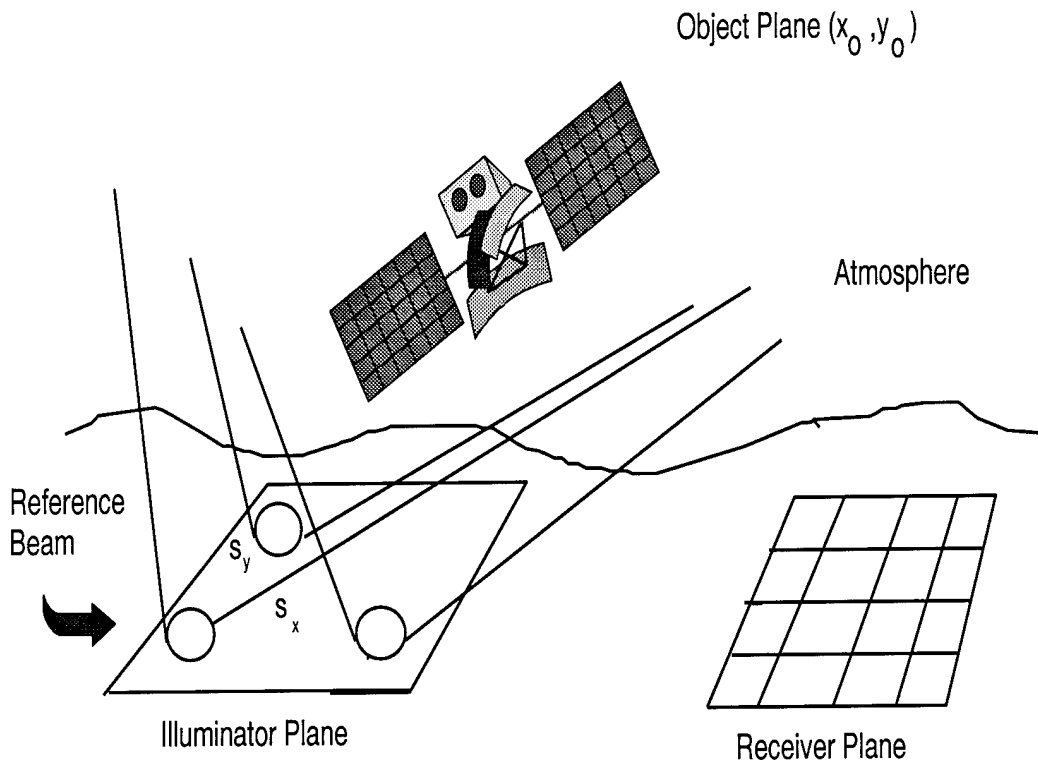


Figure 1. Illumination geometry.

third beam. The relative shifts in frequency of the two beams,  $\nu_x$  and  $\nu_y$ , results in separate temporal modulations relative to the third beam. The shifts are relative to a reference frequency,  $\nu_0 = \frac{c}{\bar{\lambda}}$ , where  $c$  is the speed of light and  $\bar{\lambda}$  is the center wavelength of the reference beam. As shown below, the frequency shifts allow for the encoding of phase difference information in the propagating electromagnetic waves.

The SCIP technique is of interest for imaging earth-orbiting objects because it is insensitive to atmospheric turbulence effects. As the three beams propagate through the atmosphere toward the object their phases become distorted. Since the majority of phase aberrations in the illumination process occur in the near field of the illuminating beams, diffraction of the propagating beams ensures that the three beams are mutually spatially coherent by the time they reach the object. Since the illuminating apertures are typically less than 0.3 meters in diameter, the spatial irradiance profile of each of the illuminating beams in the far field object

plane is approximately flat. Hence, atmospheric effects due to propagation from the illuminating aperture to the object are negligible. The mutually coherent beams are overlapped on the object, and strike the object at slightly different angles due to the separation of the illuminating beams. The three superimposed beams interact with the object, which is assumed to be rough on the scale of an optical wavelength. In the far field of the scattering object, each beam causes a speckled irradiance distribution. A change in the angle of incidence of an illuminating beam results in the reflected speckle pattern shifting in an equal and opposite amount. The reflected fields experience the same object reflectance but leave at slightly different angles. The beams are scattered by the object and give rise to three overlapping speckle patterns in the receiver plane. A key feature of the SCIP technique is that the reflected fields propagate through essentially the same atmosphere while en-route to the receiver plane. As shown later, this results in the phase differences between the propagating beams being insensitive to atmospheric distortions.

The field in the receiver plane consists of the superposition of three identical fields which are shifted (or sheared) with respect to one another [5]. The measurement plane irradiance at a given instant is given by,

$$I(\vec{x}; t) = |u_0(\vec{x}; t) + u_x(\vec{x} + \vec{s}_x; t) + u_y(\vec{x} + \vec{s}_y; t)|^2, \quad (1)$$

where  $\vec{x}$  is a two-dimensional position vector in the measurement plane. The quantities  $\vec{s}_x$  and  $\vec{s}_y$  represent the measurement plane vector separations between the three fields. The individual field quantities are given by,

$$\begin{aligned} u_0(\vec{x}; t) &= A(\vec{x}) \exp j\phi(\vec{x}) \exp j2\pi\nu_0 t, \\ u_x(\vec{x} + \vec{s}_x; t) &= A(\vec{x} + \vec{s}_x) \exp j\phi(\vec{x} + \vec{s}_x) \exp j2\pi(\nu_0 + \nu_x) t, \\ u_y(\vec{x} + \vec{s}_y; t) &= A(\vec{x} + \vec{s}_y) \exp j\phi(\vec{x} + \vec{s}_y) \exp j2\pi(\nu_0 + \nu_y) t. \end{aligned} \quad (2)$$

The complex field,  $u_0$ , is the reference field. The complex fields  $u_x$  and  $u_y$  represent the sheared field in the  $x$  direction and the sheared field in the  $y$  direction, respectively. The frequencies  $\nu_x$  and  $\nu_y$  are the frequency shifts in the  $x$  and  $y$  sheared beams, respectively. The quantities  $A(\cdot)$  and  $\phi(\cdot)$  represent the position dependent amplitude and phase of the corresponding reference,  $x$  sheared and  $y$  sheared fields. The temporal dependence of the  $A(\cdot)$  and  $\phi(\cdot)$  terms is neglected because these quantities are object dependent, and it is assumed that the measurement interval is short compared to the time scale of the object variations. Expanding the square in equation (1) and regrouping terms allows the measurement plane irradiance to be expressed as [14],

$$\begin{aligned} I(\vec{x}, t) = & I_m(\vec{x}) \{1 + V_x(\vec{x}) \cos[2\pi\nu_x t + \Delta\phi_x(\vec{x})] \\ & + V_y(\vec{x}) \cos[2\pi\nu_y t + \Delta\phi_y(\vec{x})] + V_{xy}(\vec{x}) \cos[2\pi(\nu_x - \nu_y)t + \Delta\phi_{xy}(\vec{x})]\}, \end{aligned} \quad (3)$$

where the mean irradiance at  $I_m(\vec{x})$  is given by,

$$I_m(\vec{x}) = \left\{ |u_0(\vec{x})|^2 + |u_x(\vec{x} + \vec{s}_x)|^2 + |u_y(\vec{x} + \vec{s}_y)|^2 \right\}. \quad (4)$$

The quantity,  $I_m(\vec{x})$ , is the time averaged irradiance in the measurement plane due to all three fields. The visibility factors associated with the three temporal frequency components in equation (3),  $\nu_x$ ,  $\nu_y$ , and  $\nu_x - \nu_y$  are given by,

$$\begin{aligned} V_x(\vec{x}) &= 2I_m(\vec{x})^{-1} |u_0(\vec{x}) u_x^*(\vec{x} + \vec{s}_x)|, \\ V_y(\vec{x}) &= 2I_m(\vec{x})^{-1} |u_0(\vec{x}) u_y^*(\vec{x} + \vec{s}_y)|, \\ V_{xy}(\vec{x}) &= 2I_m(\vec{x})^{-1} |u_x(\vec{x} + \vec{s}_x) u_y^*(\vec{x} + \vec{s}_y)|. \end{aligned} \quad (5)$$

where the asterisk represents complex conjugation. The phase differences in equation (3) are given by,

$$\begin{aligned}\Delta\phi_x(\vec{x}) &= \phi(\vec{x}) - \phi(\vec{x} + \vec{s}_x), \\ \Delta\phi_y(\vec{x}) &= \phi(\vec{x}) - \phi(\vec{x} + \vec{s}_y), \\ \Delta\phi_{xy}(\vec{x}) &= \phi(\vec{x} + \vec{s}_x) - \phi(\vec{x} + \vec{s}_y).\end{aligned}\tag{6}$$

In the subsequent analysis only the first two phase differences are required.

We can now demonstrate the insensitivity of the SCIP technique to turbulence effects along the path from the object to the aperture plane. To illustrate this point, consider the effects of turbulence on two of the wavefronts,  $u_0(\vec{x}, t)$  and  $u_x(\vec{x} + \vec{s}_x, t)$ . After reflection, the two beams propagate through the same atmosphere and acquire the phase aberration,  $\psi(\vec{x})$ . The effect of this phase aberration on the measurement plane irradiance is encoded in the term,

$$u_o(\vec{x}, t) u_x^*(\vec{x} + \vec{s}_x, t) = A(\vec{x}) A^*(\vec{x} + \vec{s}_x) \exp(\Delta\phi_x(\vec{x}) - 2\pi\nu_x t + \psi(\vec{x}) - \psi(\vec{x})).\tag{7}$$

Since at the point,  $\vec{x}$ , the fields  $u_0(\vec{x}, t)$  and  $u_x(\vec{x} + \vec{s}_x, t)$  experience the same atmospheric phase distortion the resulting phase difference illustrated in equation (7) is insensitive to atmospheric phase perturbations.

By taking the temporal Fourier transform of the measurement plane irradiance in equation (3) at each sampling point in the measurement plane the following relationship is obtained,

$$\begin{aligned}I(\vec{x}, \nu) &= I_m(\vec{x}) \left\{ \delta(\nu) + \frac{V_x(\vec{x})}{2} \delta(\nu - \nu_x) \exp\{j\Delta\phi_x(\vec{x})\} \right. \\ &\quad + \frac{V_x(\vec{x})}{2} \delta(\nu + \nu_x) \exp\{-j\Delta\phi_x(\vec{x})\} \\ &\quad \left. + \frac{V_y(\vec{x})}{2} \delta(\nu - \nu_y) \exp\{j\Delta\phi_y(\vec{x})\} \right\}\end{aligned}$$

$$\begin{aligned}
& + \frac{V_y(\vec{x})}{2} \delta(\nu + \nu_y) \exp \{-j\Delta\phi_y(\vec{x})\} \\
& + \frac{V_{xy}(\vec{x})}{2} \delta(\nu - (\nu_x - \nu_y)) \exp \{j\Delta\phi_{xy}(\vec{x})\} \\
& + \frac{V_{xy}(\vec{x})}{2} \delta(\nu + (\nu_x - \nu_y)) \exp \{-j\Delta\phi_{xy}(\vec{x})\} \}.
\end{aligned} \tag{8}$$

A narrow band filter centered at either  $\nu_x$  or  $\nu_y$  provides the appropriate phase difference measurement. For example, to obtain the phase difference in the  $x$  direction, a narrow band filter centered at frequency,  $\nu_x$ , leads to the following relationship between the irradiance spectrum,  $I(\vec{x}, \nu_x)$ , and the phase difference  $\Delta\phi_x(\vec{x})$ ,

$$I(\vec{x}, \nu_x) = \frac{1}{2} I_m(\vec{x}) V_x(\vec{x}) \exp \{j\Delta\phi_x(\vec{x})\}. \tag{9}$$

The above expression provides the relationship between irradiance measurements at discrete points in the measurement plane and the desired phase differences at that point. The phase difference in the  $x$  direction can be evaluated by the following relationship, A

$$\Delta\phi_x(\vec{x}) = \tan^{-1} \left( \frac{\Im(I(\vec{x}, \nu_x))}{\Re(I(\vec{x}, \nu_x))} \right). \tag{10}$$

The operator,  $\Im(\cdot)$ , represents taking the imaginary part of the argument. The operator,  $\Re(\cdot)$ , represents taking the real part of the argument. Another filter centered at  $\nu_y$  can be used to obtain the phase difference in the  $y$  direction. Equation (8) is then evaluated at  $\nu_y$  and similar expressions to equations (9) and (10) result for phase differences in the  $y$  direction. The SCIP technique provides phase differences, which are known modulo  $2\pi$ , on a grid of points in the measurement plane [5, 14]. The phase differences obtained in this manner are mapped into the range of  $-\pi \leq \Delta\phi_q(\vec{x}) \leq \pi$ . The insensitivity to  $2\pi$  phase discontinuities can be seen from equations (9) and (10). The complex exponential is insensitive to any arbitrary addition or subtraction of  $2\pi$  to its argument. The phase reconstruction technique discussed here uses the phase difference measurements obtained by the SCIP method combined with a minimum variance technique to estimate the measurement plane

phase. In the next section, the conventional least squares method of phase estimation is discussed and related to the SCIP phase difference measurements.

## 2.2 *Conventional Least Squares Reconstructors*

The phase differences provided by SCIP are input to a wavefront reconstructor in order to reconstruct the measurement plane phase. This section discusses the least squares formalism to the phase reconstruction problem. The least squares reconstructor discussed uses deterministic methods to estimate the two-dimensional (2D) phase map in the measurement plane of the imaging system, neglecting the statistical aspects of the phase reconstruction process. The conventional least squares reconstructor directly minimizes a squared error metric (such as the squared phase error or squared phase difference error) without using statistics. Since no statistics are used in the least squares method, the solutions are deterministic.

The reconstruction of two-dimensional phase surfaces from phase difference measurements has been of interest to researchers in adaptive optics and speckle imaging for a number of years. The reconstruction process involves transforming noisy phase differences into a 2D phase surface in the measurement plane of the imaging system. Previous work [15, 16] was directed at reconstructing the phase map on a 2D grid of points using a least squares formalism. Figure 2 illustrates the points of reconstruction in the measurement plane.

In Figure 2, the quantities  $N_x$  and  $N_y$  correspond to the number of sample points in the  $x$  and  $y$  direction, and  $L_x$  and  $L_y$  represent the distance in meters between the sample points in the  $x$  and  $y$  directions, respectively. The coordinates  $j$  and  $k$  are indices which denote the sampled phase locations in the measurement plane in the  $x$  and  $y$  directions, respectively. An often used least squares solution [6, 8, 16, 17] minimizes the squared phase error summed over a discrete set of points



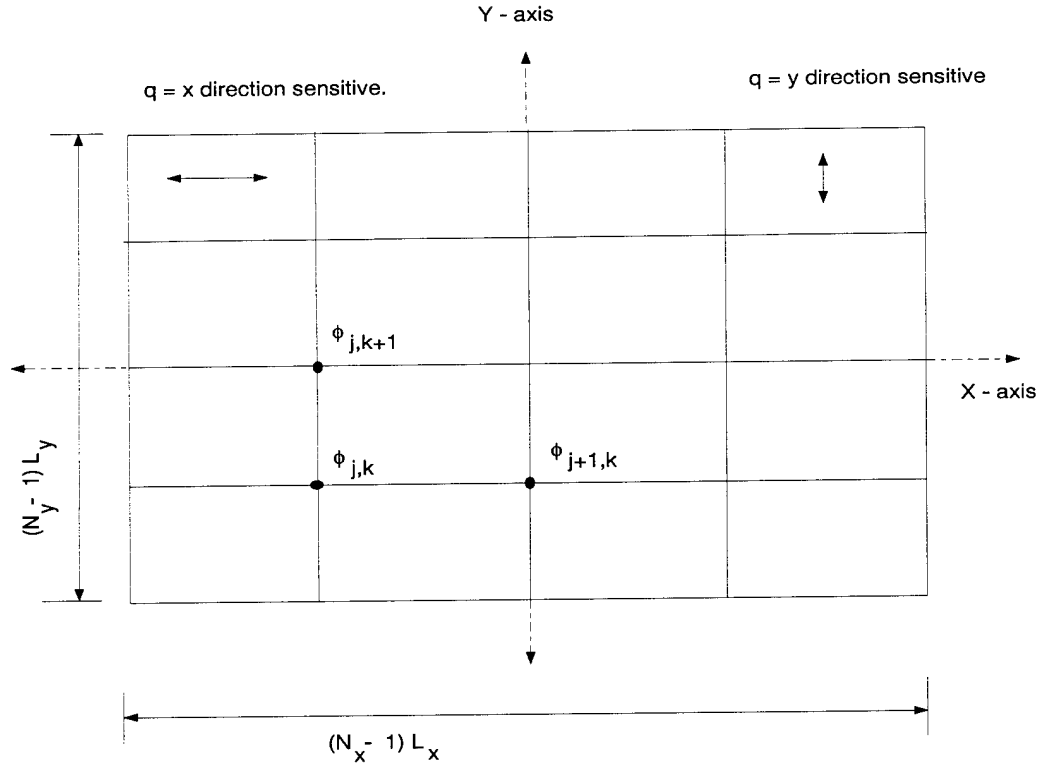


Figure 2. Measurement plane grid.

in the measurement plane aperture,

$$\varepsilon^2 = \sum_j \sum_k (\phi(\vec{x}_{j,k}) - \phi'(\vec{x}_{j,k}))^2, \quad (11)$$

where the symbol,  $\phi'(\vec{x}_{j,k})$ , represents the phase estimate at grid coordinate,  $\vec{x}_{j,k}$ .

The least squares solution is specified in terms of the following recursive equation,

$$\begin{aligned} \phi'(\vec{x}_{j,k}) &= \frac{1}{4} (\phi(\vec{x}_{j+1,k}) + \phi(\vec{x}_{j-1,k}) + \phi(\vec{x}_{j,k+1}) + \phi(\vec{x}_{j,k-1})) \\ &+ \frac{1}{4} (\Delta\phi_x(\vec{x}_{j,k}) - \Delta\phi_x(\vec{x}_{j-1,k}) + \Delta\phi_y(\vec{x}_{j,k}) - \Delta\phi_y(\vec{x}_{j,k-1})), \end{aligned} \quad (12)$$

where the phase differences in equation (12) are given in equation (6). Note that equation (12) only provides phase differences on a grid of points in the measurement plane and not everywhere in the aperture. Other least squares implementations exist

which minimize the sum of squares of the difference between the actual and estimated phase differences [18]. Equation (12) can be iteratively solved to estimate the phase on a finite grid of points in the measurement plane [16]. Other solutions similar to equation (12) can be formulated by summing over different closed paths on the grid. A common feature of the recursive least squares phase reconstructors is that they are based on a path integral approach where the sum of the phase differences around any closed path sums to zero. A matrix formulation of solving the least squares phase estimation problem has been developed [17]. Properly constrained, this matrix algebra method was shown to give results similar to the recursive approaches illustrated in equation (12).

Additional complications result in reconstructing the measurement plane 2D phase map when the object is illuminated by coherent light. The irradiance distribution in the Fraunhofer plane of the object can have isolated zeros. In the case of an isolated zero, neighboring phases can assume discontinuous values resulting in  $2\pi$  ridges in the 2D measurement plane phase map [19]. The ridges in the measurement plane 2D phase are referred to as branch cuts. Summed phase differences around a closed path containing an isolated zero do not sum to zero. The conventional least squares iterative solution given in equation (12) requires modification to account for the presence of isolated zeros and the associated branch cuts.

To adapt the conventional least squares formalism to the case of coherent illumination, the sum of the phase differences along any enclosed path on the measurement grid was allowed to vary [8]. This was done to permit the summation around an isolated zero in the measurement plane field. To account for the presence of isolated zeros in the measurement plane field, the sum of the phase differences around any closed path in the measurement plane were allowed to vary in integer multiples of  $\pm 2\pi$ .

In the SCIP detection process, the phase difference between neighboring grid points was wrapped into the principal value of  $\pm\pi$ . The actual sign and magnitude of

the phase difference is given by equation (10). The wrapping of the phase differences into their principal values was done to reflect the inability of the measurement system to distinguish the integer value associated with the  $\pm 2\pi$  increments added to the phase at any given grid coordinate.

A different ridge-like type of phase discontinuity which appears similar to branch cuts arises in the measurement plane phase function. These ridges result from the complex exponential representation of the measurement plane field. Specifically, the phase is represented as the argument of a complex exponential. Phases whose magnitude exceed the value of  $\pi$  (such as is possible, for example, for tilted phase planes arising from off-axis objects which resemble point sources) are automatically wrapped into the principal region  $\pm\pi$  by subtracting integer multiples of  $2\pi$ . Phase differences across the phase ridge have a constant magnitude of  $2\pi$ . To distinguish between the  $2\pi$  discontinuities associated with branch cuts, these phase ridges will be denoted as  $2\pi$  phase wraps.

The presence of branch cuts and  $2\pi$  phase wraps lead to discontinuities in the measurement plane phase, and limitations in data collection systems result in the measured phase differences being restricted to their principal range of  $(-\pi, \pi)$ . By using a 2D phase unwrapping technique [6], integer multiples of  $2\pi$  are added to the phase in the reconstruction process to account for these discontinuities. Figure 3, illustrates a branch cut from an object with an angular subtense of  $0.4333 \mu\text{rad}$ . The simulation will be discussed later. The branch cut originates in the lower right quadrant of Figure 3. The branch cut runs from the bottom to the top of the right half of the figure. The magnitude of the phase difference across the branch cut is  $2\pi$ .

Ghiglia and Romero (G & R) have recently implemented the coherent version of the least squares phase reconstructor in a fast, non-iterative manner using Discrete Cosine Transforms [6]. This reconstructor was used in the simulation process for the following two purposes:

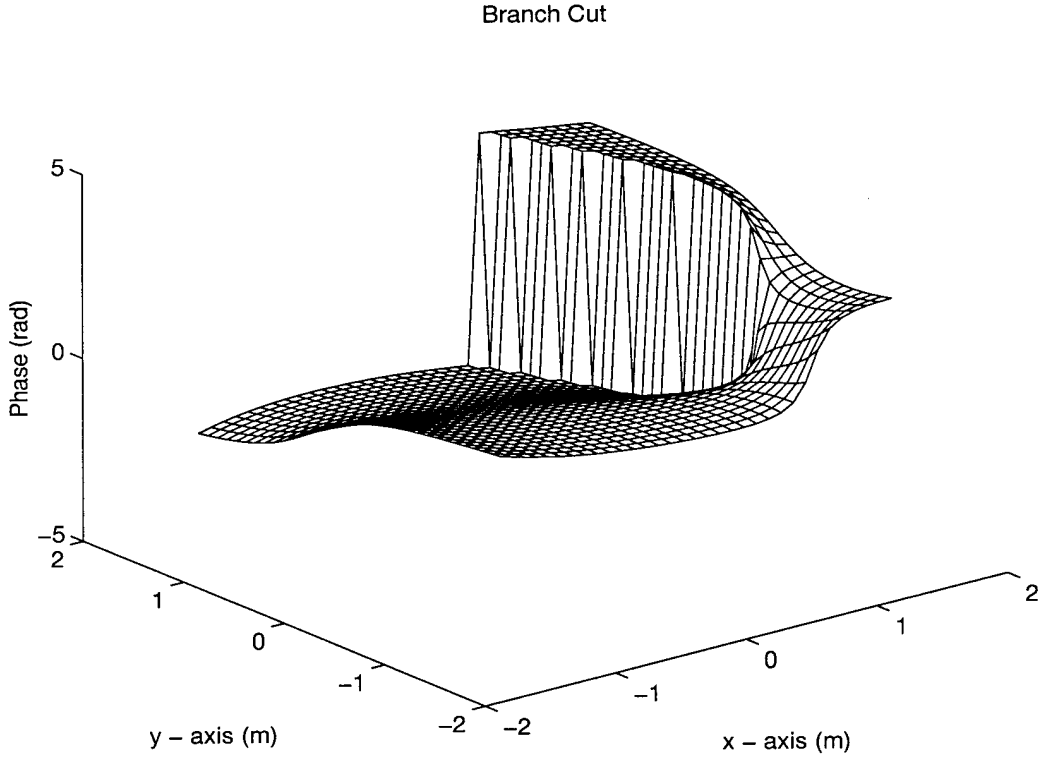


Figure 3. Branch cut in measurement plane phase.

1. Unwrap the measurement plane reference phase to eliminate  $2\pi$  phase ambiguities. The phase differences determined from the unwrapped measurement plane phase map is consistent with the phase differences obtained from the SCIP technique.
2. Provide a representative least squares phase estimator with which to compare simulation results between the conventional least squares and minimum variance formalisms on a grid of points in the measurement plane.

The G & R phase reconstructor minimizes the same error metric as the iterative least squares reconstructors discussed in equation (12). The iterative solution illustrated in equation (12) is re-cast by Ghiglia and Romero into a discrete version of Poisson's equation with Neumann boundary conditions on a rectangular grid [6, 8]. The G & R phase reconstructor is applicable to the coherent phase estimation problem and can reconstruct measurement plane phase maps with branch cut discontinuities. The fast

(non-iterative) nature of the reconstruction process makes the G & R reconstructor a suitable choice for comparing the minimum variance wavefront reconstruction results.

This section has discussed how conventional least squares techniques are used to reconstruct a 2D phase map in the measurement plane of a coherent imaging system. The inputs to the least squares reconstructor can be in the form of phase differences such as those provided by the SCIP technique. The next section provides a brief overview of coherent imaging and illustrates how the 2D phase map provided in the previous section can be combined with spatial amplitude information and processed to produce an image of the object.

### *2.3 Image Formation and Measurement Plane Statistics*

The first section of this chapter discussed how the SCIP technique provides phase difference information on a grid of sample points in the measurement plane of a coherent imaging system. The second section discussed how the phase differences can be used with a conventional least squares reconstructor to estimate the 2D phase map in the measurement plane of the imaging system. This section discusses how a sequence of estimated measurement plane phases can be merged with field amplitudes and processed to produce an image of the object. In addition, motivation of the underlying statistical assumptions required to implement the minimum variance reconstructor will be discussed along with the required aspects of coherent imaging theory. For the purpose of developing the minimum variance reconstructor, the quantity of interest in the object plane is the reflected field. The spatial correlation properties of the reflected field can be used to determine the mutual intensity in the object plane. The mutual intensity is propagated to the measurement plane and converted to the complex coherence factor. The complex coherence factor is used in the minimum variance phase reconstruction process. The clearest approach is to start the discussion in the plane of the object, propagate to the measurement

plane of the imaging system, form the complex field, calculate the image field, and illustrate how the averaged coherent image is formed.

As discussed previously, the three illuminating fields are spatially and temporally coherent with one another in the plane of the object and just prior to making contact with the object. Since the object is man made, the surface of the object is assumed to be rough on the scale of an optical wavelength. The phase of the reflected wave becomes random, having point phase statistics which are uniformly distributed between  $-\pi \leq \phi(\vec{x}_o) \leq \pi$  [13]. The time scales of the measurement process are controlled by the receiver plane detectors and are assumed short enough to freeze a realization of the speckled irradiance pattern. The reflected field can be described by circularly complex Gaussian random variables [9]. This means that the real and imaginary parts of the field are represented by independent, zero mean Gaussian variates with equal variances [13]. For circularly complex Gaussian (CCG) random variables, the variance of the real and imaginary parts of the field is equal to half the ensemble averaged average reflectivity. An additional assumption is that the object is not a strong absorber and that most of the randomization is due to the phase and not the amplitude.

The correlation properties of the reflected field can be used to determine the mutual intensity of the object. The reflected field is assumed uncorrelated with itself for point separations greater than the center wavelength of the illuminating light. Figure 4 shows the coordinate system used between the object and measurement plane. If  $\vec{x}_{o1}$  and  $\vec{x}_{o2}$  are arbitrary points in the object plane then the mutual intensity is given by [13],

$$J(\vec{x}_{o1}, \vec{x}_{o2}) = \langle u(\vec{x}_{o1}, t) u^*(\vec{x}_{o2}, t) \rangle, \quad (13)$$

where  $u$  represents the field, the asterisk represents complex conjugation and the brackets denote the statistical expectation operator. The object plane average re-

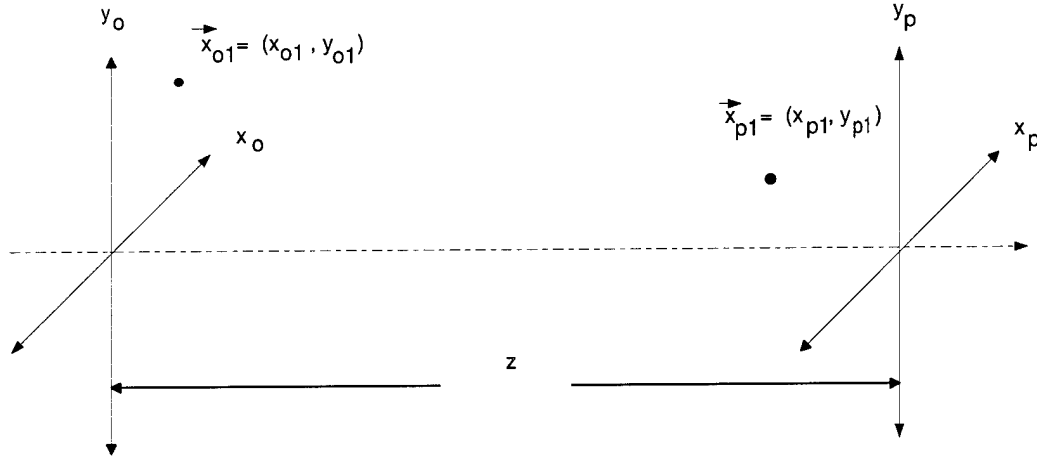


Figure 4. Object to Measurement Plane Coordinate System.

flectivity can be obtained at any point by letting  $\vec{x}_{o1}$  equal  $\vec{x}_{o2}$ . Since the CCG field is assumed to become uncorrelated at spatial separations larger than an optical wavelength, the mutual intensity is non-zero only at points where  $\vec{x}_{o1}$  and  $\vec{x}_{o2}$  coincide. The mutual intensity in the object plane can then be written as,

$$J(\vec{x}_{o1}, \vec{x}_{o2}) = \kappa I(\vec{x}_{o1}) \delta(\vec{x}_{o1} - \vec{x}_{o2}), \quad (14)$$

where  $\kappa = \frac{(\bar{\lambda})^2}{\pi}$  for objects with spatial coherence on the order of the illuminating wavelength and where the resolution of the optical system is coarser than the spatial coherence length [13]. The quantity  $I(\vec{x}_{o1})$  is the ensemble averaged reflectivity at point  $\vec{x}_{o1}$  and  $\delta(\cdot)$  represents a 2D Dirac delta function. The mutual intensity in equation (14) is identical to the mutual intensity for an incoherent source. For the purposes of evaluating the mutual coherence function, the average reflectivity distribution of the object can be considered equivalent to an incoherent radiator. This analogy permits the use of the Van Cittert-Zernike theorem to propagate the mutual intensity from the object plane to the measurement plane [13].

For the case of imaging space based objects from the Earth, the following assumptions are usually satisfied.

1. Source and receiver dimensions are small compared to the separation between the object and measurement plane.
2. Only small angles with respect to the optical axis are involved.
3. Assumptions required for the paraxial approximation are appropriate.

If the above assumptions are valid, then the relationship between the mutual intensity in the measurement (pupil) plane  $\vec{x}_p$  and source (object) plane  $\vec{x}_o$  is given by,

$$J(\vec{x}_{p1}; \vec{x}_{p2}) = \frac{\kappa e^{-j\psi}}{(\bar{\lambda}z)^2} \int_{-\infty}^{\infty} \int_{-\infty}^{\infty} I(\vec{x}_o) \exp \left[ j \frac{2\pi}{\bar{\lambda}z} (\vec{x}_{p1} - \vec{x}_{p2}) \cdot \vec{x}_o \right] d\vec{x}_o. \quad (15)$$

The phase factor,  $\psi$ , is given by,

$$\psi = \frac{\pi}{\bar{\lambda}z} \left[ |\vec{x}_{p1}|^2 - |\vec{x}_{p2}|^2 \right]. \quad (16)$$

As is seen in equation (15), the measurement plane mutual intensity is given by Fourier transforming the incoherent object average reflectivity and evaluating at spatial frequencies,

$$f_x = \frac{(x_{p1} - x_{p2})}{\bar{\lambda}z} \quad \text{and} \quad f_y = \frac{(y_{p1} - y_{p2})}{\bar{\lambda}z}, \quad (17)$$

where,  $x_{p1} - x_{p2}$  and  $y_{p1} - y_{p2}$  is the  $x$  and  $y$  separation along the  $x$  and  $y$  axis in the measurement plane, respectively. The complex coherence factor is obtained by normalizing the mutual intensity in the following fashion,

$$\mu(x_{p1}, y_{p1}; x_{p2}, y_{p2}) = \frac{J(x_{p1}, y_{p1}; x_{p2}, y_{p2})}{\int_{-\infty}^{\infty} \int_{-\infty}^{\infty} I(x_{o1}, y_{o1}) dx_{o1} dy_{o1}}, \quad (18)$$

where  $x_{o1}$  and  $y_{o1}$  are  $x$  and  $y$  coordinates in the object plane, respectively. As will be seen later, the complex coherence factor is required in the determination of the essential phase covariance function in the minimum variance phase reconstruction



formalism. The average irradiance at a point in the measurement plane is obtained by setting the coordinates  $\vec{x}_{p1} = \vec{x}_{p2}$  in equation (15).

The measurement plane field is related to the reflected object field in the Fraunhofer limit by [20],

$$U(\vec{x}_p) = \frac{\exp(jkz)}{j\lambda z} \exp\left[j\frac{k}{2z}|\vec{x}_p|^2\right] \int_{-\infty}^{\infty} \int_{-\infty}^{\infty} U(\vec{x}_o) \exp\left[-j\frac{2\pi}{\lambda z}(\vec{x}_p \cdot \vec{x}_o)\right] d\vec{x}_o, \quad (19)$$

where,  $z$ , is the object plane to measurement plane distance. The parameter  $k = \frac{2\pi}{\lambda}$  is the wave number. The measurement plane field is obtained from the object field by a Fourier transform relationship. The instantaneous irradiance at a given position in the measurement plane can be obtained by Fourier transforming the reflected object field in accordance with equation (19) and multiplying by its complex conjugate. The underlying point statistics of the measurement plane field also obey CCG statistics [10]. Since the expected value of the real and imaginary parts of the measurement plane field are each zero, the magnitude of the field at a given point can assume small values, or be identically zero. The 2D phase of  $U(\vec{x}_p)$  is obtained from equation (19) by the arctangent of the real and imaginary parts of the field at every point,

$$\phi(\vec{x}_p) = \tan^{-1} \left( \frac{\Im(U(\vec{x}_p))}{\Re(U(\vec{x}_p))} \right). \quad (20)$$

The resulting measurement plane phase associated with the regions where the irradiance is zero results in the formation of branch cuts. The field at an observation point reasonably distant from the object consists of the superposition of dephased coherent radiators. The coherent radiators arise from different microscopic coherent elements on the object. The interference of the dephased coherent radiators is the physical process which leads to the formation of granularity or high contrast regions in the measurement plane irradiance [13: 347–359]. This granularity is commonly called the speckle effect.

The combination of the SCIP technique and the minimum variance wavefront reconstructor can be used to estimate the measurement plane field. The relationship between the measurement plane field and the image plane field is also given by a Fourier transform. The image field is formed by spatially Fourier transforming the measurement plane field. The instantaneous image irradiance is given by the modulus squared of the image plane field. The instantaneous image plane irradiance is also speckled. Averaging independent image frames will significantly reduce the amount of speckle in the resulting averaged image.

In Chapter IV, the averaged image irradiance obtained from the synthetic aperture SCIP technique and the minimum variance measurement plane phase estimates are compared to a computer simulated ensemble averaged image irradiance obtained from a filled aperture coherent imaging system. A theoretical description of the statistical properties of the ensemble averaged image irradiance is useful in predicting the results of the coherent imaging process. A linear systems approach is used to relate the statistical properties of the reflected object field to the ensemble averaged image irradiance.

It has been determined that for a coherently illuminated source the underlying probability density function of the reflected object field is that of a circularly complex Gaussian random variable [9]. For a linear, shift invariant system, the image field can be obtained from the object field by convolution,

$$g(\vec{x}_i) = \int_{-\infty}^{\infty} f(\vec{x}_o) h(\vec{x}_i - \vec{x}_o) d\vec{x}_o, \quad (21)$$

where  $h(\cdot)$ , the impulse response of the system, is equal to the appropriately scaled Fourier transform of the measurement plane pupil function [20],  $\vec{x}_o$  is a position vector in the object plane,  $\vec{x}_i$ , is a position vector in the image plane and  $f(\cdot)$  is the object field given by,

$$f(\vec{x}_o) = t(\vec{x}_o) d(\vec{x}_o). \quad (22)$$

The function,  $t(\cdot)$ , is a masking function which provides the 2D object details. The function,  $d(\cdot)$ , is a random diffusive element which embodies the statistics of the field. The object autocorrelation is given by,

$$R_{ff}(\vec{x}_{o1}, \vec{x}_{o2}) = t(\vec{x}_{o1}) t^*(\vec{x}_{o2}) R_{dd}(\vec{x}_{o1} - \vec{x}_{o2}). \quad (23)$$

Here the diffuser amplitude is assumed wide sense stationary. Note that the object field autocorrelation is not stationary.

In computing the image statistics for a diffusely scattering object, the object field autocorrelation width is typically very narrow compared with the impulse response of the optical system. The reflected object field becomes uncorrelated for spatial separations larger than the center wavelength of the illuminating light. This results from the optically rough surface features of the object randomizing the phase of the reflected field. The autocorrelation of the diffusive part of the object field can be approximated by a Dirac delta function,

$$R_{dd}(\vec{x}_{o1}, \vec{x}_{o2}) = \delta(\vec{x}_{o1} - \vec{x}_{o2}). \quad (24)$$

The mean of the image amplitude is found to be zero. This can be seen by taking the ensemble average of the convolution expression above and noting that  $\langle f(\vec{x}_o) \rangle$  is zero. Since the image amplitude mean is zero, the variance of the image amplitude is found to be equal to the mean irradiance.

$$\sigma_g^2(\vec{x}_i) = \langle I(\vec{x}_i) \rangle. \quad (25)$$

The subscript,  $g$ , represents the image plane amplitude. The variance of the real and imaginary parts of the image field are identical and are each equal to half the mean irradiance at the image point of observation [13]. The output autocorrelation

of a linear space invariant system is related to the input auto correlation by [21],

$$R_{gg}(\vec{x}_{p1}, \vec{x}_{p2}) = R_{ff}(\vec{x}_{o1}, \vec{x}_{o2}) * h(\vec{x}_{p1}) * h(\vec{x}_{p2}). \quad (26)$$

By inserting the values for  $R_{ff}(\vec{x}_{o1}, \vec{x}_{o2})$  into the preceding equation the following surface integral over the object plane results,

$$R_{gg}(\vec{x}_{p1}, \vec{x}_{p2}) = \int |t(\vec{x}_{o1})|^2 h(\vec{x}_{p1} - \vec{x}_{o1}) h^*(\vec{x}_{p2} - \vec{x}_{o1}) d\vec{x}_{o1}. \quad (27)$$

The above expression indicates that the image amplitude autocorrelation depends on the impulse response of the system and also the magnitude squared of the transmission function of the object modulating transparency. The mean image irradiance is obtained by letting  $\vec{x}_{p1} = \vec{x}_{p2}$  in equation (27) for the image amplitude autocorrelation,

$$\langle I(\vec{x}_p) \rangle = R_{gg}(\vec{x}_p, \vec{x}_p) = |t(\vec{x}_{o1})|^2 * |h(\vec{x}_p)|^2. \quad (28)$$

This equation indicates that the average transfer function for a coherently illuminated diffuse object is the incoherent optical transfer function. In other words, the mean irradiance of the image for a coherently illuminated diffuse object is the same as if the object were replaced by an incoherent object having the same average reflectivity.

### III. Theory

This chapter introduces the theoretical formalism for the minimum variance reconstructor. In the first section, a generalized error metric is developed which will allow comparison between the minimum variance and least squares class of wavefront reconstructors. The error metric is the aperture averaged mean squared phase error. As will be seen in section 3.1, this error metric is expressed in terms of a system of linear equations which are presented in matrix and vector notation. The governing matrices are the phase difference correlation matrix,  $\Phi_{nm}$ , the elementary function correlation matrix,  $R_{jk}$ , the elementary function/phase/phase difference interaction matrix,  $A_{jn}$ , and the reconstruction matrix,  $M_{jn}$ . The generalized error metric discussed in section 3.1 is expressed in terms of these four matrices and the phase differences obtained from the SCIP technique. The minimum variance formalism determines an optimal reconstruction matrix,  $M_{jn}$ , by minimizing the error metric with respect to the reconstruction matrix elements. The resulting reconstruction matrix is used to estimate a 2D measurement plane phase map which provides the minimum error in terms of the specified error metric. To evaluate all but the elementary function correlation matrix,  $R_{jk}$ , evaluation of the measurement plane phase covariances is required. Section 3.2 develops the phase covariance function required in the generalized error metric of section 3.1. In order to evaluate the generalized error metric, a specific form of the reconstruction matrix,  $M_{jn}$ , must be determined. A derivation of a reconstruction matrix based on the minimum variance formalism is provided in Section 3.3, and Section 3.4 presents a reconstruction matrix based on least squares methods. Substitution of these matrices into the generalized error metric provides for a theoretical comparison of the expected aperture averaged mean squared phase error for the minimum variance and least squares methods. Section 3.5 discusses the computer based implementation of the minimum variance theory

and its functionality. Finally, section 3.6 discusses how additive white Gaussian noise is incorporated in the theoretical model and computer simulation.

### 3.1 Phase Reconstructor and Generalized Error Metric

This section discusses a convenient error metric which provides a means for comparing the minimum variance reconstructor with other reconstructor implementations. Evaluation of the error metric requires knowledge of the measurement plane detection system, a choice of elementary functions, an expression for the measurement plane phase covariance, and an expression for the measurement plane covariance of the noise. For the SCIP process, the measurement system consists of a spatial grid of irradiance sensors. Irradiance measurements are converted to phase differences by the SCIP technique and the phase differences are used as inputs to the minimum variance phase reconstructor. The input phase differences are denoted by,  $\Delta\phi_q(\vec{x}_n)$ , and are defined as [14],

$$\Delta\phi_q(\vec{x}_n) = \phi(\vec{x}_n) - \phi(\vec{x}_n + \vec{s}_q) + n(\vec{x}_n), \quad (29)$$

where  $\vec{x}_n$  is a two-dimensional vector position of the  $n^{th}$  measurement point in the measurement plane of the imaging system. The quantity,  $n(\vec{x}_n)$ , represents zero mean additive white Gaussian noise. The noise and measurement plane phase are assumed to be statistically independent from one another and are uncorrelated with each other. The quantity  $\vec{s}_q$  is the vector shear in either the  $x$  direction, denoted by  $\vec{s}_x$ , or the  $y$  direction denoted  $\vec{s}_y$ . The estimate of the phase,  $\hat{\phi}(\vec{x})$ , is obtained by a linear combination of elementary functions,  $r_j(\vec{x})$ :

$$\hat{\phi}(\vec{x}) = \sum_j c_j r_j(\vec{x}), \quad (30)$$

where  $c_j$  is the weight associated with the  $j^{th}$  elementary function. Gaussian elementary functions of the form,

$$r_j(\vec{x}) = e^{-\frac{|\vec{x}-\vec{x}_j|^2}{R^2}}, \quad (31)$$

were used in the theoretical development and simulation of the minimum variance wavefront reconstructor and the new least squares wavefront reconstructor. The quantity,  $R$ , is an adjustable decay parameter. It is useful to define a vector of ordered phase difference measurements,  $\Delta\phi$ , given by,

$$\Delta\phi = \begin{pmatrix} \Delta\phi_x(\vec{x}_1) \\ \Delta\phi_y(\vec{x}_1) \\ \Delta\phi_x(\vec{x}_2) \\ \Delta\phi_y(\vec{x}_2) \\ \vdots \\ \Delta\phi_x(\vec{x}_M) \\ \Delta\phi_y(\vec{x}_M) \end{pmatrix}, \quad (32)$$

where  $M$  is the total number of sampling elements in the measurement plane, and the  $n^{th}$  element of the  $\Delta\phi$  vector is denoted by  $\Delta\phi_n$ . With the definitions in equation (32), the weighting coefficients,  $c_j$ , in equation (30) are given by a linear combination of the phase difference measurements [14]:

$$c_j = \sum_{n=1}^{2M} M_{jn} \Delta\phi_n, \quad (33)$$

where the matrix,  $M_{jn}$ , maps phase difference measurements to elementary function weights. The matrix,  $M_{jn}$ , is referred to as the reconstruction matrix and has dimensions of  $M \times 2M$ . The proper choice of  $M_{jn}$  can minimize the aperture averaged mean squared phase error between the actual phase and the estimated phase. The error between the true phase at position  $\vec{x}$  in the measurement plane of the imaging

system and the estimated phase at the same spatial location is given by [12],

$$\begin{aligned}\varepsilon(\vec{x}) &= \phi(\vec{x}) - \hat{\phi}(\vec{x}) \\ &= \phi(\vec{x}) - \sum_j \sum_n M_{jn} \Delta\phi_n r_j(\vec{x}).\end{aligned}\tag{34}$$

The mean squared error at a point is formed by squaring the above term and taking the expected value of the result,

$$\begin{aligned}\langle \varepsilon^2(\vec{x}) \rangle &= \langle \phi^2(\vec{x}) \rangle - 2 \sum_j \sum_n M_{jn} r_j(\vec{x}) \langle \phi(\vec{x}) \Delta\phi_n \rangle + \\ &\quad \sum_j \sum_n \sum_k \sum_m M_{km} r_k(\vec{x}) M_{jn} r_j(\vec{x}) \langle \Delta\phi_n \Delta\phi_m \rangle,\end{aligned}\tag{35}$$

where the brackets,  $\langle \cdot \rangle$ , represent the statistical expectation operator. The aperture averaged mean squared phase error is defined by,

$$\langle \varepsilon^2 \rangle = \int_{-\infty}^{\infty} d\vec{x} W_A(\vec{x}) \langle \varepsilon^2(\vec{x}) \rangle.\tag{36}$$

The aperture function,  $W_A(\vec{x})$ , is non-zero inside the clear aperture of the measurement plane, and is zero outside of the clear aperture. It is useful to define the value of  $W_A(\vec{x})$  inside the aperture so that,

$$\int_{-\infty}^{\infty} d\vec{x} W_A(\vec{x}) = 1.\tag{37}$$

By substituting the expression for  $\langle \varepsilon^2(\vec{x}) \rangle$  in (35) into the equation in (36) and interchanging orders of integration and summation, the aperture averaged mean squared phase error is seen to be [12, 22]:

$$\begin{aligned}\langle \varepsilon^2 \rangle &= \sum_j \sum_k \sum_n \sum_m M_{jn} M_{km} \langle \Delta\phi_n \Delta\phi_m \rangle \int_{-\infty}^{\infty} d\vec{x} [W_A(\vec{x}) r_j(\vec{x}) r_k(\vec{x})] \\ &\quad - 2 \sum_j \sum_n M_{jn} \int_{-\infty}^{\infty} d\vec{x} [W_A(\vec{x}) r_j(\vec{x}) \langle \Delta\phi_n \phi(\vec{x}) \rangle]\end{aligned}$$



$$+ \int_{-\infty}^{\infty} d\vec{x} W_A(\vec{x}) \langle \phi^2(\vec{x}) \rangle. \quad (38)$$

Following Wallner [12], considerable notational simplification in equation (38) results by making the following identifications,

$$\begin{aligned} R_{jk} &= \int_{-\infty}^{\infty} d\vec{x} [W_A(\vec{x}) r_j(\vec{x}) r_k(\vec{x})], \\ A_{jn} &= \int_{-\infty}^{\infty} d\vec{x} [W_A(\vec{x}) r_j(\vec{x}) \langle \Delta \phi_n \phi(\vec{x}) \rangle], \\ \langle \varepsilon_0^2 \rangle &= \int_{-\infty}^{\infty} d\vec{x} [W_A(\vec{x}) \langle \phi^2(\vec{x}) \rangle], \\ \Phi_{nm} &= \langle \Delta \phi_n \Delta \phi_m \rangle. \end{aligned} \quad (39)$$

Inserting the above identifications into equation (38) leads to,

$$\langle \varepsilon^2 \rangle = \sum_j \sum_n \sum_k \sum_m M_{jn} M_{km} R_{jk} \Phi_{nm} - 2 \sum_j \sum_n M_{jn} A_{jn} + \langle \varepsilon_0^2 \rangle. \quad (40)$$

The above generalized error metric represents the aperture averaged mean squared phase error in the measurement plane of the imaging system. Equation (40) provides the theoretical basis of comparison for the least squares and minimum variance formalisms. In order to evaluate the error expression in equation (40), expressions for the reconstruction matrix,  $M_{jn}$ , the phase covariance,  $\langle \phi(\vec{x}) \phi(\vec{x}') \rangle$ , and the noise covariance,  $\langle n(\vec{x}) n(\vec{x}') \rangle$ , must be determined. The requirement for an expression for the noise covariance stems from substituting the phase differences in equation (29) into the last term of equation (39). An expression for the noise covariance is given later in this chapter. The reconstruction matrix,  $M_{jn}$ , depends on the optimization method used (least squares, minimum variance) and will be discussed shortly. The determination of an expression for the measurement plane phase covariance is discussed first.

### 3.2 Measurement Plane Phase Covariance

In order to evaluate the minimum variance optimal reconstruction matrix and the subsequent expected minimum error, it is necessary to determine the phase correlation function,  $\langle \phi(\vec{x}) \phi(\vec{x}') \rangle$ . An expression for the phase correlation function is required in evaluating the expectations in equation (39).

The correlation function of the phase is given by [11]:

$$\langle \phi(\vec{x}) \phi(\vec{x}') \rangle = \pi^2 \left[ 1 + 2\gamma - 4\gamma^2 + \frac{1}{12} \Omega(\mu_0) \right] - \pi^2, \quad -\pi \leq \phi(\vec{x}), \phi(\vec{x}') \leq \pi, \quad (41)$$

where,

$$\gamma \equiv \frac{1}{2\pi} \sin^{-1} \mu_0,$$

and,

$$\Omega(\mu_0) \equiv \frac{6}{\pi^2} \sum_{n=1}^{\infty} \frac{\mu_0^{2n}}{n^2}.$$

In equation (41), the coordinates  $\vec{x}$  and  $\vec{x}'$  are arbitrary points in the measurement plane. The parameter  $\mu_0$  is the complex coherence factor of the object and is given by,

$$\mu_0(\vec{x}, \vec{x}') = \left| \frac{\langle u(\vec{x}) u^*(\vec{x}') \rangle}{\sqrt{\langle u(\vec{x}) u^*(\vec{x}) \rangle \langle u(\vec{x}') u^*(\vec{x}') \rangle}} \right|, \quad (42)$$

where the asterisk represents complex conjugation, the parameters  $u(\vec{x})$  and  $u(\vec{x}')$  represent the measurement plane field at coordinates  $\vec{x}$  and  $\vec{x}'$ ,  $\langle \cdot \rangle$  represents the statistical expectation operator, and the spatial dependence of  $\mu_0$  is suppressed in equation (41).

Middleton's theory applies to arbitrarily shaped objects. However, for the results presented in Chapter IV, the theoretical object emittance distribution was assumed to be a Gaussian with infinite spatial extent. An object with a Gaussian

emittance distribution has a complex coherence factor given by [14],

$$\mu_0(\Delta x, \Delta y) = \exp\left(-\pi \frac{R_x^2}{(\bar{\lambda}z)^2} (\Delta x)^2\right) \exp\left(-\pi \frac{R_y^2}{(\bar{\lambda}z)^2} (\Delta y)^2\right), \quad (43)$$

where  $\Delta x$  and  $\Delta y$  are coordinate differences in the measurement plane given by  $x_1 - x_2$  and  $y_1 - y_2$ , respectively. The parameter  $\bar{\lambda}$  is the center wavelength of the illuminating laser and  $z$  is the object to measurement plane distance. The quantities  $R_x$  and  $R_y$  are decay parameters for the Gaussian object average reflectivity in the  $x$  and  $y$  directions of the object plane, respectively. This section discussed the determination of the phase covariance function required for the evaluation of equation (40). The measurement plane phase covariance is also required to determine the minimum variance optimal reconstruction matrix discussed in the next section.

### 3.3 Minimum Variance Reconstruction Matrix

Evaluation of the generalized error metric developed in Section 3.1 requires expressions for the measurement plane phase covariance and the reconstruction matrix,  $M_{jn}$ . This section presents a specific form of  $M_{jn}$  which provides the optimal reconstruction matrix in a minimum variance sense.

The aperture averaged mean squared phase error can be minimized by proper choice of the reconstruction matrix,  $M_{jn}$ . This minimization is accomplished by differentiating equation (40) with respect to the elements of  $M_{jn}$ , setting the result equal to zero, and solving for  $M_{jn}$ . This analysis has been accomplished and leads to an optimum reconstruction matrix given by [12, 22],

$$M_{jn} = \sum_k \sum_m R_{jk}^{-1} \Phi_{nm}^{-1} A_{km}, \quad (44)$$

where the notation,  $R_{jk}^{-1}$  represents the  $j^{th}$  row and the  $k^{th}$  column element of the inverse of the  $R$  matrix and  $\Phi_{nm}^{-1}$  represents the  $n^{th}$  row and  $m^{th}$  column element

of the inverse of the  $\Phi$  matrix. This choice of  $M_{jn}$  is referred to as the minimum variance reconstructor because it explicitly minimizes the aperture averaged variance of the error. The aperture averaged mean squared phase error associated with  $M_{jn}$  is,

$$\langle \varepsilon^2 \rangle_{\min} = \langle \varepsilon_0^2 \rangle - \sum_j \sum_n M_{jn} A_{jn}. \quad (45)$$

The above equation can be written as [22],

$$\langle \varepsilon^2 \rangle_{\min} = \langle \varepsilon_o^2 \rangle - \sum_j \sum_n \sum_k \sum_m R_{jk}^{-1} A_{km} \Phi_{nm}^{-1} A_{jn}. \quad (46)$$

Equation (46) represents the minimum aperture averaged mean squared phase error obtained from the minimum variance solution to the phase reconstruction problem. The reconstruction matrix,  $M_{jn}$ , in equation (44) is used in equation (30) to determine the optimal weighting coefficient,  $c_j$ , leading to the 2D measurement plane phase estimates. Besides the minimum variance solution to the measurement plane phase reconstruction problem, a least squares formalism can be used to determine a different reconstruction matrix. The least squares reconstruction matrix,  $M_{jn}^{LS}$ , can also be used to evaluate the aperture averaged mean squared phase error in equation (40) and estimate the measurement plane phase in equation (30). In Section 3.4, the least squares reconstruction matrix is determined.

### 3.4 Reconstruction Matrix for New Least Squares Reconstructor

It is possible to define a least squares reconstructor which minimizes the sum of the squared error between the true phase differences and the reconstructed phase differences in the aperture without use of the statistical properties of the random scattered field [4, 18, 23]. The error metric which is minimized is different than the error metric discussed in Section 2.2. The reconstructors discussed in Section 2.2 minimize the difference between the true and reconstructed phases and not the true and reconstructed phase differences as discussed in this section. This least squares

implementation is useful in that an optimal reconstruction matrix is generated which is used to estimate the theoretical aperture averaged mean squared phase error given in equation (40). Good agreement between the theoretical errors developed in this section and simulated results based on the conventional least squares reconstructor discussed in Section 2.2 should, in general, not be expected due to the error metric differences. To compare the theoretical results in this section to simulation, the minimum variance formalism needs to be recast in terms of the phase estimation paradigm given in equation (30) and the error metric used in this section. The analysis for using the aperture averaged mean squared phase difference error in the minimum variance wavefront reconstructor has been accomplished during the course of this research. However, implementation of the minimum variance wavefront reconstructor based on the aperture averaged mean squared phase difference error metric was found to be too computer intensive for current use. The least squares implementation in this section provides the ability to generate a representative theoretical aperture averaged mean squared phase error curve as a function of the sampling parameter,  $\beta$ . The theoretical aperture averaged mean squared phase error results can be used to predict relative performance between the minimum variance and new least squares methods.

Because least squares reconstructors do not require knowledge of statistics they are computationally much simpler to implement than minimum variance techniques. However, in the adaptive optics field, least squares reconstruction has been shown to give lower performance than minimum variance reconstruction [23]. The least squares phase reconstructor discussed below takes the general form given in equations (30) through (33). However a different reconstruction matrix is used for the least squares technique. The derivation of the least squares reconstruction matrix has been previously accomplished. The critical elements of this derivation are repeated as it applies to a SCIP phase reconstructor. To start, the error between the measured phase differences and the phase differences arising from a given set of elementary

function weights is given by,

$$\Delta = \Delta\phi - Hc^{LS}, \quad (47)$$

where  $\Delta\phi$  is the vector of ordered phase difference measurements given in equation (32),  $H$  is the Jacobian matrix, and  $c^{LS}$  is a vector of weighting coefficients.

The elements,  $h_{nj}^q$ , of the Jacobian matrix,  $H$ , which relate the change in the output signal of the  $n^{th}$  measurement plane sampling element in the  $q^{th}$  direction of sensitivity,  $\Delta\phi_q(\vec{x}_n)$ , to the change in the  $j^{th}$  weighting coefficient,  $c_j$  are given by,

$$h_{nj}^q = \frac{\partial \Delta\phi_q(\vec{x}_n)}{\partial c_j} = [r_j(\vec{x}_n) - r_j(\vec{x}_n + s_q)]. \quad (48)$$

In the above equation, the phase differences in the partial derivative are given by equation (29) and the constituent phases are given by,  $\phi(\vec{x}_n) = \sum_j c_j r_j(\vec{x}_n)$ . Equation (48) gives the sensitivity of the phase differences,  $\Delta\phi_q(\vec{x}_n)$ , to a change in the weighting coefficients,  $c_j$ . The error metric which is minimized for this implementation of the least squares formalism is given by,

$$\|\Delta\|^2 = \Delta^T \Delta, \quad (49)$$

where  $\|\Delta\|^2$  is the normed squared error of  $\Delta$  and  $T$  represents the transpose operator. The least squares reconstructor finds  $c^{LS}$  as a function of  $\Delta\phi$  which minimizes the sum of squares of the components of the error [19],

$$c^{LS} = (H^T H)^{-1} H^T \Delta\phi. \quad (50)$$

By comparing equation (50) with equation (33), the least squares reconstruction matrix for the least squares reconstructor is seen to be,

$$M_{jn}^{LS} = (H^T H)^{-1} H^T. \quad (51)$$

By substituting the above reconstruction matrix for that obtained by the minimum variance derivation in equation (40), theoretical comparisons between the two phase reconstruction methods can be made. Conclusions must be carefully drawn since the error metric for the theoretical minimum variance and least squares formalisms are different. The implementation and testing of the computer based theoretical and simulated comparisons are discussed in the next section.

### 3.5 Minimum Variance Implementation and Testing

This section discusses the implementation of the minimum variance reconstructor. The assumptions required to tie the physical processes to computer simulation are presented. The presentation follows the development of Chapter II in that the modeling process starts with the reflected object field. The reflected field is then propagated to the measurement plane using equation (19) implemented with Fast Fourier Transforms (FFT's) and a 2D reference phase map is generated. The phase at any measurement plane point lies in the range  $-\pi \leq \phi(\vec{x}_p) \leq \pi$ . The reference phase map has  $2\pi$  discontinuities resulting from both branch cuts, as illustrated in Figure 3, and phase wraps. The phase differences obtained from the reference map lie in the range  $-2\pi \leq \Delta\phi_q(\vec{x}_p) \leq 2\pi$ . The reference phase  $2\pi$  discontinuities associated with branch cuts and phase wraps are unwrapped with a 2D phase unwrapping utility [6]. The unwrapped phases are referred to as measurement plane true phases. Phase differences are formed from the true phase in a manner consistent with the SCIP measurement process in equations (1) - (10). The phase differences formed from the unwrapped phase lie in the range  $-\pi \leq \Delta\phi_q(\vec{x}_p) \leq \pi$ . The phase differences are input to the minimum variance reconstructor and a 2D reconstructed phase map is generated in the measurement plane. The phase maps are combined with amplitude information from the measurement plane field and the respective true and reconstructed measurement plane fields are determined. These fields are propagated to the image plane using equation (19) implemented with FFT's where

speckled instantaneous images are made for the true and reconstructed fields. In using equation (19), the object plane coordinates are replaced by the measurement plane coordinates and the measurement plane coordinates are replaced with the image plane coordinates. Averaging of the image irradiance is used to reduce the speckle noise and produce the incoherent image.

The modeling process starts in the object plane illustrated at the top right corner of Figure 5. The reflected object field is modeled by circularly complex Gaussian (CCG) statistics. To represent the reflected field on a computer the field must be spatially sampled on a 2D grid of points. For the SCIP technique, the measurement plane aperture is assumed to be a square enclosing the measurement plane sampling elements. The length of a side of the enclosing square aperture is assumed to be  $D$  m. There are  $N$  by  $N$  measurement plane sampling elements evenly spaced within the aperture. The performance of the minimum variance reconstructor is compared to a diffraction limited coherent imaging system by computer simulation. The clear aperture of the computer simulated coherent imaging system (reference imaging system) is the same as the aperture enclosing the SCIP measurement plane sampling elements. The diffraction limited resolution is the same for both the SCIP imaging system and the diffraction limited imaging system. The spacing between the points of the sampled reflected object field should be less than the diffraction limited resolution of the reference imaging system to prevent granularity in the reconstructed image. The center wavelength,  $\bar{\lambda}$ , of the illuminating beams is assumed to be  $1.3 \mu\text{m}$ . The length,  $D$ , of one side of the square measurement plane collecting aperture is 3 m. With an object to measurement plane distance,  $z$ , of  $10^6$  meters, the diffraction limited resolution,  $2\frac{\bar{\lambda}}{D}z$ , of both imaging systems with square collecting apertures [20: page 63] is seen to be 0.8667 m. The sample spacing in the object plane was 0.2167 m. The value of the reflected field on the 2D grid of points in the object plane is determined by associating with every spatial point a random complex number. For each 2D spatial coordinate, the real and imaginary part of the complex number



# Reconstruction Flow Diagram

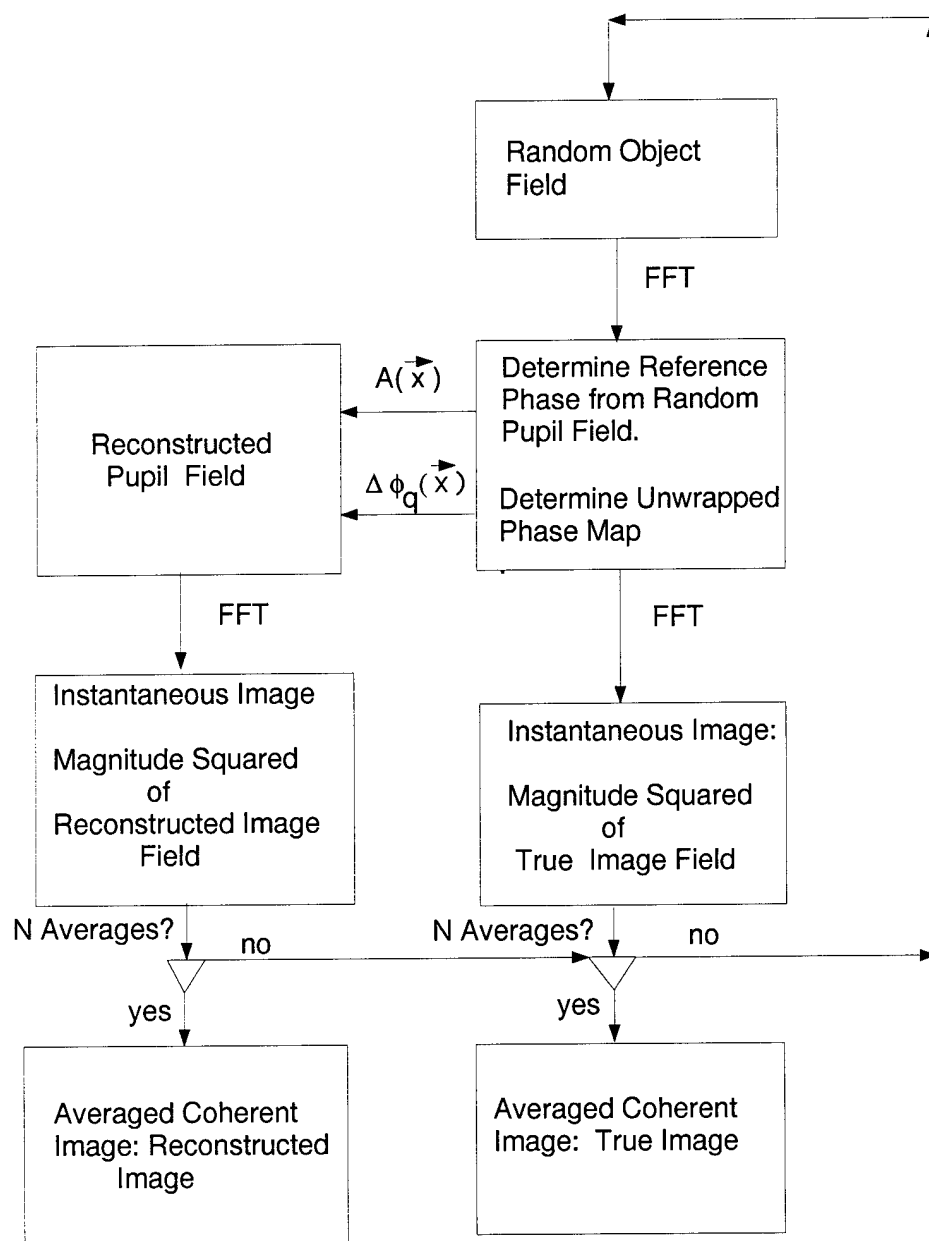


Figure 5. Modeling process.

consist of independent random draws from a Gaussian distribution with zero mean and equal variance. The variance of the real and imaginary parts of the reflected object field is set to half the time averaged emittance at that particular spatial location. The spatial field distribution generated in this fashion corresponds to one realization of the random process. The digital representation of the reflected field was centered in a 64 by 64 array otherwise filled with zeros.

Propagation of the reflected field from the object to the measurement plane is accomplished by using the principle of Fraunhofer diffraction illustrated in equation (19). An FFT was used to convert the reflected object field into the instantaneous measurement plane field. The reference phase map is obtained by calculating the phase at each sampled point of the measurement plane reference field in accordance with equation (20). The sample spacing in the measurement plane,  $\Delta x_m$  is given by,

$$\Delta x_m = \frac{1}{M} \frac{\bar{\lambda} z}{\Delta x_o}, \quad (52)$$

where  $M$  is the total number of FFT points in the  $x$  linear direction and  $\Delta x_o$  is the sample spacing in the object plane. For an FFT using 64 points in a linear direction and the preceding parameters, the grid of points in the measurement plane (fine grid) has a sample spacing of 0.09375 m. The fine grid was used in the reconstruction process to provide reference phase maps with which to compare the reconstructed phases. The phase reconstructions illustrated in the results section are limited by processing speed and are accomplished on a coarser grid in the measurement plane. The sampling grid associated with the phase reconstruction process uses an 8 by 8 array of points (coarse grid) in the measurement plane of the imaging system. Sample spacing on the coarse grid is 0.375 m in a linear direction.

The phase differences for the minimum variance reconstructor must be calculated using the unwrapped reference phase (measurement plane true phases or true phases for brevity) on the coarse grid to reflect limitations in the measurement system. The reference phase differences lie in the range of  $\pm 2\pi$  and must be

unwrapped to the range of  $\pm\pi$  for consistency with the SCIP detection process. Measurement plane reference phase values whose magnitude exceeds  $\pi$  are wrapped by the detection process into their principal ranges ( $\pm\pi$ ). Since the reference phases are restricted to this principal range, the phase differences determined from the reference field phase can not have magnitudes exceeding  $2\pi$ . The phase differences obtained from the true phase map are equivalent to those that are obtained from the SCIP technique and can not have magnitudes exceeding  $\pi$ .

The reference phase differences are also calculated on the fine grid and used in conjunction with the G & R least squares phase unwrapper [6] to provide a high resolution true phase map in the measurement plane. Both the reference phase map and the true phase map are used to compare the results from the minimum variance phase estimation process to the new least squares and a conventional least squares wavefront reconstructors. The G & R least squares phase unwrapper is based on solving Poisson's equation in two dimensions with Neumann boundary conditions. The mathematical development is identical to the path integral based iterative least squares phase reconstructors discussed in Chapter II. Therefore, the phase unwrapper can be used as a wavefront reconstructor on the coarse grid of measurement plane sample points allowing for a direct simulation comparison between the conventional least squares and minimum variance formalisms.

By using the weighted elementary functions in equation (31) which exist everywhere in the aperture in the minimum variance formalism and in a new implementation of the least squares method, the values of the phase at any arbitrary position in the aperture of the measurement plane can be interpolated. Conventional least squares approaches discussed in Section 2.2 do not provide this feature but rather can only estimate the phase on a coarse measurement grid of points. The values of the measurement plane phase are determined at every point on the fine grid allowing for a comparison between the reconstructed phase from the minimum variance formalism, the true phase, and the new implementation of the least squares phase.

The fine phase grid consists of an array of 33 by 33 points. The point phases are combined with point amplitudes from the true field to form the measurement plane field. The effects of the measurement plane aperture are included by embedding the field within the 33 by 33 point clear aperture of the imaging system in a 64 by 64 matrix of zeros. Propagation from the measurement plane to the image plane is accomplished by a 2D FFT. The instantaneous image irradiance is determined by taking the pointwise magnitude squared of the resulting image field.

The resulting instantaneous image irradiance is often disappointing since it rarely resembles the time averaged reflectivity profile of the object. This is because of the presence of speckle in the instantaneous image irradiance. Image plane averaging is used to approximate the image irradiance given by equation (28) and reduce the amount of speckle in the image. One hundred statistically independent realizations of the instantaneous image irradiance, when point wise averaged together, are found to produce similar images as those produced from a simulated noise free diffraction limited coherent imaging system.

To test the minimum variance reconstructor, the throughput and non-statistical aspects of the implementation were checked, the essential equations in the determination of the optimal reconstruction matrix,  $M_{jn}$ , were tested, and a reconstruction of a simple target was performed. These steps were performed to gain confidence in the reconstructor prior to attempting more complicated extended objects.

To check the throughput of the minimum variance reconstructor, a measurement plane phase map corresponding to a deterministic object was reconstructed. This was accomplished by choosing a test case which produced a deterministic phase correlation function. The deterministic phase correlation function was used in the minimum variance wavefront reconstructor. By choosing an off-axis point source for an object model, the expected phase map in the measurement plane is deterministic, and is given by a tilted plane. Figure 6 shows a comparison of the measurement plane phase for the (a) true phase and (b) reconstructed phase for an off-axis point source.

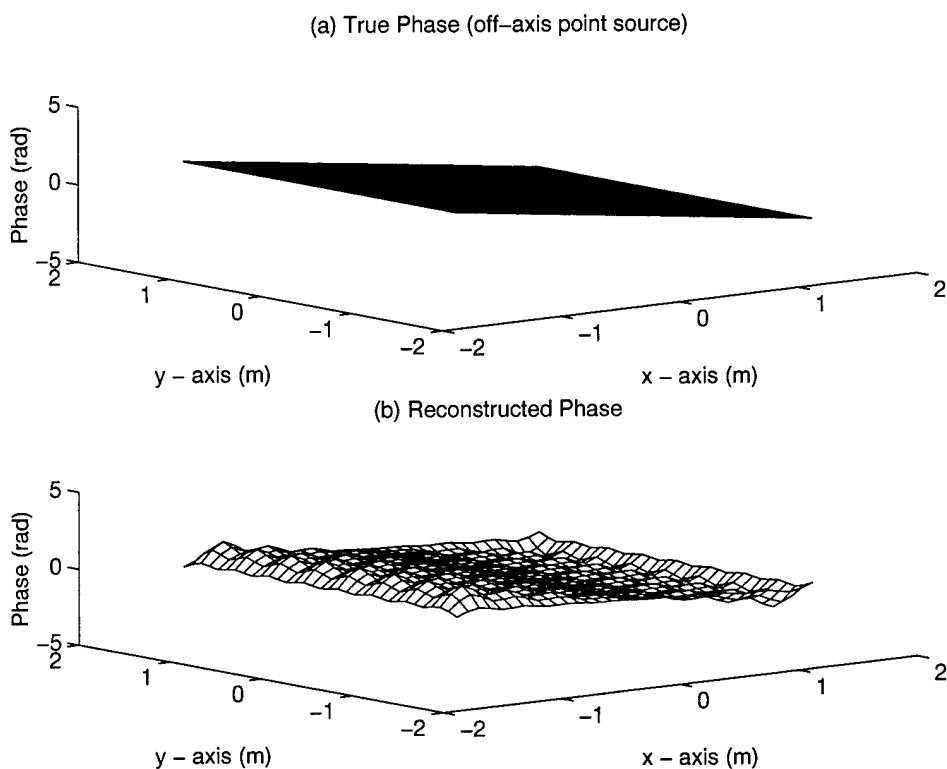


Figure 6. (a) True phase and (b) reconstructed phase for deterministic off-axis point source object.

The point source was displaced in the  $x$  direction by 0.2167 m. The reconstructed phase appears similar to the true phase. A grid of 8 by 8 sample points were used in an equally spaced 3 m by 3 m measurement plane collecting aperture. The center locations of the elementary functions are visible in the reconstructed phase.

To better observe the similarity between the true and reconstructed phase maps in Figure 6, a plot of the phase error squared between the true and reconstructed phases is in order. Figure 7 shows a point by point plot of the squared difference between the true and reconstructed phase maps. The errors along the edges are from the reduced number of neighboring sample points available to make the estimate as compared to sample points in the interior of the clear aperture. Apart from the edges, good agreement between the true and reconstructed phase maps is evident.

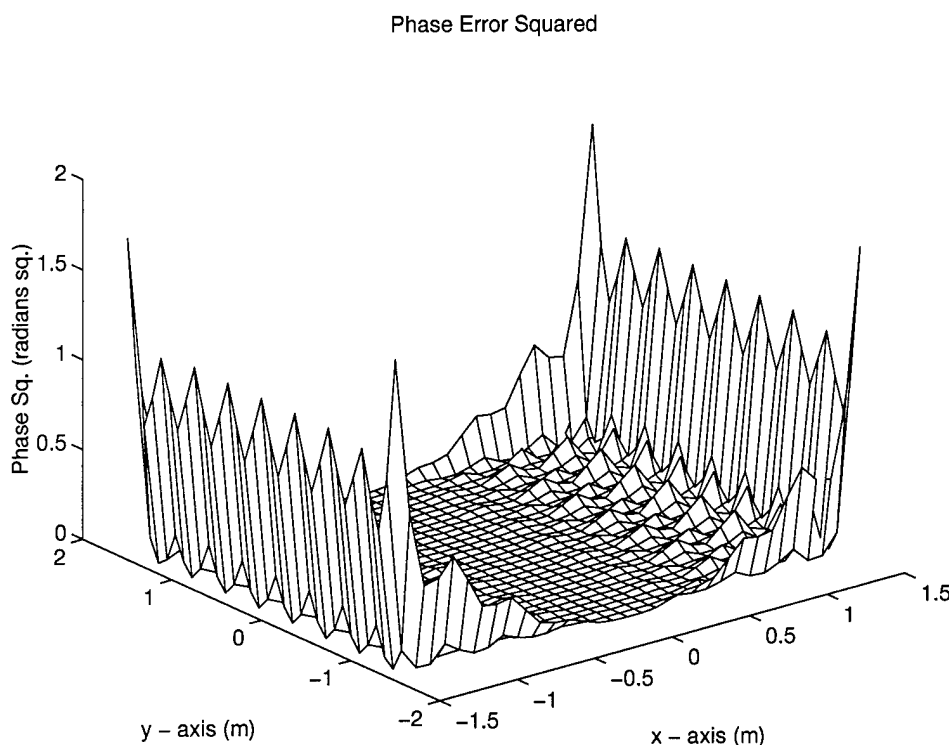


Figure 7. Off-axis point source phase error squared.

The reasonable match between the true and reconstructed phases indicates that the minimum variance simulation works for simple deterministic objects.

The phase covariance determination in the reconstructor was tested by independently implementing all the governing equations of the minimum variance reconstructor. Mathematica [24] and MathCad [25] were used to check the governing equations of the minimum variance wavefront reconstructor. The equations for,  $\Phi_{nm}$ ,  $R_{jk}$ , and  $A_{jn}$  were each independently checked and shown to be accurate to the fourth significant figure. The precision requirement was based on processing time limitations in the prototype version of the reconstructor. A test case was generated to demonstrate the functionality of the reconstructor and test the image formation process.

A test case which demonstrates the ability of a reconstructor to reproduce ridge discontinuities is a phase map arising from a double point source object. The

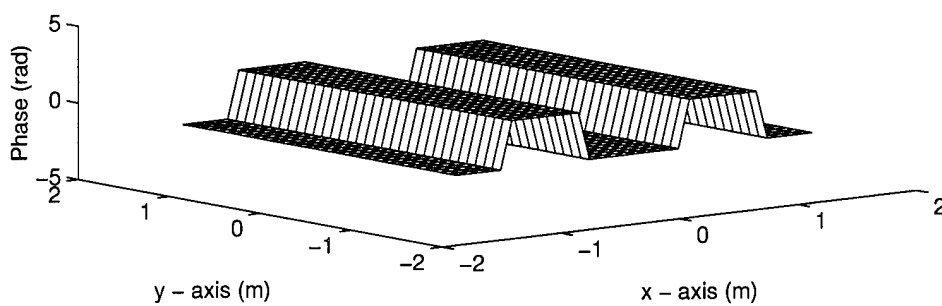
phase map from a double point source (DPS) object is illustrated in Figure 8 (a). The separation of the object point sources was  $1.733 \mu\text{rad}$ . The true phase map shows sharp ridge discontinuities. Figure 8 (b) shows the reconstructed phase for one measurement frame. There were 8 measurement plane samples used in a linear direction (64 total samples). As expected, the reconstructed phase map is similar to a low pass version of the true phase depicted in (a).

To demonstrate that the image formation process was correctly implemented, the true and reference phase maps in Figure 8 were combined with the known field amplitudes and processed to produce the instantaneous image. Figure 9 (a) shows the true image for one frame of data. The true image was obtained by Fourier transforming the measurement plane true field, multiplying the result by its complex conjugate, and normalizing by dividing by the on-axis irradiance. Figure 9 (b) shows the instantaneous reconstructed image. To obtain the single realization reconstructed image, the identical procedure as for the true image was used except the reconstructed phase was substituted for the true phase.

The prominent features of the double point source are recognizable in the reconstruction. The additional structure in the reconstructed image is due to the effect of the aperture and the imperfect reproduction of the step discontinuities. Decreasing the sample spacing,  $L_x$  and  $L_y$ , in the measurement plane would improve the appearance of the reconstructed image.

This section has illustrated that the reconstructor is implemented in accordance with the governing equations and that it is sensitive to step discontinuities in the measurement plane phase function. The production of a double point source image indicates that throughput and scaling issues have been satisfactorily addressed. The next section discusses how additive noise is included in both the governing equations and in the simulation.

(a) True Phase (double point source)



(b) Reconstructed Phase

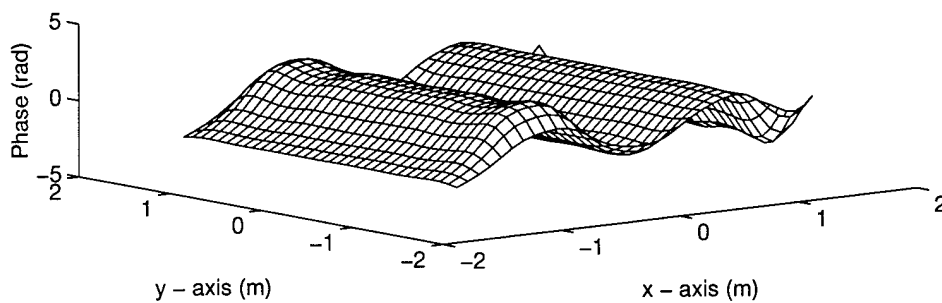


Figure 8. (a) True phase and (b) reconstructed phase for double point source object with  $1.7333 \mu\text{rad}$  separation.



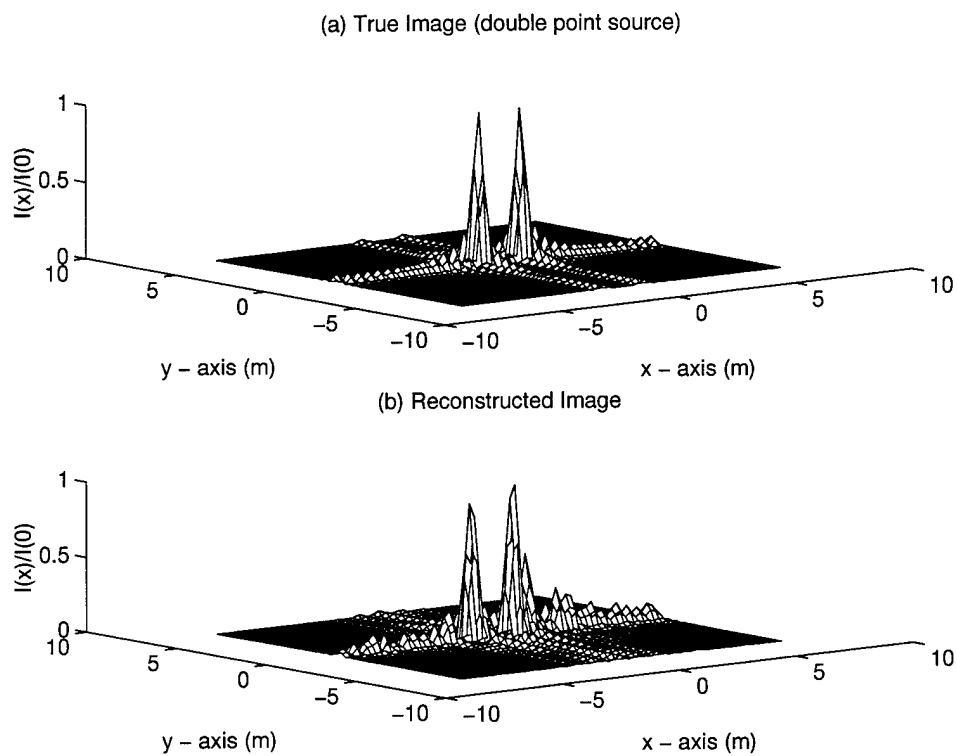


Figure 9. Double point source (a) true image and (b) reconstructed image for point source separation of  $1.7333 \mu\text{rads}$ .

### 3.6 Additive Noise

This section discusses how noise effects are incorporated in both the theory and computer simulation. The detection elements in the measurement plane are assumed point detectors such as photo diodes. The noise is assumed to be zero mean additive white Gaussian noise such as is seen in photon noise limited detectors. The governing equations of the minimum variance wavefront reconstructor depend on the covariance of the phase. Since the noise is assumed additive, the correlation of the noise is required to assess the impact of the noise on the minimum variance reconstruction process. Simultaneous measurements of orthogonal slopes from the same wavefront are uncorrelated. Mathematically these conditions are expressed as [12],

$$\langle n(\vec{x}) n(\vec{x}') \rangle = k_{nm} \sigma_n^2 \delta(\vec{x}_n - \vec{x}_m), \quad (53)$$

where  $\langle n(\vec{x}) n(\vec{x}') \rangle$ , represents the correlation of the noise,  $k_{nm}$ , is a Kronecker delta function arising from the correlation properties from separate wavefronts,  $\sigma_n^2$ , is the variance of the noise at the  $n^{th}$  sample point in the measurement plane,  $\delta(\cdot)$  represents a delta function and  $\vec{x}_n$  and  $\vec{x}_m$  are discrete spatial locations in the measurement plane.

The noise is assumed to be uncorrelated with the wavefront phase. These correlation properties indicate that the only affected term in the governing equations of the minimum variance wavefront reconstructor is that for the correlation of the phase differences,  $\Phi_{nm}$ , in equation (39). To incorporate the effects of additive white Gaussian noise in the theoretical development of the minimum variance reconstructor, the noise variance in equation (53),  $\sigma_n^2$ , is added to all the diagonal elements of the phase difference correlation matrix,  $\Phi_{nm}$ . The noise does not affect the other terms in equation (39). The noise variance for all the separate diagonal matrix elements of  $\Phi_{nm}$  are assumed identical.

To include the effects of additive white Gaussian noise in the computer simulations, a separate Gaussian random number with zero mean and variance of  $\sigma_n^2$  is added to each of the phase differences obtained from the SCIP measurement process. Random Gaussian noise draws are added to both  $x$  and  $y$  phase differences at each sample point in the measurement plane leading to  $2N^2$  random noise contributions for each data frame.

This chapter has developed the theoretical foundation for the minimum variance wavefront reconstructor. A generalized error metric was developed allowing for the comparison of the minimum variance and least squares formalisms. Evaluation of the error metric required an expression for the phase covariance, a specific choice for a reconstruction matrix,  $M_{jn}$ , and an expression for the noise covariance,  $\langle n(\vec{x}) n(\vec{x}') \rangle$ . An expression for the phase covariance was developed as well as reconstruction matrices for both the minimum variance and least squares wavefront reconstruction processes. The minimum variance reconstructor was implemented and tested on a deterministic test case. An off-axis point source reconstruction showed that the reconstructor worked for the case of a simple deterministic object with no measurement noise. Separate implementations of the governing equations from the minimum variance wavefront reconstructor showed that the statistically based algorithms in the reconstructor matched the theoretical expressions developed in this chapter. The reconstructed image of a double point source object was shown to compare favorably to a computer simulated image that would have been obtained from the DPS object using a 3 m by 3 m filled (square) collecting aperture. Finally, the incorporation of additive white Gaussian noise in theory and in simulation was presented.

## IV. Results

This section demonstrates the performance of the minimum variance reconstructor discussed in Chapters I through III. Throughout this chapter, it is important to distinguish between two types of phase maps in the Fraunhofer plane of the object. The reference phase map is the actual phase in the far field of the object. For the reference phase map, the phases are wrapped into their principal range of  $-\pi \leq \phi(\vec{x}) \leq \pi$  where  $x$  is a coordinate in the measurement plane. Phase differences given by equation (6) calculated from the reference phase lie in the range,  $-2\pi \leq \Delta\phi_q(\vec{x}) \leq 2\pi$ , where  $q$  is the direction of the measurement plane shear ( $x$  or  $y$ ). The other measurement plane phase map considered in this chapter is the unwrapped reference phase map. The unwrapped reference phase map is referred to as the true phase map. For the true phase map, the phase differences from equation (6) are wrapped into the range  $-\pi \leq \Delta\phi_q(\vec{x}) \leq \pi$  by equation (10).

In demonstrating the performance of the minimum variance wavefront reconstructor, it is reasonable to have prior knowledge about gross object features such as the approximate size and shape of the object. It is not reasonable to expect to have detailed information about the surface features and average reflectivity profile of the object. For these reasons, a Gaussian envelope function with infinite extent was used to model the object average reflectivity in the theoretical development of the minimum variance wavefront reconstructor. In this analysis, a Gaussian object is assumed to be illuminated by a plane wave. For all of the phase and image reconstructions presented in Chapter IV, the theoretical object is assumed to produce a spatially Gaussian average reflectivity profile with infinite spatial extent. The effect of a mismatch between the theoretical (Gaussian object) and simulated (truncated Gaussian object) on the aperture averaged mean squared phase error is characterized in Section 4.4. For the theoretical development of the minimum variance wavefront reconstructor, the average reflectivity at any spatial point on the object was assumed

to be given by,

$$I(x_o, y_o) = I(0, 0) \exp\left(-\pi \frac{(x_o)^2}{R_x^2}\right) \exp\left(-\pi \frac{(y_o)^2}{R_y^2}\right). \quad (54)$$

The coordinates,  $x_o$  and  $y_o$ , define an observation point in the object plane. The parameters  $R_x$  and  $R_y$  were chosen so that the average reflectivity along the outer edge of the angular subtense of the object assumed the value of  $e^{-1}$  of the on axis average reflectivity,  $I(0, 0)$ . The Gaussian average reflectivity profile was used throughout this chapter to estimate the measurement plane phase covariances and calculate the optimal reconstruction matrix,  $M_{jn}$ .

In the measurement plane, two types of phase maps were used in the comparison of the minimum variance wavefront reconstructor to both the new least squares and conventional (G & R) least squares wavefront reconstructors. The first type of phase map was referred to as the reference phase map. The reference phase was determined by evaluating equation (20) at every point on the fine grid in the measurement plane. The reference phase differences lie in the range of  $-2\pi \leq \Delta\phi_q(\vec{x}) \leq 2\pi$ . The reference phase has both  $2\pi$  discontinuities associated with branch cuts and phase wraps and so the simulated aperture averaged mean squared phase error will be too high. The phase wraps should be removed prior to calculating the simulated aperture averaged mean squared phase error. The second type of phase map used to compare the minimum variance wavefront reconstructor to both the new least squares and the G & R least squares wavefront reconstructors was obtained by unwrapping the reference phase map with a 2D phase unwrapping technique [6]. The unwrapped phase map (true phase) provides phase differences consistent with the SCIP measurement process. Applying the 2D phase unwrapping technique to the reference phase map unwraps the  $2\pi$  ridge discontinuities resulting from both the phase wraps and the branch cuts. The aperture averaged mean squared phase error determined from the true phase will be too low since the deformations in the 2D measurement plane phase map due to the presence of the  $2\pi$  discontinuities associated with branch cuts has

been removed in the unwrapped phase. This means that the simulated aperture averaged mean squared error will not equal the theoretical aperture averaged mean squared phase error. However, the theoretical performance of the minimum variance wavefront reconstructor can be compared to the theoretical performance of the new least squares reconstructor. The simulated aperture averaged mean squared phase error of the minimum variance wavefront reconstructor can be compared with both the new and conventional least squares reconstructors for both the reference and true phase maps. Section 4.1 demonstrates the performance of the reconstructor for highly polished objects. These objects provide the best reconstructions since spatial phase information is not randomized upon reflection.

Section 4.2 shows results for a simple rough object which can be modeled by a random double point source. This type of object is useful in determining the resolution of the optical system.

Section 4.3 provides results for random extended objects for optimal reconstruction conditions. Optimal conditions refer to no measurement noise and no differences between the theoretical and simulated object model. A comparison to the least squares class of reconstructors is also accomplished in this section. Several types of comparisons are made between the least squares and minimum variance methods. The theoretical aperture averaged mean squared phase error is determined for the minimum variance and new least squares reconstructor discussed in Section 3.4. A comparison of the simulated aperture averaged mean squared phase error between the minimum variance and new least squares methods is made for the two types of phase difference inputs to the wavefront reconstructors (reference phases and true phases). A comparison of the simulated aperture averaged mean squared phase error is made between the minimum variance reconstructor and a conventional least squares reconstructor for both the reference and true measurement plane phase maps. In comparing the performance of the minimum variance reconstructor to a conventional least squares reconstructor, the G & R version of the conventional least

squares reconstructor discussed in Section 2.2 was used. The G & R conventional least squares reconstructor minimizes the same error metric as that for the minimum variance reconstructor. The simulated aperture averaged mean squared phase error for the minimum variance reconstructor is compared to the G & R reconstructor on identical sampling grids. The G & R wavefront reconstructor is implemented on an  $8 \times 8$  sampling grid to coincide with the  $8 \times 8$  sampling grid used in the minimum variance reconstruction process. For the minimum variance wavefront reconstructor, only the values of the squared error at the spatial locations of the sampling grid were used in determining the average mean squared phase error.

Section 4.4 evaluates the performance of the minimum variance reconstructor under sub-optimal conditions. Mismatches between the theoretical object average reflectivity and the simulated average reflectivity are characterized. Three types of average reflectivity mismatches are characterized. The first average reflectivity mismatch between the theory and simulation looks at differences between a Gaussian object average reflectivity with infinite extent (as modeled in the theoretical development of the minimum variance wavefront reconstructor) and a truncated Gaussian (to reflect the finite extent of the object in simulation). The second average reflectivity mismatch between the minimum variance theory and simulation investigates the effect of differences between the shape and magnitude of the average reflectivity profiles. For the second average reflectivity mismatch case, the average reflectivity profile in the theory is assumed to be spatially Gaussian with infinite extent. The third average reflectivity mismatch investigates differences between the theoretical object size and the simulated object size. The aperture averaged mean squared phase error is determined as a function of the degree of size mismatch. Also included in this section are the effects of additive white Gaussian phase difference measurement noise on the performance of the minimum variance wavefront reconstructor.

In carrying out the computer simulations, the following parameters were used. The measurement plane aperture was a square with a side length of 3 m. There

were two sampling grids used in the measurement plane, a fine grid and a coarse grid. The fine sampling grid is shown in Figure 2. The number of sample points on the fine grid in both linear directions are referred to as  $N_x$  and  $N_y$  and there were  $33 \times 33$  evenly spaced points within the measurement plane. The sample spacing  $L_x$  and  $L_y$  of the fine grid was 0.09375 m in both linear directions. The fine grid was used to determine the high resolution phase maps with which to compare the reconstructed phase maps. Figure 2 can also be used for the coarse grid by substituting  $N = N_x = N_y$  and  $L = L_x = L_y$ . For the coarse grid, the number of measurement plane samples,  $N$ , in the reconstruction process was 8 in both linear directions. This lead to a coarse sampling grid of  $8 \times 8$  evenly spaced samples in the measurement plane aperture. The sample spacings,  $L$ , on the coarse grid was 0.375 m in both the  $x$  and  $y$  directions. The reconstructed phase maps were generated on the points of the coarse grid. The elementary functions in equation (31) were used to interpolate the remaining reconstructed phase estimates on the 33 by 33 fine grid. The interpolation allowed for a direct comparison between the high resolution phase maps and the reconstructed phase maps. The illumination center wavelength was  $\lambda = 1.3 \mu\text{m}$  and the measurement plane to object plane distance was  $10^6$  m. The shear between the measurement plane fields ( $s_x$  and  $s_y$ ) were both 0.46875 m. The distance from the illumination plane to the object plane was assumed to be  $10^6$  m and so the separation of the illuminating beams was also assumed to be 0.46875 m. The radius of the elementary functions,  $R$  was set to 0.75 L. This choice of radius was found to provide smooth reconstructions. Sample spacing in the object plane was 0.21667 m in both linear directions. The object dimensions were allowed to vary. These parameters were used in all of the results discussed in this chapter. The following section presents the results for reconstructions of objects which are smooth on the scale of an optical wavelength.



#### 4.1 *Reconstructions of Smooth Objects*

Before evaluating the performance of the minimum variance wavefront reconstructor for conditions when the object is optically rough (diffuse scatterer), a performance assessment was made for objects which are smooth on the scale of an optical wavelength (highly polished objects). The reconstructor performance is expected to be better than the diffuse scattering case when the object surface features can be considered optically smooth. This stems from the preservation of the spatial phase information in the polished objects reflected field. In random objects, the reflected phase is randomized, leading to a corrupted reflected phase map. The reflected field from a highly polished object can essentially be considered a special case of the diffuse scattering problem. Namely, the reflected field from a polished object can be considered a noise free reflection where the noise is the randomization of the field itself. By assuming negligible amplitude effects (low absorbing material), the randomization effects result predominantly from the phase. The reflected phase from a highly polished object can be considered as the reflection of a random scatterer where the amount of corruption of the scattered phase map is considered negligible. Two types of objects are evaluated in this section. The first is an object with a 2D spatial irradiance distribution similar to a doughnut. The second object has three bars parallel to the horizontal axis in the object plane. For both objects, the reconstruction matrix,  $M_{jn}$ , corresponding to the Gaussian average reflectivity profile given by equation (54) was used.

The first polished object under consideration had a simulated Gaussian average reflectivity profile given by equation (54) with the additional condition that a central circular core with a smaller radius than that of the object support is set to zero. A top down 2D view of the average reflectivity in the object plane is shown in Figure 10. The average reflectivity distribution from the object resembles a doughnut with an inner radial average reflectivity that is higher than along the outer object support.

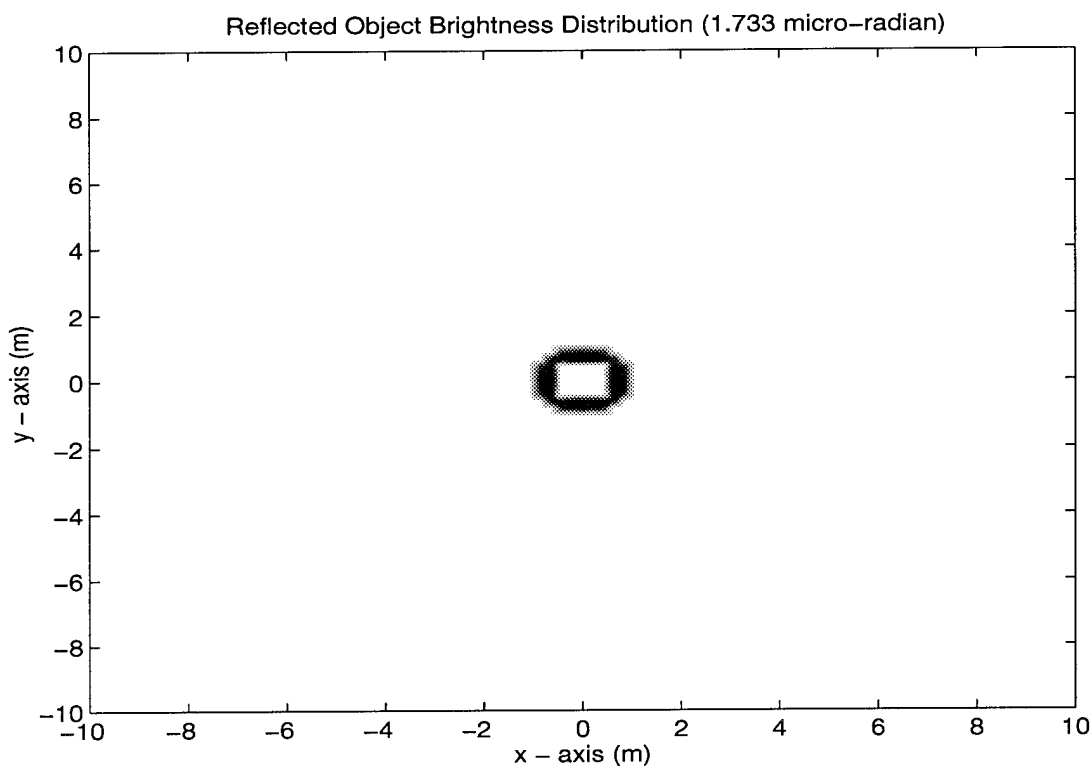


Figure 10. Average reflectivity distribution for 1.7333  $\mu\text{rad}$  deterministic doughnut object.

The reflected field from a highly polished object can be modeled as being entirely real. This can be seen from the following illustration. The electromagnetic waves illuminating the object are plane waves. Since in the minimum variance formalism the average value of the phase is negligible, the mean value of the illuminating wavefront phase can be set to zero. The reflected wavefront preserves the phase information of the illuminating wavefront for highly polished objects and so the reflected field is entirely real. Spatial features were added to the object by zeroing selected portions of the reflected field.

The reflected field was Fourier transformed and the phase was determined from the real and imaginary parts of the measurement plane field. The resulting measurement plane computer simulated phase map had phase differences in the range  $\pm\pi$  requiring no phase unwrapping.

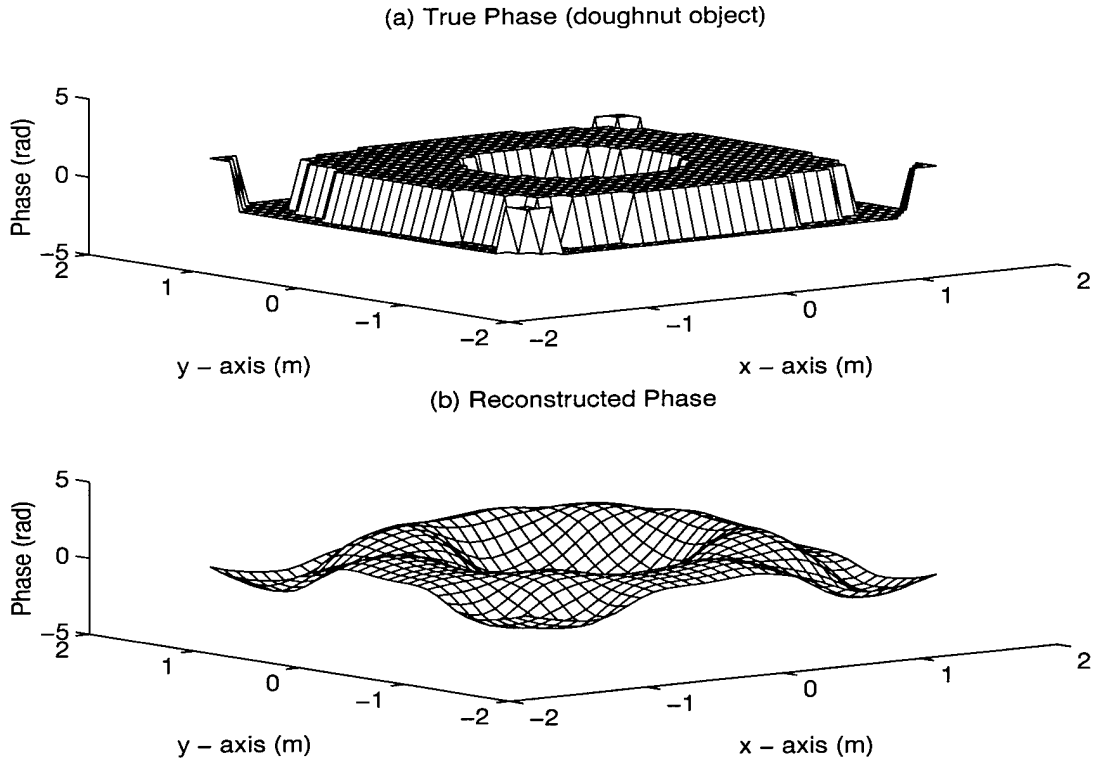


Figure 11. Measurement plane phase maps of (a) true phase and (b) reconstructed phase for  $1.733 \mu\text{rad}$  deterministic doughnut object.

Figure 11 shows the measurement plane true phase (a) and reconstructed phase (b) corresponding to one frame from the doughnut object. The reconstructed phase was obtained by using the phase differences from the true phase as inputs to the minimum variance wavefront reconstructor. The phase differences correspond to those obtained by the SCIP technique given in equation (10). The simulated aperture averaged squared phase error was determined by pointwise subtracting the estimated phase from the true phase, pointwise squaring the result, integrating across the measurement plane aperture, and normalizing by dividing by the aperture area. The simulated aperture averaged squared phase error determined in this fashion was 1.2763 radians squared. The simulated aperture averaged squared phase error was 41 % of the aperture averaged input phase variance given by the last term in equa-

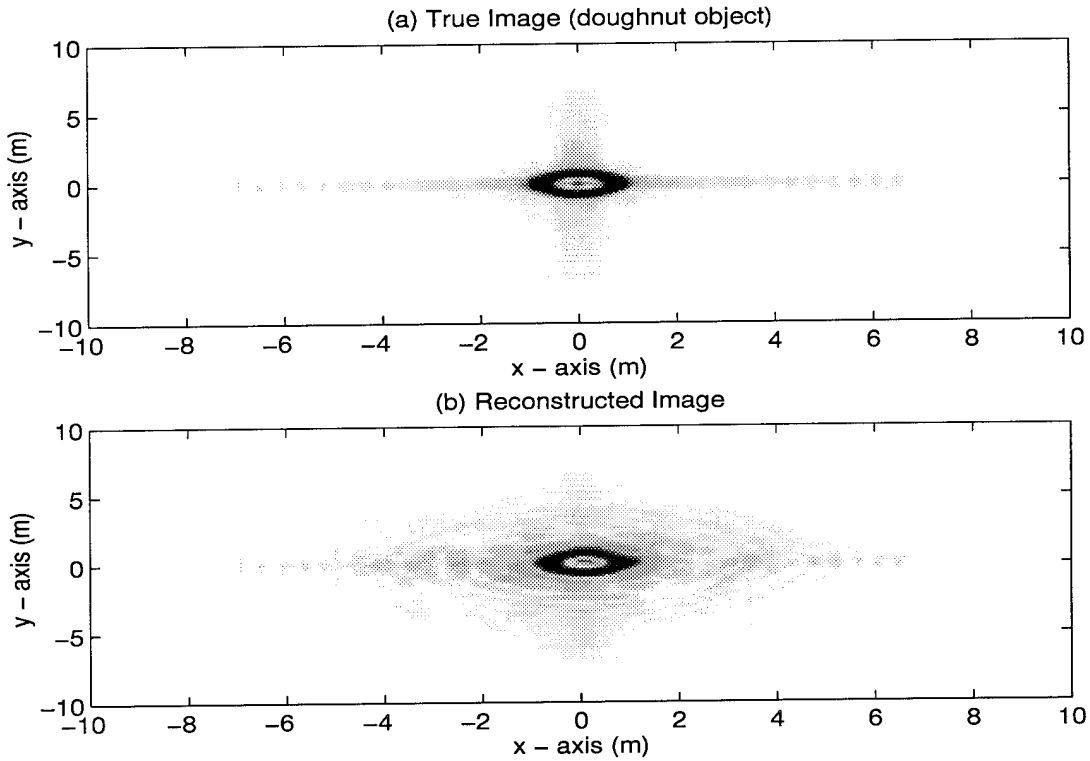


Figure 12. Plots of (a) true image and (b) reconstructed image for  $1.733 \mu\text{rad}$  deterministic doughnut object.

tion (40). The measurement plane sampling was 8 by 8 samples across a 3 m square aperture.

The instantaneous true image which would be obtained from a 3 by 3 m square filled aperture was obtained by Fourier transforming the measurement plane field. The measurement plane true field was determined using the true phase shown in Figure 11 along with the true field amplitudes. The measurement plane reconstructed field was estimated using the reconstructed phases shown in Figure 11 and the true field amplitudes. Figure 12 shows the resulting image for the true image (a) and reconstructed image (b). Only one realization (frame) of measurement plane phase data was used to reconstruct the images since this was a deterministic test case. The central hole in the reconstructed doughnut object is clearly visible. The true and reconstructed images look similar.

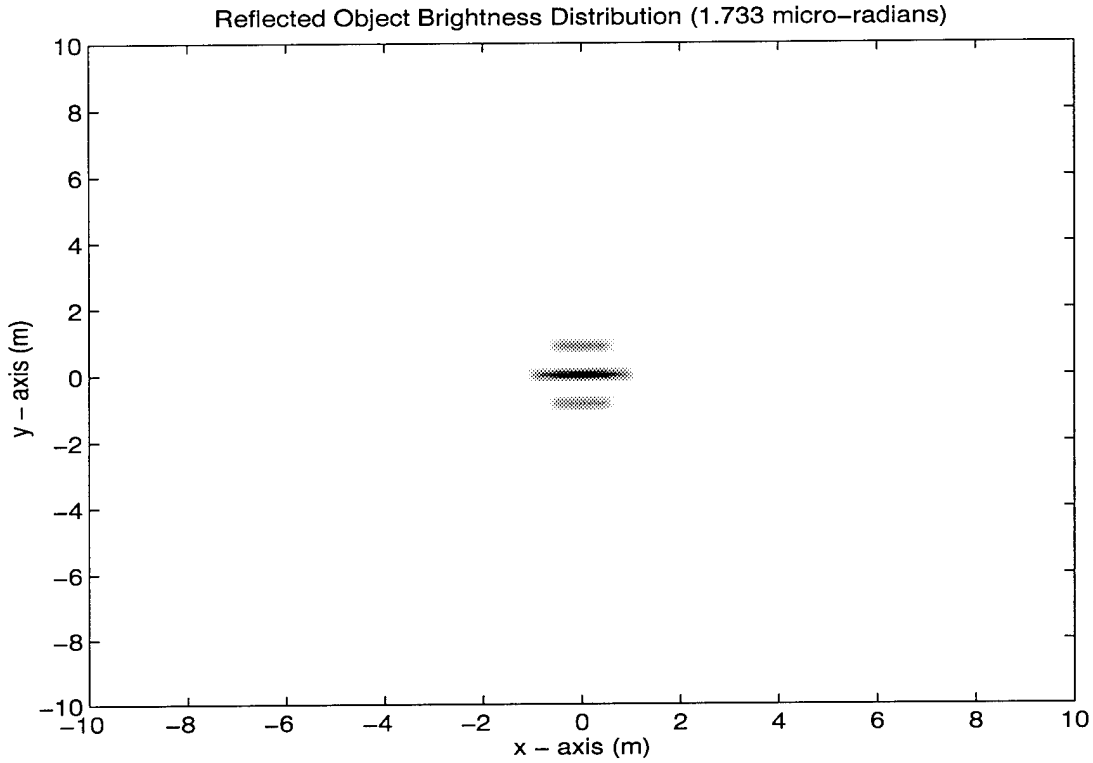


Figure 13. Average reflectivity for 1.733  $\mu\text{rad}$  deterministic tri-bar object.

In Figure 13, a simulated object average reflectivity with three horizontal stripes is illustrated. The object has a reflected Gaussian average reflectivity distribution given by equation (54). In addition to this average reflectivity profile two parallel stripes are set to zero equally spaced from the horizontal axis in the object plane.

The reconstruction process used for the doughnut object was repeated for the tri-bar object. The measurement plane phase maps are illustrated in Figure 14. Figure 14 (a) shows the true phase in the measurement plane and (b) shows the reconstructed phase. Identical sampling was used as with the doughnut object. The aperture averaged squared phase error was 0.8326 radians squared true and reconstructed phases corresponding to the tri-bar object. This aperture averaged squared phase error was 27 % of the aperture averaged input phase variance.

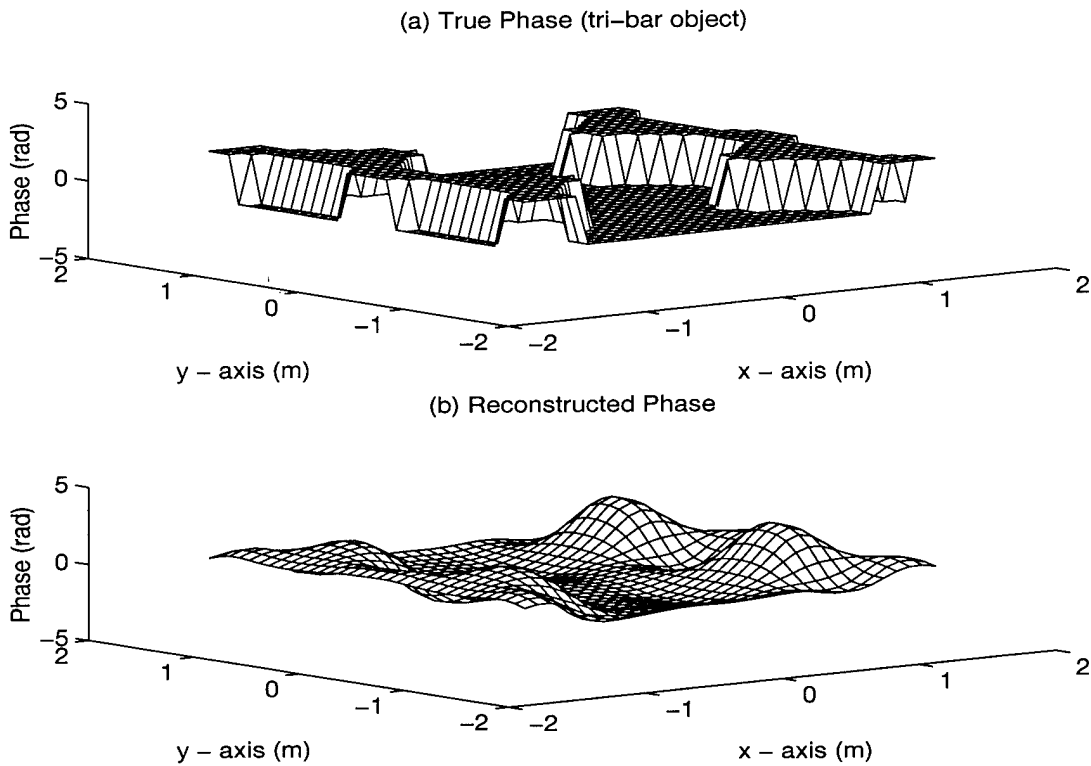


Figure 14. Measurement plane phase maps of (a) true phase and (b) reconstructed phase for  $1.733 \mu\text{rad}$  deterministic tri-bar object.

Figure 15 shows the true (a) and reconstructed (b) images corresponding to the single frame phase maps depicted in Figure 14. Good agreement is again seen between the actual reflected object average reflectivity, the true image, and the reconstructed image. An important point to mention is that in constructing the true image, the entire 3 m by 3 m aperture (33 by 33 points) was used to determine the resulting image. For the minimum variance wavefront reconstructor, the reconstructed image only used 8 by 8 sample points in the reconstruction process.

This section has demonstrated that the minimum variance reconstructor works for the special case of an optically smooth object. Images of an object with an average reflectivity profile that looks like a doughnut and a horizontal tri-bar were successfully reconstructed. The next section looks at the performance of the minimum variance reconstructor for a simple diffuse scatterer.

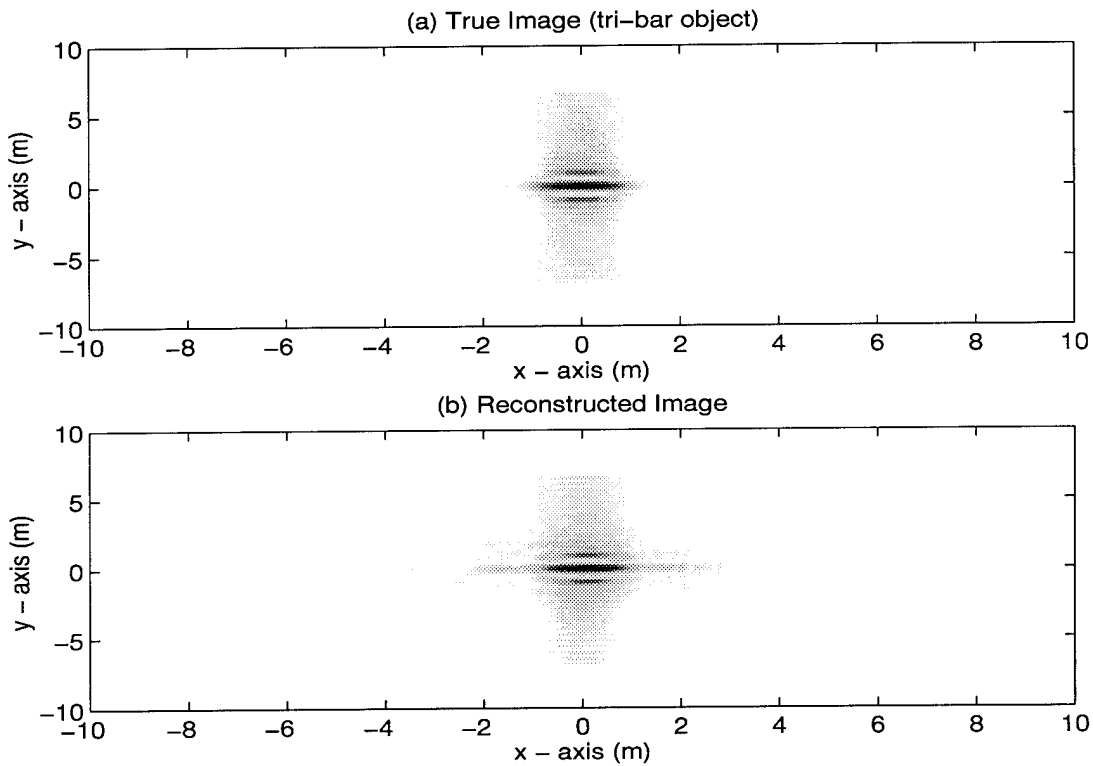


Figure 15. Image plane maps of (a) true image and (b) reconstructed image for  $1.733 \mu\text{rad}$  deterministic tri-bar object.

#### 4.2 Simple Diffuse Reflector

This section demonstrates the performance of the minimum variance reconstructor for a geometrically simple diffuse scattering object. A double point source is used to illustrate the resolution of the minimum variance reconstructor. The term point source denotes an object with physical dimensions much smaller than the resolution of the optical system. Computationally, a point source corresponds to objects with physical dimensions smaller than the sample spacing in the object plane. Figure 16 shows the configuration of the point sources in the object plane. The optical power at each point source was the same. The field at each source point was represented by a complex number whose real and imaginary parts were independent Gaussian variables with zero mean and equal variance. For consistency

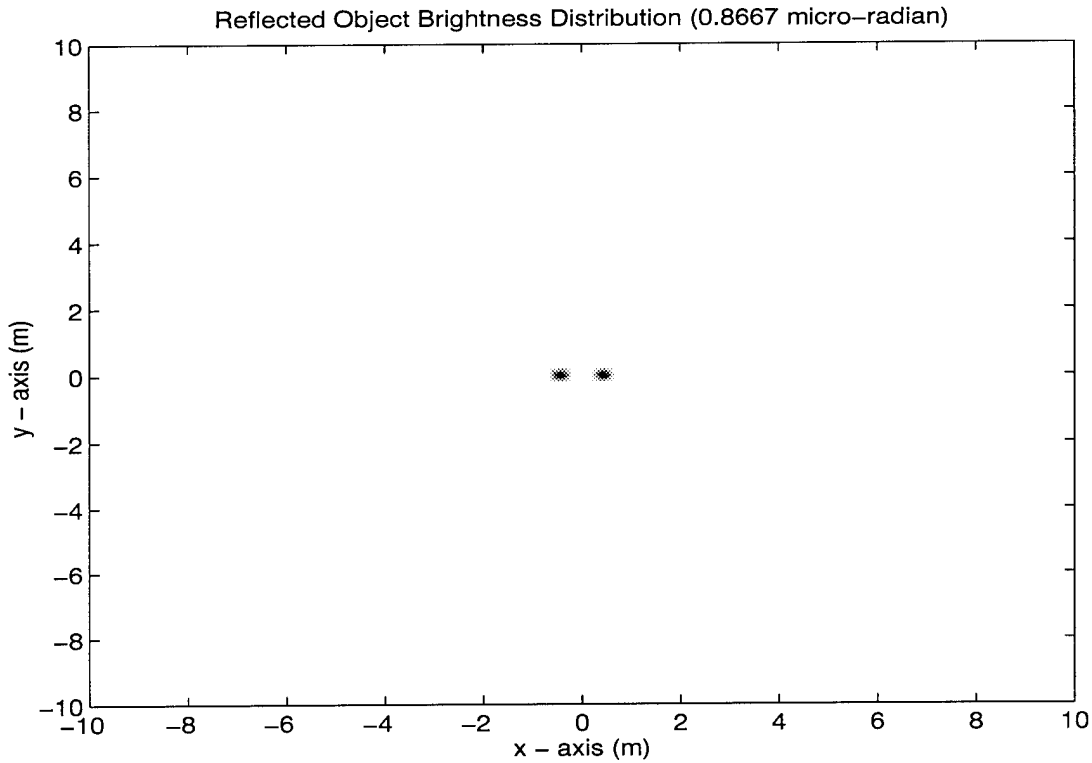


Figure 16. Average reflectivity distribution for a random double point source object with  $0.8667 \mu\text{rad}$  separation.

with circularly complex Gaussian statistics, the variance was set to half the average reflectivity at a given source point [13].

As before, the measurement plane reference phase is obtained by Fourier transforming the reflected object field. The reference phase is then determined by calculating the phase according to equation (20) at each measurement plane spatial location. The true phase is determined by unwrapping the reference phase with a 2D phase unwrapping utility [6]. Figure 17 shows the measurement plane (a) true phase and (b) the reconstructed phase corresponding to the random double point source object depicted in Figure 16. The reconstructed phase appears to be a smoothed version of the true phase.

The instantaneous image was obtained by Fourier transforming the measurement plane field and pointwise multiplying by the complex conjugate of the resulting



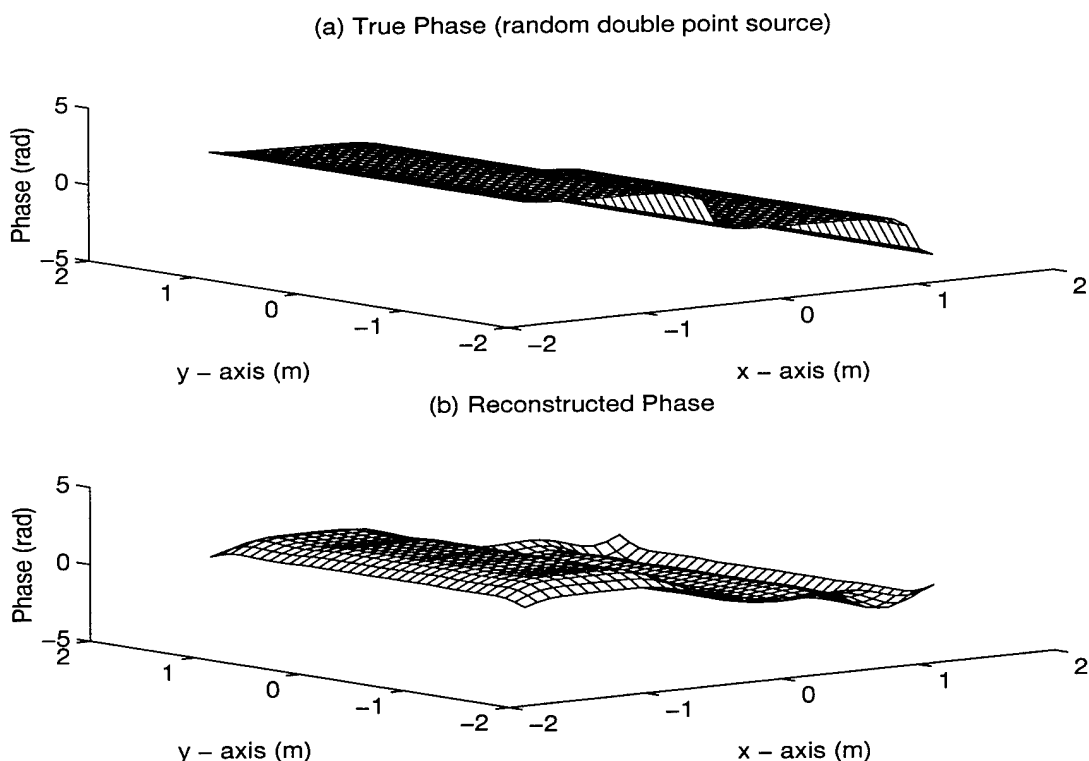


Figure 17. Measurement plane phase maps of (a) true phase and (b) reconstructed phase for  $0.8667 \mu\text{rad}$  separation random double point source object.

image field. Figure 18 shows the resulting (a) true and (b) reconstructed images for the single frame phases illustrated in Figure 17. The reconstructed image exhibits the general features of the true image of the random double point source. The reconstructed phase and image matched the true phase and image particularly well for this random draw from the space of possible phase and image realizations.

The average image irradiance was formed by pointwise averaging the instantaneous image irradiance. Figure 19 shows the (a) true and (b) reconstructed images for 100 independent image frame averages of the random double point source object. The reconstructed image shows the separation between the two point sources. This separation is equal to the diffraction limited resolution of the imaging system. The measurement plane sampling was 8 samples in a given linear direction (64 total

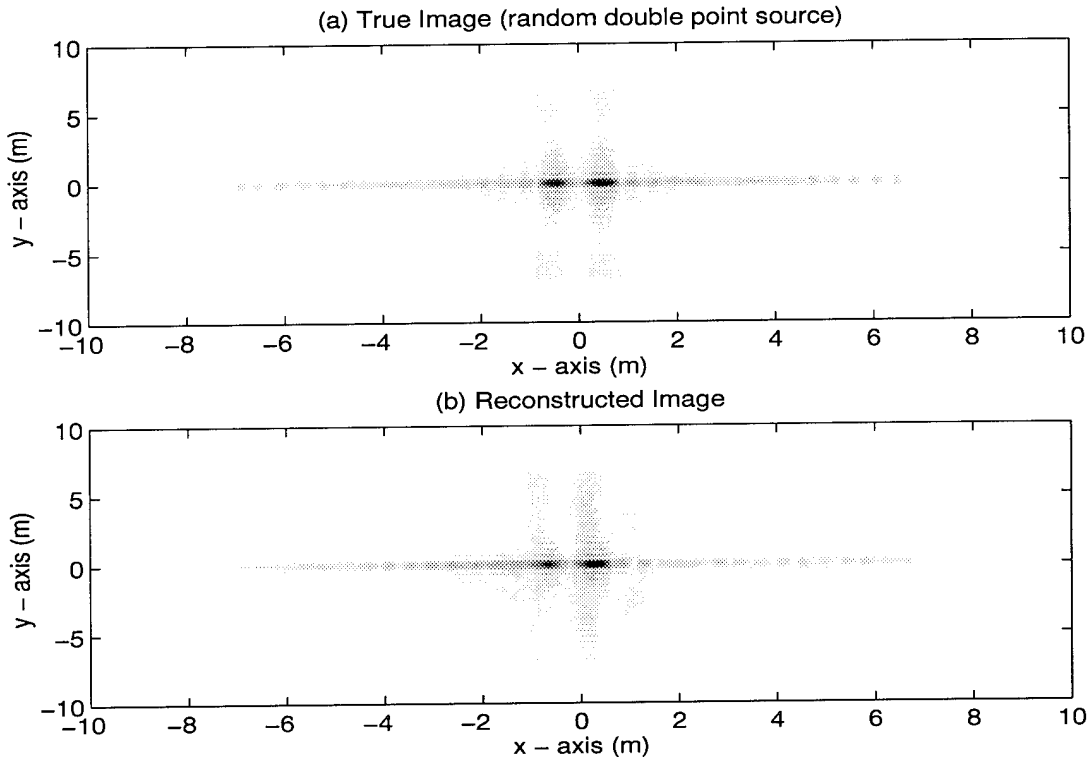


Figure 18. (a) True image and (b) reconstructed image for random double point source object with  $0.8667 \mu\text{rad}$  separation. The measurement plane sampling density was 8 by 8 evenly spaced samples in a 3 m by 3 m square collecting aperture. The number of independent image frames used to average was 1.

samples spanning a 3 m by 3 m aperture). The measurement plane sample spacing was 0.375 m in both the  $x$  and  $y$  directions.

To better see the diffraction limited performance shown in Figure 19, an overlay of a slice along the  $x$  axis of the true and reconstructed images is helpful. Figure 20 shows that the peak-to-peak separation of both the reconstructed image and the true image is identical. The peak-to-peak separation was calculated as 0.85 m. The full width at half maximum (FWHM) measurement of a single lobe of the true image irradiance was 0.42 m. The FWHM measurement of the reconstructed image was 0.62 m.

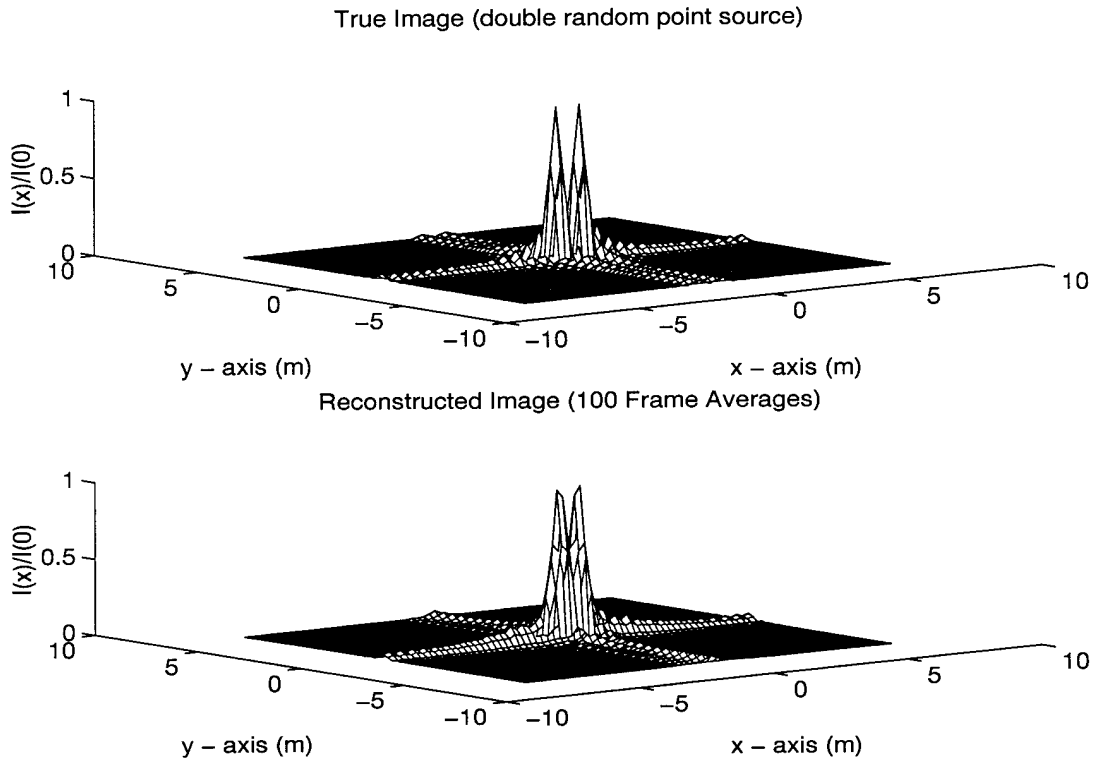


Figure 19. (a) True image and (b) reconstructed image for random double point source object with  $0.8667 \mu\text{rad}$  separation. The measurement plane sampling density was 8 by 8 evenly spaced samples in a 3 m by 3 m square collecting aperture. The number of independent image frames used to average were 100.

The random double point source object was used to bridge the gap between the specular reflector class of objects and the extended diffuse reflector class discussed in the next section. Additionally, the random double point source object was useful in illustrating the diffraction limited resolution of the minimum variance reconstructor. The next section evaluates the performance of the minimum variance reconstructor for extended diffuse reflectors.

#### 4.3 *Extended Diffuse Reflectors*

This section illustrates the performance of the minimum variance wavefront reconstructor when imaging optically rough extended objects. The theory developed

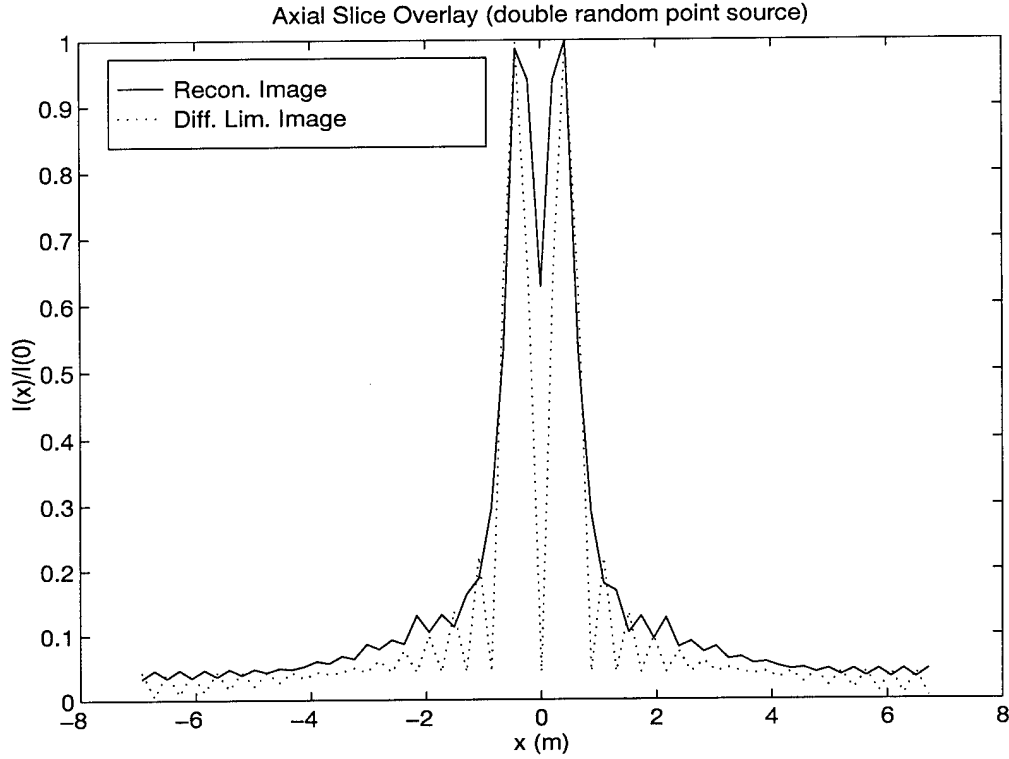


Figure 20. Overlay of true image slice and reconstructed image slice for random double point source object with  $0.8667 \mu\text{rad}$  separation. The number of independent image frames used to average were 100.

in Chapter III was applied to a simulated object with a Gaussian average reflectivity profile described by equation (54). The reflected field in the immediate vicinity of the object was modeled by circularly complex Gaussian statistics where the real and imaginary parts of the field are zero mean Gaussian random variates with equal variances [9]. To generate the proper far field statistics, the variance was set to half the value of the average reflectivity at each point in the object [10]. The average reflectivity at any given point within the support of the object was given by equation (54). The average reflectivity was set to zero outside the object support.

The aperture plane of the imaging system was located in the far field of the object. Discrete sampling detectors were simulated by a sampling grid illustrated in Figure 2. The quantities  $L_x$  and  $L_y$  are the fine grid sample spacings in the  $x$  and  $y$  directions. The parameters  $N_x$  and  $N_y$  represent the number of sampling

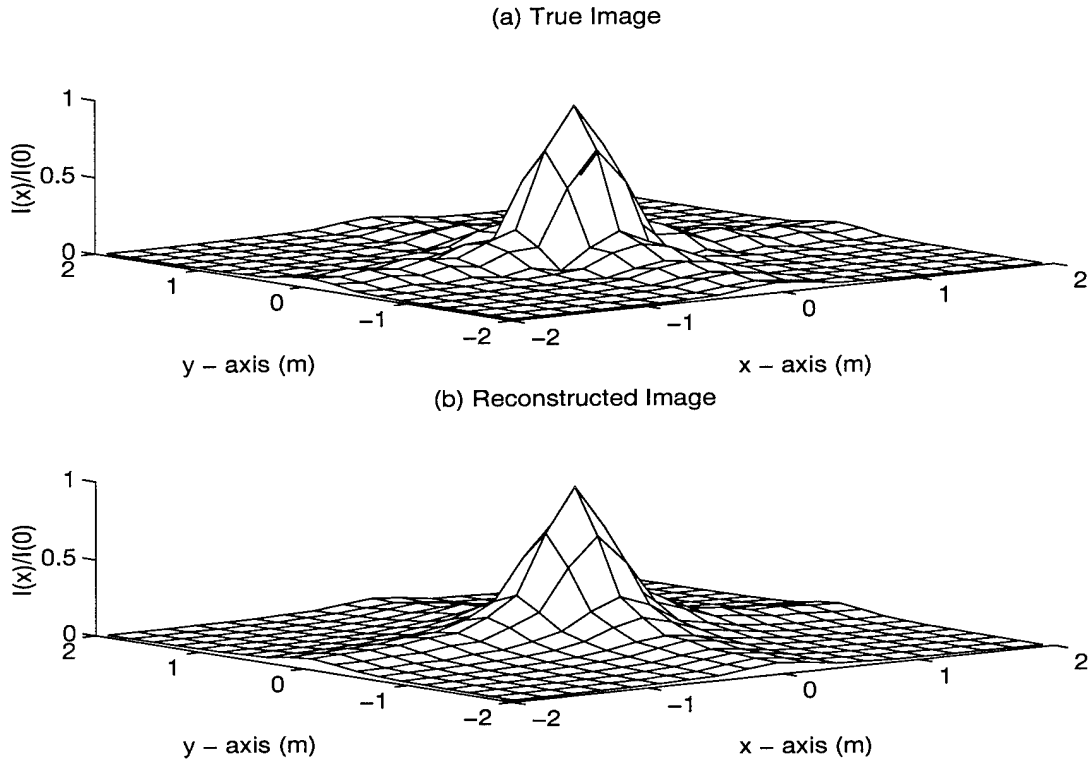


Figure 21. True (a) and reconstructed image (b) for extended random object with Gaussian average reflectivity profile

elements in the  $x$  or  $y$  directions so that the total spatial extent of the sample array is  $(N_x - 1)L_x$  by  $(N_y - 1)L_y$ .

The optimum reconstruction matrix using the minimum variance formalism was calculated for a Gaussian target subtending  $0.4333 \mu\text{rad}$ . The angular subtense of  $0.4333 \mu\text{rad}$  indicates the  $e^{-1}$  width of the Gaussian average reflectivity profile given in equation (54). Figure 21 shows a comparison of the true image with that of the average reconstructed image. The measurement plane field was obtained by Fourier transforming the reflected object field.

The true image was formed by Fourier transforming the measurement plane field, computing the associated image irradiance, and averaging the result. One hundred realizations of the random object were used to obtain the results presented. As can be seen, good agreement between the reconstructed and true image is evident.

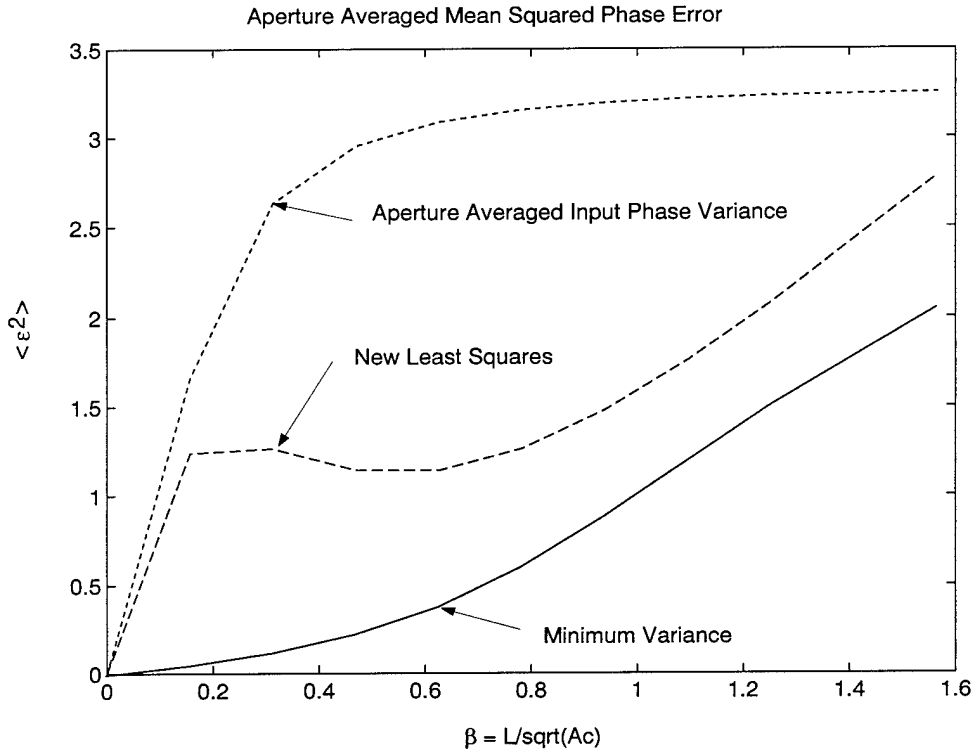


Figure 22. Minimum theoretical aperture averaged mean squared phase error for minimum variance (solid line) and least squares (long dashes) formalisms. Also included is the aperture averaged input phase variance (short dashes). Gaussian average reflectivity profiles with infinite spatial extent were used in determining the theoretical aperture averaged mean squared phase error for all values of  $\beta$ .

The aperture averaged mean squared phase error given by equation (40) for this case was 0.0522 radians squared. The aperture averaged mean squared phase error was 3.1 % of the aperture averaged input phase variance.

Figure 22 shows a comparison of  $\langle \epsilon^2 \rangle$  from equation (40) for the least squares wavefront reconstructor from Section 3.4 and the minimum variance wavefront reconstructor as a function of the sampling parameter,  $\beta = \frac{L}{\sqrt{A_c}}$ . The sampling parameter is a function of measurement plane sample spacing,  $L$ , and the coherence area of the object,  $A_c$ . Note that the dimensionless parameter  $\beta$  does not factor out of the analysis of this phase reconstruction technique. Rather, the choice of  $\beta$  as the parameter used to study sampling effects on the reconstruction reflects the physical

insight that errors due to sampling are closely related to the coherence area of the field in the measurement plane. The dependency of  $\beta$  on the object coherence area makes the sampling parameter object dependent. The general expression for the coherence area,  $A_c$ , is given by [13: page 210],

$$A_c = \int_{-\infty}^{\infty} \int_{-\infty}^{\infty} |\mu_o(\Delta x, \Delta y)| d\Delta x d\Delta y, \quad (55)$$

where  $\mu_o(\Delta x, \Delta y)$  is the complex coherence factor. By substituting the complex coherence factor corresponding to the Gaussian object average reflectivity profile given by equation (43), the coherence area determined from equation (55) is seen to be,

$$A_c = \left(\frac{1}{2}\right) \frac{(\bar{\lambda} z)^2}{R_x R_y}, \quad (56)$$

where  $\bar{\lambda}$  is the center wavelength of the illuminator, and  $z$  is the object to receiver plane distance. The parameters  $R_x$  and  $R_y$  can be related to the object dimensions,  $D_x$  and  $D_y$ , by,

$$\begin{aligned} R_x &= \sqrt{\pi} \frac{D_x}{2} \\ R_y &= \sqrt{\pi} \frac{D_y}{2}. \end{aligned} \quad (57)$$

The dimensions of the object were changed to vary the coherence area in the measurement plane. An 8 by 8 measurement plane sampling grid was used and kept constant for all measurements. The theoretical object average reflectivity used to estimate the optimal reconstruction matrix,  $M_{jn}$ , was a Gaussian with infinite spatial extent. The  $e^{-1}$  width of the theoretical object average reflectivity was set to 0.4333 m, 0.8667 m, 1.3000 m, 1.7333 m and 2.1667 m for the corresponding values of  $\beta$ . As can be seen in Figure 22 the minimum expected error for the minimum variance formalism is much less than that expected for the least squares methods. The bump in the theoretical least squares curve (long dashes) in Figure 22 is suspicious. One

possible reason for the bump in the theoretical least squares results is precision limitations in the determination of the measurement plane phase covariances. These precision errors become more significant as  $\beta$  becomes smaller. As can be seen by equation (44), the minimum variance wavefront reconstructor compensates for some of the  $\Phi_{nm}$  precision error by including  $\Phi_{nm}^{-1}$  in the estimation of the optimal reconstruction matrix,  $M_{jn}$ . The current precision level in the determination of the measurement plane phase covariances was set at the fourth decimal place based on processing time limitations.

Note that, as the value of  $\beta$  becomes smaller, the phase difference correlation matrix,  $\Phi_{nm}$ , becomes ill-conditioned, and hence the inverse of  $\Phi_{nm}$  can become unstable. This results from the orthogonal phase differences converging towards constant values as the object size gets smaller. In the limit of a point source, the  $x$  phase differences in the measurement plane are constant and the  $y$  phase differences are also constant. In this limiting case, the  $\Phi_{nm}$  matrix is not invertible. For the  $0.4333 \mu\text{rad}$  object, the condition number of the  $\Phi_{nm}$  matrix was high ( $1.577 \times 10^3$ ).

Computer simulation was used to determine the simulated  $\langle \epsilon^2 \rangle$  as a function of  $\beta$ . Both the reference phase map and the true phase map were used in the simulations. The reference phase map was used to illustrate the performance of the minimum variance wavefront reconstructor when the measurement plane phase map contained ridge discontinuities of magnitude  $2\pi$  resulting from branch cuts and phase wraps. These ridge discontinuities are present in the actual measurement plane phase function and the associated phase differences are unwrapped by the SCIP detection process. The reference field characterization is used to demonstrate the performance of the minimum variance wavefront reconstructor assuming that phase differences spanning the range of  $-2\pi \leq \Delta\phi_q(\vec{x}) \leq 2\pi$  are available in the detection process. The true phase map was used to demonstrate the performance of the minimum variance wavefront reconstructor for phase difference measurements corresponding to the SCIP detection process. Unlike the branch cuts, which result from zeros in the



measurement plane field, the phase wraps result from the complex exponential representation of the measurement plane 2D phase function and should be unwrapped prior to calculating the aperture averaged mean squared phase error. The aperture averaged mean squared phase error determined from the reference phase will be too high because of the presence of the phase wraps in the 2D measurement plane phase function. However, applying a 2D phase unwrapping technique to the reference phase unwraps the  $2\pi$  discontinuities from both the phase wraps and the branch cuts. The simulated aperture averaged mean squared phase error calculated from the true phase will be too low since the  $2\pi$  phase discontinuities associated with branch cuts have been unwrapped in the true phase map. The theoretical object average reflectivity used to determine  $M_{jn}$  was a Gaussian with infinite extent. The simulated object average reflectivity was matched to the theoretical object average reflectivity.

In the first determination of  $\langle \epsilon^2 \rangle$  as a function of  $\beta$ , the phase differences used as inputs in the simulation were calculated from the reference phase map. The reference and reconstructed phase maps were pointwise subtracted from one another and squared. This process resulted in an array of 33 by 33 squared instantaneous phase error terms denoted  $\epsilon_{si}^2$ . The simulated aperture averaged mean squared phase error,  $\langle \epsilon^2 \rangle_s$ , was obtained by repeating the process for determining  $\epsilon_{si}^2$  for 100 independent measurement plane phase frames, pointwise averaging the squared phase error terms, integrating across the aperture, and normalizing by dividing by the aperture area. Figure 23 shows the comparison between the theoretical and simulated results for the minimum aperture averaged mean squared phase error as a function of the sampling parameter,  $\beta$ .

The simulated aperture averaged mean squared phase error is higher than the theoretical result for the minimum variance reconstructor because precision limitations in the phase covariances and the presence of phase wraps in the simulated reference phases. The phase wraps cause artificial ridge discontinuities in the mea-

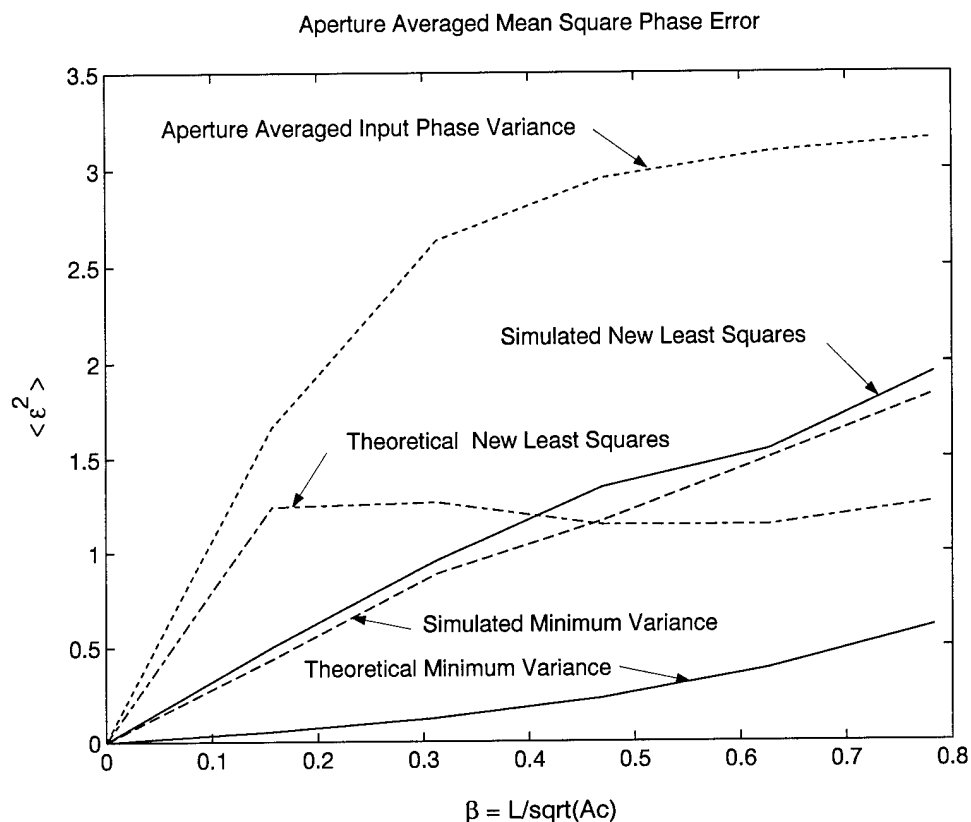


Figure 23. Aperture averaged mean squared phase error for theoretical (lower solid line) and simulated (long dashes) minimum variance results. Aperture averaged mean squared phase error for theoretical (dash dot) and simulated (upper solid line) results for the new least squares reconstructor. The aperture averaged input phase variance is also shown (dotted line). The reference phase map was used to provide the phase differences. Gaussian average reflectivity profiles with infinite spatial extent were used in both the theoretical and simulated determination of the aperture averaged mean squared phase error. The horizontal axis is the sampling parameter,  $\beta$ . The measurement plane sampling density was 8 by 8 evenly spaced samples in a 3 m by 3 m square collecting aperture. For the simulation results, the number of independent measurement plane frames used to determine  $\langle \epsilon^2 \rangle_s$  was 100.

surement plane phase. Unlike branch cuts which result from isolated zeros in the measurement plane field, the phase wraps should be unwrapped prior to calculating the aperture averaged mean squared phase error. The presence of the phase wraps produce discontinuities in the measurement plane phase function which cause the simulated aperture averaged mean squared phase error based on the reference phase map to be higher than the theoretical result.

Figure 24 shows a comparison of the theoretical and simulated aperture averaged mean squared phase error of the minimum variance reconstructor and the least squares reconstructor of Section 3.4. The phase differences were calculated from the true phase map and are consistent with the SCIP measurement process. The true phases are obtained from the reference phases by applying a 2D phase unwrapping technique [6]. The 2D phase unwrapping utility can not distinguish between phase wraps or the  $2\pi$  discontinuities associated with branch cuts and so both the phase wraps and the discontinuities associated with branch cuts are unwrapped. The simulated aperture averaged mean squared phase error is expected to be less than the theoretical aperture averaged mean squared phase error because of the unwrapping of the  $2\pi$  discontinuities associated with the branch cuts in the measurement plane phase function.

The comparison between the minimum variance reconstructor and the least squares wavefront reconstructor of Section 3.4 shows that both the theoretical and simulated aperture averaged mean squared phase errors are less for the minimum variance wavefront reconstructor. The optimal reconstruction matrix,  $M_{jn}$ , for the minimum variance reconstructor is optimized for the error metric given in equation (40). The new least squares reconstruction matrix,  $M_{jn}^{LS}$ , does not incorporate the measurement plane phase covariance in the optimization process. The minimum variance wavefront reconstructor out performs the least squares reconstructor in terms of the aperture averaged mean squared phase error.

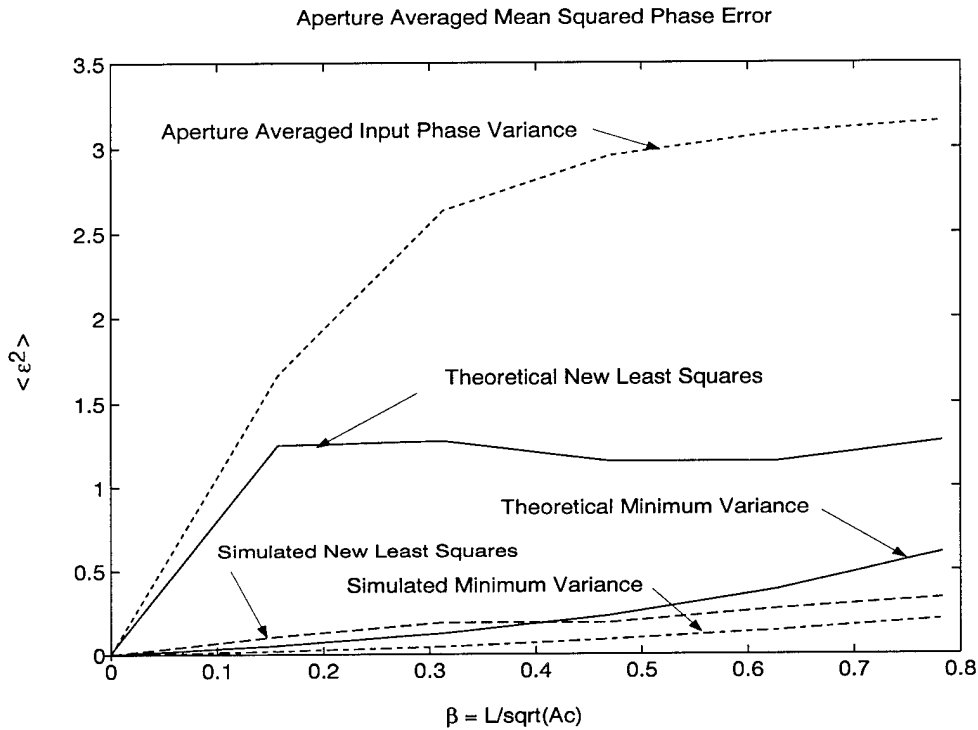


Figure 24. Aperture averaged mean squared phase error for theoretical (solid line) and simulated (dash dot) minimum variance results. Aperture averaged mean square phase error for theoretical (solid with asterisk) and simulated (long dashes) results for the new least squares reconstructor. The aperture averaged input phase variance is also shown (dotted line). The true phase map was used to provide phase differences consistent with the SCIP detection process. Gaussian average reflectivity profiles with infinite spatial extent were used in both the theoretical and simulated determination of the aperture averaged mean squared phase error. The horizontal axis is the sampling parameter,  $\beta$ . The measurement plane sampling density was 8 by 8 evenly spaced samples in a 3 m by 3 m square collecting aperture. For the simulation results, the number of independent measurement plane frames used to determine  $\langle \epsilon^2 \rangle_s$  was 100.

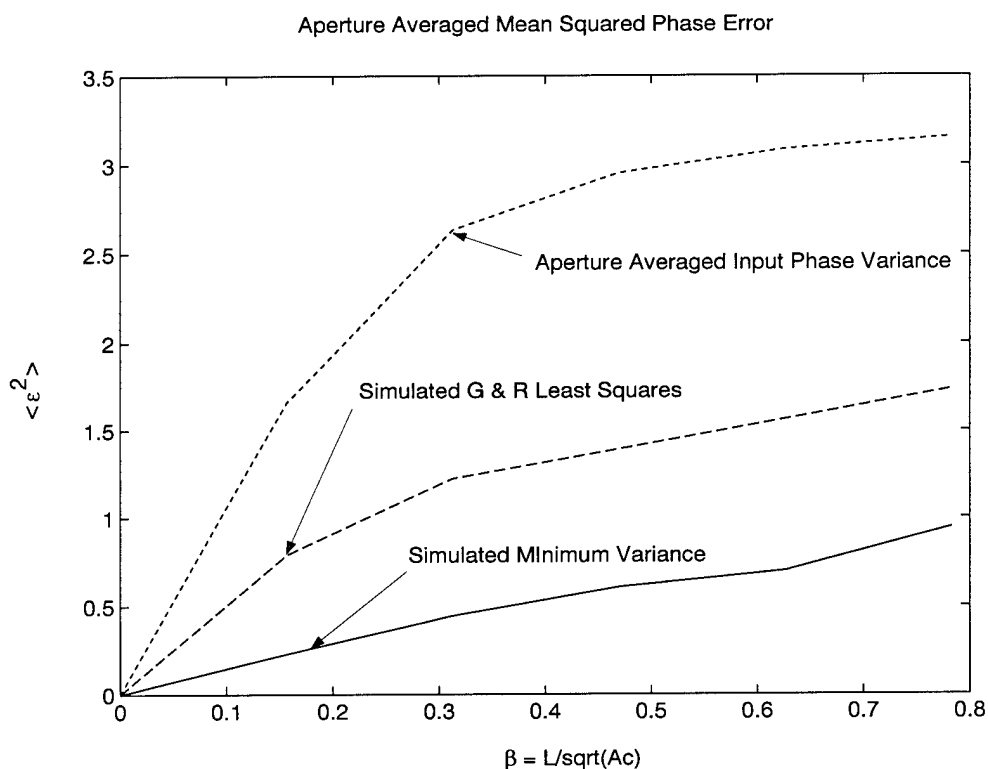


Figure 25. Comparison of simulated aperture averaged mean squared phase error for minimum variance (solid line) and G & R least squares results (long dashes). The aperture averaged input phase variance is also shown (short dashes). The phase differences were determined from the measurement plane reference phases. The horizontal axis is the sampling parameter,  $\beta$ . The measurement plane sampling density was 8 by 8 evenly spaced samples in a 3 m by 3 m square collecting aperture. The number of independent measurement plane frames used to determine  $\langle \epsilon^2 \rangle_s$  were 100. The theoretical average reflectivity profile of the objects used to estimate  $M_{jn}$  were Gaussian with infinite extent. The simulated average reflectivity profile was matched to the theoretical for both the G & R least squares and minimum variance simulations.

The performance of the minimum variance wavefront reconstructor was compared to a conventional least squares reconstructor (G & R least squares reconstructor) as described in Section 2.2. Figure 25 shows a comparison of the simulated aperture averaged mean squared phase error for the minimum variance reconstructor and the G & R least squares reconstructor. The phase differences were calculated from the measurement plane reference phase map and had the range,  $-2\pi \leq \Delta\phi_q(\vec{x}_p) \leq 2\pi$ . The average reflectivity profile of the theory and simulation were both assumed Gaussians with infinite spatial extent. No noise or estimation errors were assumed. The simulated aperture averaged mean squared phase error was determined on the coarse sampling grids for both the minimum variance and G & R least squares reconstruction methods.

The comparison between the minimum variance reconstructor and the G & R least squares wavefront reconstructor of Section 2.2 shows that the simulated aperture averaged mean squared phase error is less for the minimum variance wavefront reconstructor for all values of  $\beta$ . This indicates that the minimum variance reconstructor out performs the G & R least squares reconstructor in terms of the aperture averaged mean squared phase error.

Figure 26 shows a comparison of the simulated aperture averaged mean squared phase error for the minimum variance reconstructor and the G & R least squares reconstructor of Section 2.2. The phase differences were calculated from the true phase map and are consistent with the SCIP measurement process in equation (10). The true phases are obtained from the reference phases by applying a 2D phase unwrapping technique [6]. Both the phase wraps and the  $2\pi$  discontinuities associated with branch cuts are unwrapped.

The comparison between the minimum variance reconstructor and the G & R least squares wavefront reconstructor of Section 2.2 shows that the simulated aperture averaged mean squared phase error, over the values of  $\beta$  shown, is less for

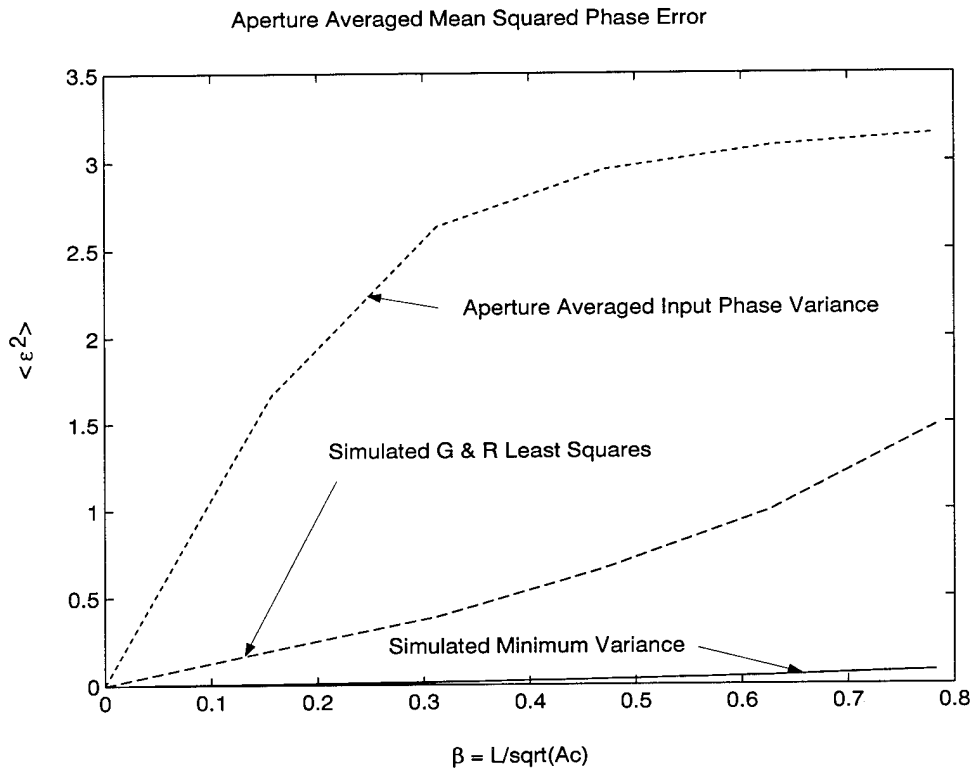


Figure 26. Comparison of simulated aperture averaged mean squared phase error for minimum variance (solid line) and G & R least squares results (long dashes). The aperture averaged input phase variance is also shown (short dashes). Phase differences were determined from the measurement plane true phases. The horizontal axis is the sampling parameter,  $\beta$ . The measurement plane sampling density was 8 by 8 evenly spaced samples in a 3 m by 3 m square collecting aperture. The number of independent measurement plane frames used to determine  $\langle \epsilon^2 \rangle_s$  were 100. The theoretical average reflectivity profile of the object used to estimate  $M_{jn}$  was a Gaussian with infinite extent. The simulated average reflectivity profile was matched to the theoretical for both the G & R least squares and minimum variance simulations.

the minimum variance wavefront reconstructor for both the reference and true phase maps.

In comparing the simulated minimum variance results to the simulated G & R least squares results, the mean squared phase error was determined on the same coarse sampling grid for both the minimum variance and G & R least squares methods. The squared phase error for both the minimum variance and G & R least squares reconstructors was averaged over the measurement plane sampling points.

Theoretical and simulated results should not be expected to match too well. The differences between the theoretical and simulated results are attributable to:

1. The finite (instead of infinite) number of averages used in approximating  $\langle \epsilon^2 \rangle$ .
2. Precision errors in calculating the measurement plane phase covariances. Individual phase covariances are accurate to the fourth decimal place. Processing limitations determined the precision of the phase covariances.
3. The presence of branch cut and phase wrap discontinuities in the simulation. The theory used to develop the phase covariances are based on ensemble statistics and does not predict branch cuts and phase wraps which are single frame effects.

Besides looking at the predicted and simulated aperture averaged mean squared phase errors, the minimum variance wavefront reconstructor was used to reconstruct phases for a variety of object sizes. The reference phases of the measurement plane reference field were determined in accordance with equation (20). The true phases were determined by unwrapping the reference phase with a 2D phase unwrapping technique.

Examples of phase reconstructions are illustrated in Figures 27 through 30 for various values of  $\beta$ . Reconstructed phase maps for objects with angular subtenses of 0.8667, 1.3000, 1.733, and 3.467  $\mu\text{rad}$  are illustrated. These objects correspond to values of  $\beta$  of 0.31, 0.47, 0.63, and 1.25 respectively.



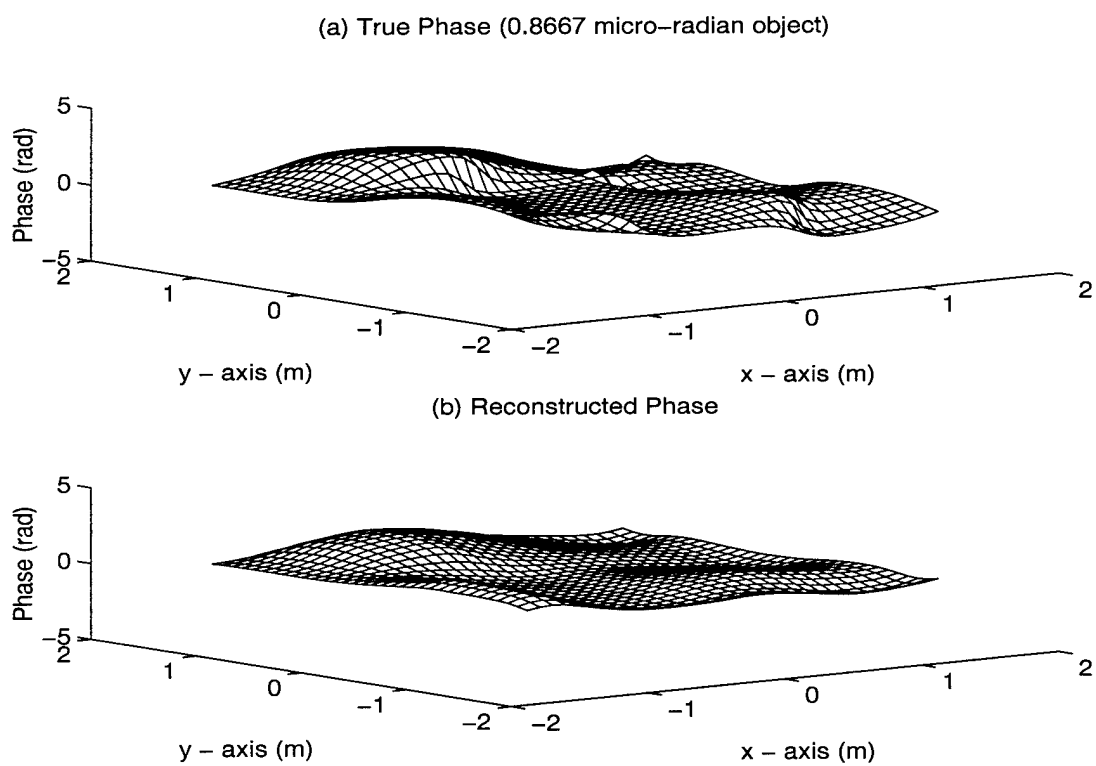
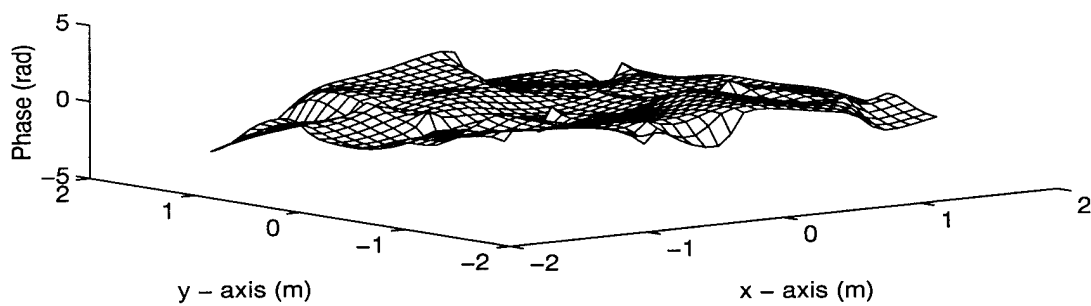


Figure 27. (a) True and (b) reconstructed phase for 0.8667  $\mu\text{rad}$  extended object with Gaussian reflectance.

(a) True Phase (1.3000 micro-radian object)



(b) Reconstructed Phase

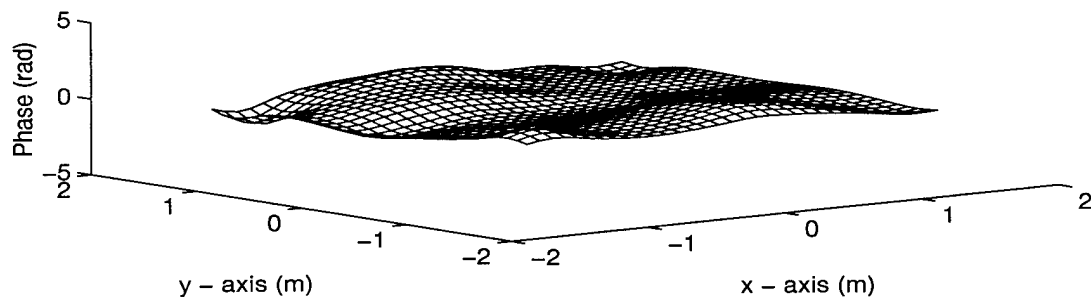
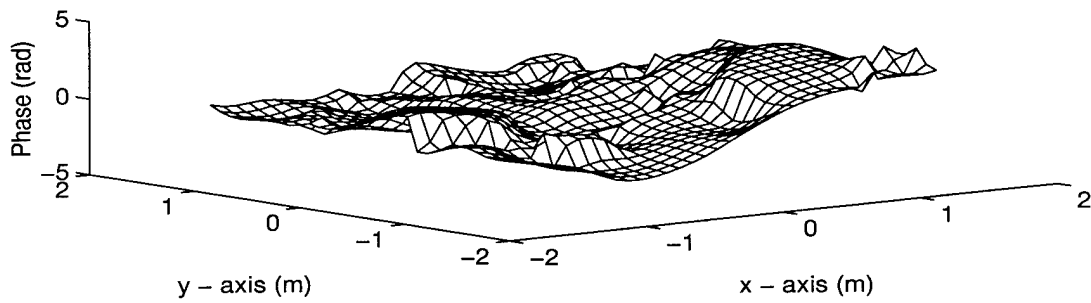


Figure 28. (a) True and (b) reconstructed phase for 1.300  $\mu\text{rad}$  extended object with Gaussian reflectance.

(a) True Phase (1.7333 micro-radian object)



(b) Reconstructed Phase

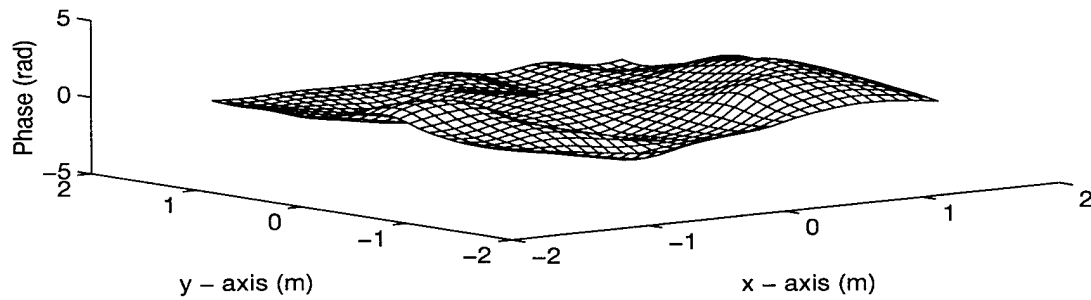
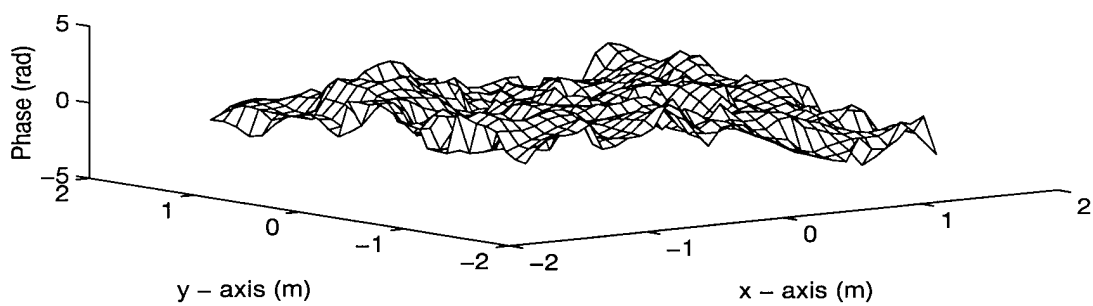


Figure 29. (a) True and (b) reconstructed phase for 1.7333  $\mu\text{rad}$  extended object with Gaussian reflectance.

(a) True Phase (3.467 micro-radian object)



(b) Reconstructed Phase

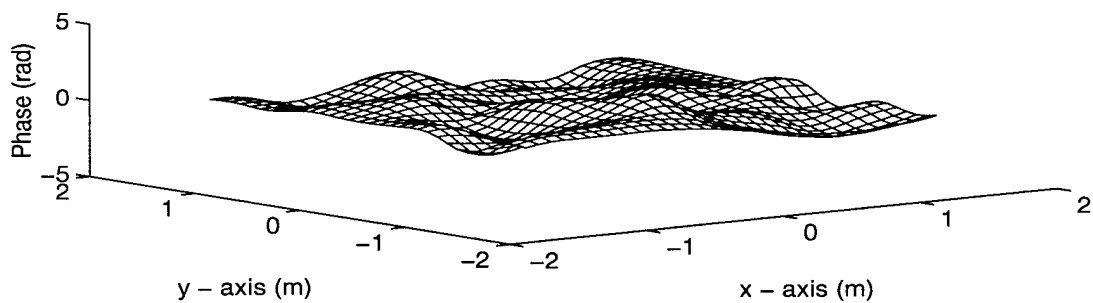


Figure 30. (a) True and (b) reconstructed phase for  $3.467 \mu\text{rad}$  extended object with Gaussian reflectance.

The visual similarity between the true and reconstructed phases decreases as the angular subtense of the object increases. This indicates that the sample spacing,  $L$ , is becoming too large to sufficiently sample the measurement plane field. The visual degradation can be related to  $\langle \epsilon^2 \rangle$  in Figure 22 through the object dependent sampling parameter,  $\beta$ . The aperture averaged squared phase error for phase maps illustrated in Figure 27 through Figure 30 where 0.1033, 0.1343, 0.3770, and 0.4322 respectively. The sampling parameter can also be related to object dimensions through the coherence area relationships in equations (55) through (57). The given sampling is then sufficient for objects smaller than or equal to this determined object size. If imaging larger objects is desired then the measurement plane sampling density must be increased to lower  $\beta$  to an acceptable value.

Figure 31 shows the performance of the minimum variance reconstructor in the presence of a branch cut which result from a zero in the measurement plane field. The branch cut originates in the lower right corner of the upper plot and runs parallel to the  $y$ -axis. The branch cut becomes a  $2\pi$  phase discontinuity. The middle plot shows the unwrapped phase map using a 2D phase unwrapping algorithm [6]. The plot in Figure 32 shows the reconstructed phase map for the same frame of data using the minimum variance formalism. The lower right corner of Figure 32 shows that the phase reconstructor provides continuous phase estimates in the presence of a branch cut.

This section has demonstrated the performance of the minimum variance wavefront reconstructor under ideal conditions (noise free, the same object model in the theory and simulation, and no size or average reflectivity mismatches between the theory and simulation). Phase and image reconstructions were shown for the minimum variance wavefront reconstructor when imaging extended objects with a Gaussian average reflectivity profile in the object plane. The reconstructed instantaneous phases were shown to match the true phases for several different object sizes. For values of  $\beta$  up to 0.47, the reconstructed phases appeared to be reasonable represen-

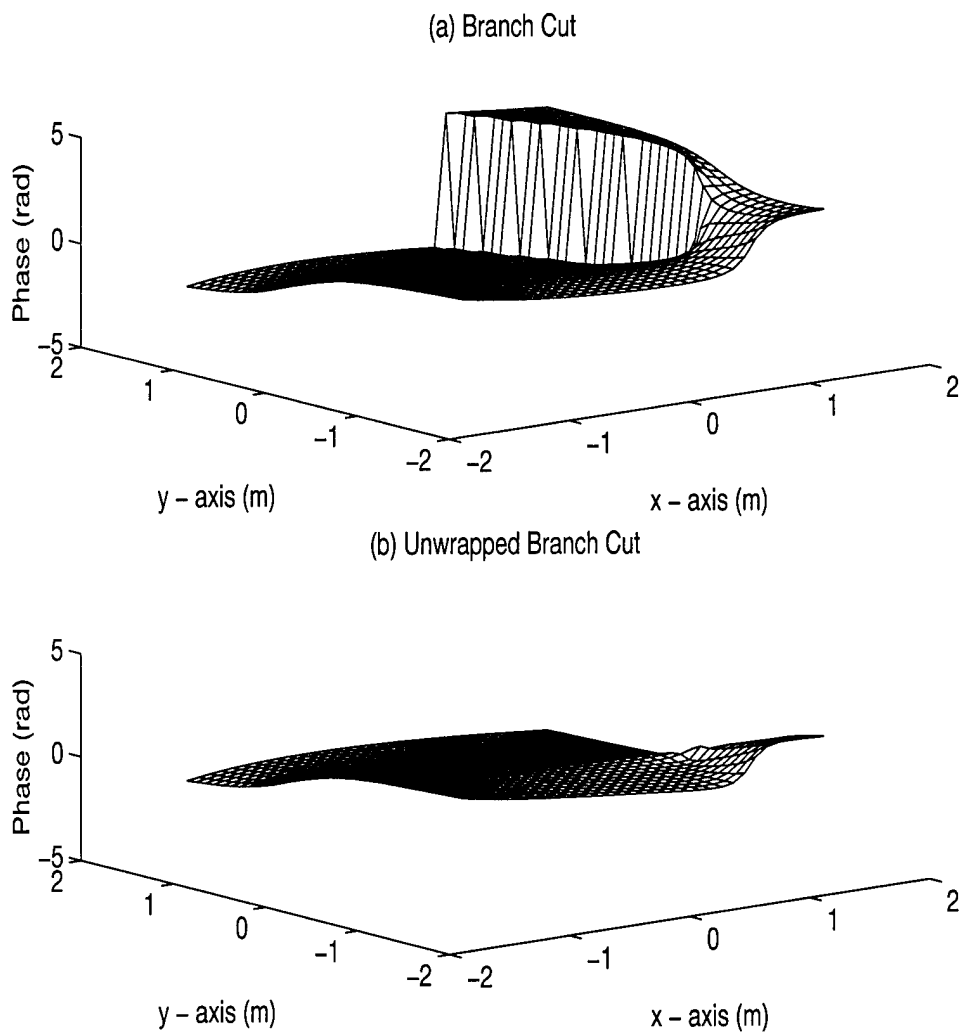


Figure 31. (a) Branch cut and (b) unwrapped branch cut for  $0.4333 \mu\text{rad}$  extended object with Gaussian reflectance.

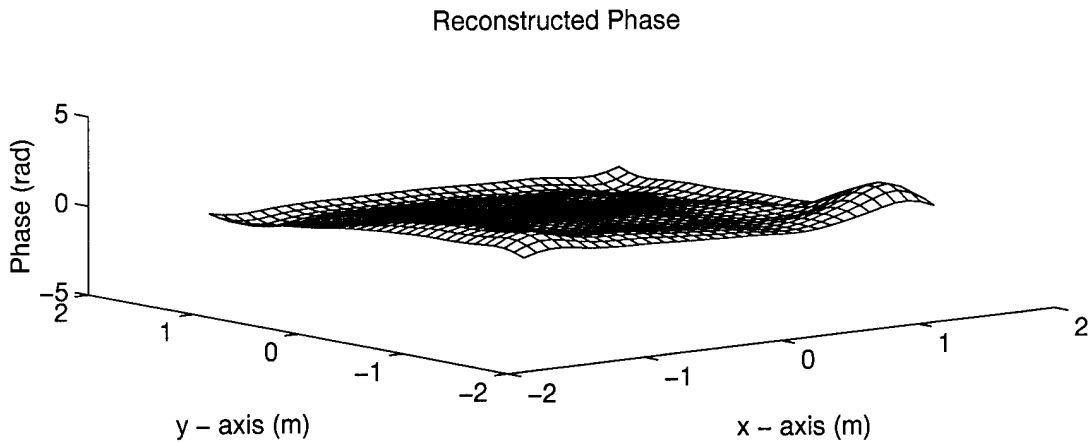


Figure 32. Minimum variance reconstructed phase for  $0.4333 \mu\text{rad}$  extended object with Gaussian average reflectivity profile.

tations of the true phases. The aperture averaged squared phase error corresponding to the object with  $\beta = 0.47$  was 0.3770. This phase error squared corresponded to 12.23 % of the aperture averaged input phase variance. The phase reconstructions for larger values of  $\beta$  appeared not to be sampled sufficiently. The theoretical expected aperture averaged mean squared phase error was shown to be less for the minimum variance reconstructor than for the least squares reconstructor discussed in Section 3.4. The least squares reconstructor used in the theoretical comparison was a new implementation of the least squares formalism. The same error metric as that for the minimum variance reconstructor was used. The error metric is illustrated in equation (40). Identical elementary functions,  $r_j(\vec{x})$ , were used for both the minimum variance and least squares reconstructors in this comparison. The only difference between the minimum variance and least squares reconstructors is in the choice of the optimal reconstruction matrix,  $M_{jn}$ . The minimum variance formalism makes use of the statistical properties of the object (in the form of measurement plane phase covariances) in determining the optimal reconstruction matrix. The new least squares reconstructor, just as conventional least squares reconstructors, does not use any statistical information in determining the reconstruction matrix,  $M_{jn}$ . The new least squares reconstructor has an advantage over conventional least

squares reconstructors in that phase estimates can be obtained at any point in the measurement plane clear aperture.

The performance of the minimum variance wavefront reconstructor was demonstrated for an extended random object with a Gaussian average reflectivity profile. The Gaussian average reflectivity used in simulation matched the average reflectivity profile used in the theoretical determination of the optimal solution matrix,  $M_{jn}$ . No measurement noise or estimation errors in the object average reflectivity profile were assumed in the previous analysis. The performance of the minimum variance reconstructor in the presence of noise must still be demonstrated. Since the reconstructor depends on prior knowledge of the object support and the average reflectivity profile of the object, the sensitivity to mismatches between the theoretical and simulated object average reflectivity profile is of interest. The next section looks at the performance of the minimum variance reconstructor under these sub-optimal conditions.

#### *4.4 Performance and Sensitivity Analysis*

This section discusses the performance of the minimum variance reconstructor in the presence of estimation errors and noise. The estimation errors considered are due to mismatches in the object average reflectivity profile. The average reflectivity function of the object directly affects the phase covariances in the measurement plane. Therefore, the effect of average reflectivity variations on the performance of the minimum variance wavefront reconstructor need to be understood. Three object average reflectivity mismatches between the theoretical development and simulation of the minimum variance wavefront reconstructor are investigated. The first average reflectivity mismatch incorporates finite object dimensions in the simulation of the minimum variance wavefront reconstructor. A Gaussian average reflectivity profile with infinite extent is used to compute the reconstruction matrix,  $M_{jn}$ , in the theoretical development of the minimum variance wavefront reconstructor. In simulation,



the average reflectivity profile of the object was set to zero outside the boundaries of the object support. The aperture averaged mean squared phase error is calculated for this average reflectivity mismatched case. The second average reflectivity estimation error investigates mismatches between the shape of the theoretical and simulated object average reflectivity profiles. Two aspects of shape mismatches are investigated. The first aspect involves mismatches between the spatial details of the theoretical and simulated object average reflectivities. The theoretical object average reflectivity profile was assumed a Gaussian with infinite spatial extent while the spatial features of the simulated average reflectivity profile were assumed to be a + or an  $\times$ . The second shape mismatch assumes a Gaussian average reflectivity profile with infinite spatial extent in the theory but the simulated average reflectivity profile is constant with spatial features of a +. The third estimation error investigated is a mismatch between the expected size of the object and the actual size of the object. Differences in apparent object size will occur because of variations in the orientation of the object with respect to the optical axis of the imaging system.

The performance of the minimum variance reconstructor in the presence of additive white Gaussian noise corrupting the  $\Delta\phi$  measurements is also discussed. Additive white Gaussian noise is the type of noise expected in photon noise limited processes [26].

The first estimation error investigated involved a mismatch between the theoretical and simulated object average reflectivities. The theoretical object average reflectivities were assumed to be Gaussian with infinite extent while the simulated object average reflectivities were assumed to be truncated Gaussians. For the truncated Gaussian, the average reflectivity profile is given by equation (54) but the value of the average reflectivity outside the support region of the object was set to zero. The  $e^{-1}$  angular subtense of the theoretical object average reflectivities and the angular subtense of the object support of the simulated average reflectivities was 0.4333, 0.8667, 1.3000, 1.7333, and 2.1667  $\mu\text{rad}$ , respectively. In Figure 33, the

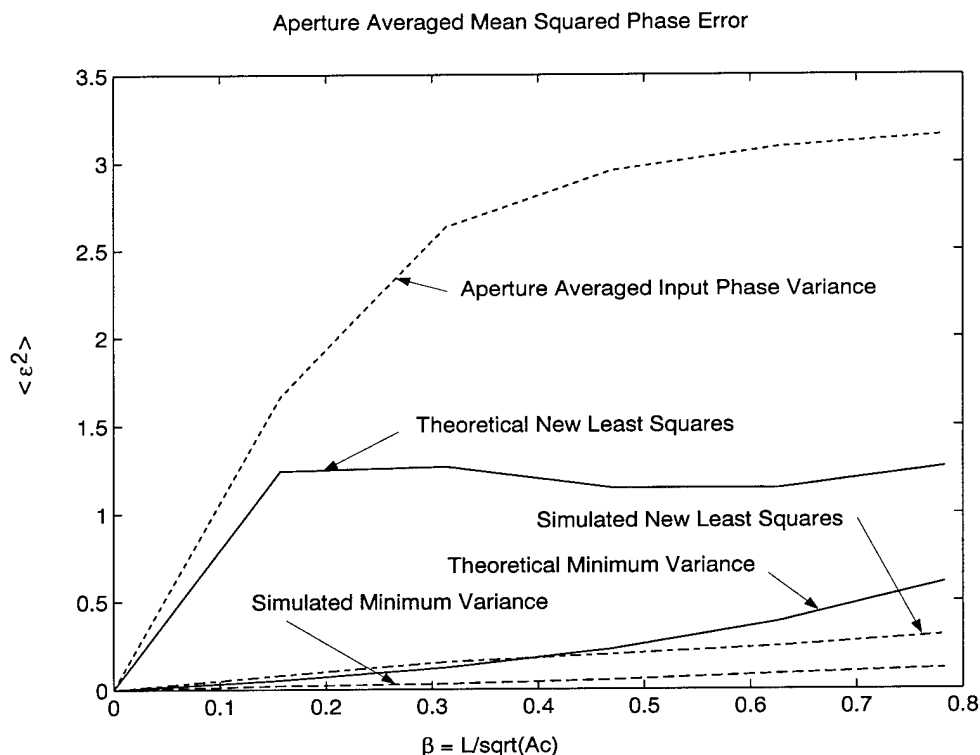


Figure 33. Minimum aperture averaged mean squared phase error for theoretical (bottom solid line) and simulated (long dashes) minimum variance results. Minimum aperture averaged mean square phase error for theoretical (top solid) and simulated (dash - dot) results for the new least squares reconstructor. The aperture averaged input phase variance is also shown (dotted line). The true phase map was used to provide phase differences. Gaussian average reflectivity profiles with infinite spatial extent were used in the theoretical development of the aperture averaged mean squared phase error. Truncated Gaussian average reflectivity profiles were used for the simulated objects. The horizontal axis is the sampling parameter,  $\beta$ . The measurement plane sampling density was 8 by 8 evenly spaced samples in a 3 m by 3 m square collecting aperture. For the simulation results, the number of independent measurement plane frames used to determine  $\langle \epsilon^2 \rangle_s$  were 100.

simulated aperture averaged mean squared phase error was determined as a function of  $\beta$  for both the minimum variance and least squares methods and compared to the corresponding theoretical values. The new least squares reconstructor discussed in Section 3.4 was used to make the comparison. For the simulated results, the true phase map was used to determine the measurement plane phase differences. The simulated aperture averaged mean squared phase error does not include the effects of branch cuts or phase wraps. Since both the phase wraps and the  $2\pi$  discontinuities associated with the branch cuts are unwrapped from the measurement plane reference phase, the simulated aperture averaged mean squared phase error is expected to be lower than the corresponding theoretical aperture averaged mean squared phase error.

The simulated aperture averaged mean squared phase error results are smaller than those shown in Figure 24 for both the least squares and minimum variance methods. The coherence area for the truncated Gaussian in the simulation is larger than the coherence area for the Gaussian with infinite extent used in the theoretical estimation of the aperture averaged mean squared phase error. Hence, the simulated value of  $\beta$  is less than the theoretical value of  $\beta$ , resulting in a lower aperture averaged mean squared phase error for the simulated case.

Figure 34 shows the comparison of the aperture averaged mean squared phase error between the G & R least squares reconstructor discussed in Section 2.2 and the minimum variance reconstructor. The reference phases were used to determine the phase differences. The presence of the phase wraps is somewhat mitigated by only using coarse grid points to compute the aperture averaged mean squared phase error instead of integrating across the measurement plane aperture. Therefore, the reference phase map is used for comparisons between the simulated minimum variance and G & R least squares sampled aperture averaged mean squared phase error. The average reflectivity profile of the theoretical object was assumed to be a Gaussian with infinite extent and the simulated average reflectivity was assumed a truncated

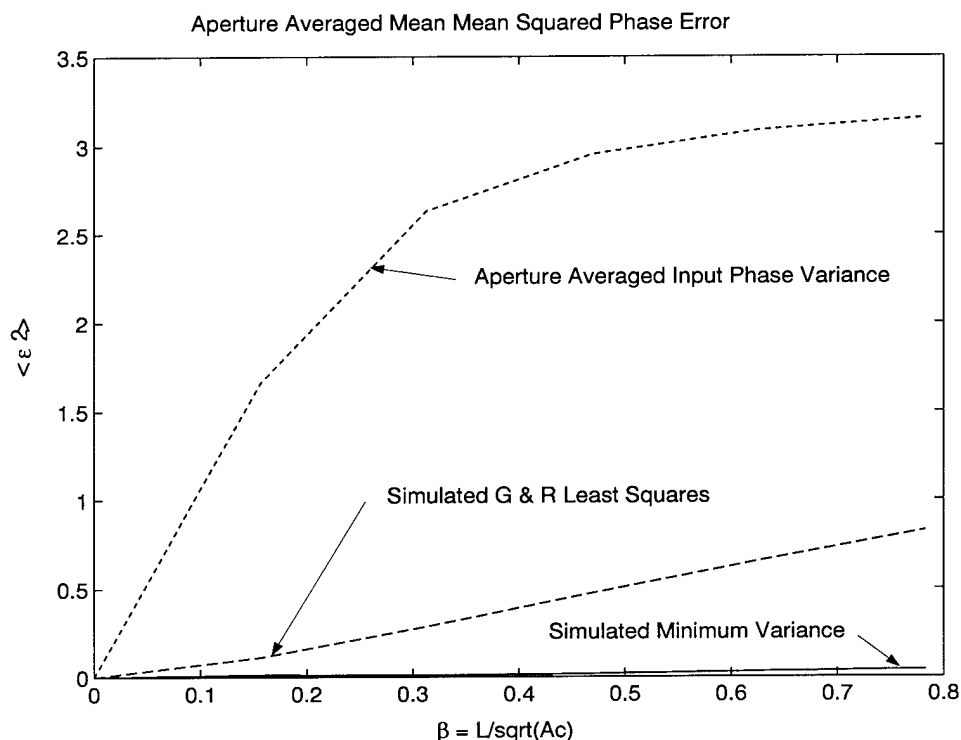


Figure 34. Minimum aperture averaged mean squared phase error for the minimum variance (solid line) and G & R least squares (long dashes) formalisms. Also included is the input aperture averaged mean squared error (short dashes). The horizontal axis is the sampling parameter,  $\beta$ . Gaussian average reflectivity profiles with infinite spatial extent were used in the determination of the optimal reconstruction matrix for minimum variance simulation. Truncated Gaussian average reflectivity profiles were used for the simulated objects in both the minimum variance and G & R least squares methods.

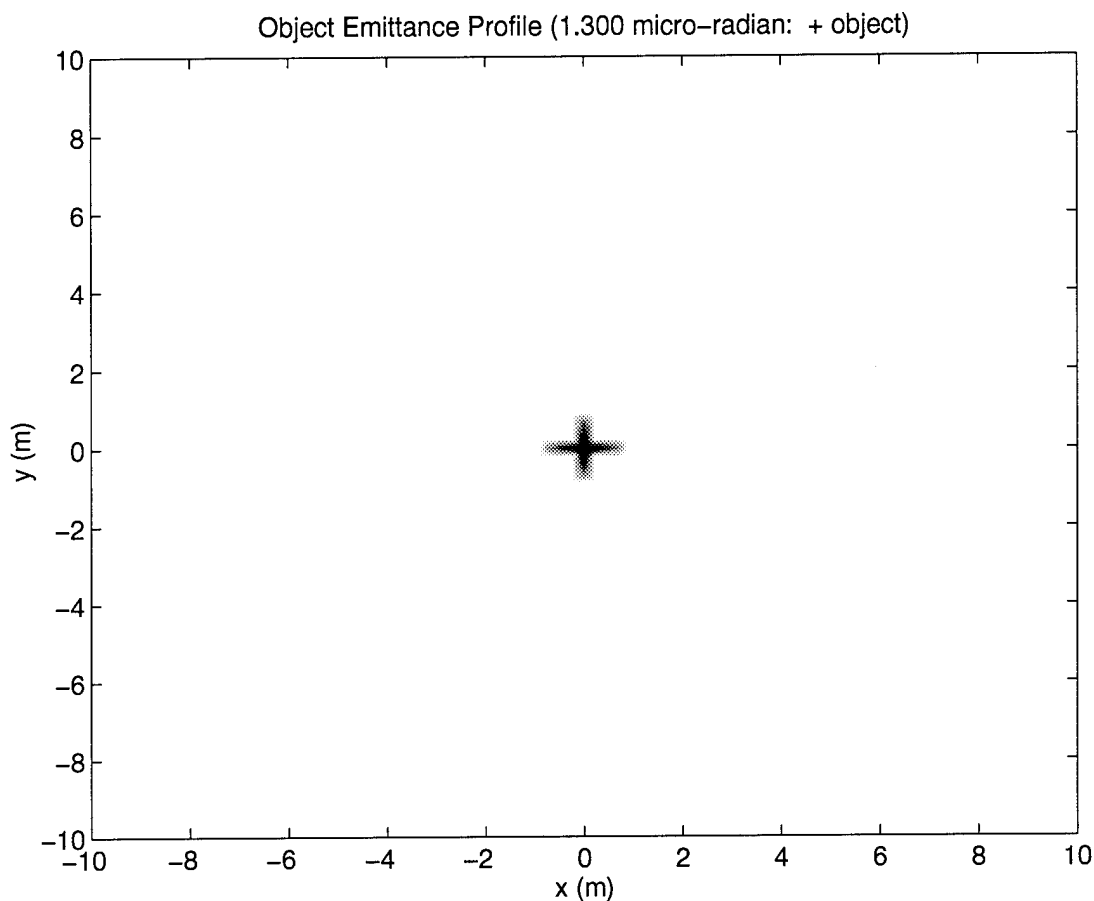


Figure 35. Average reflectivity distribution for a random + object with 1.300  $\mu\text{rad}$  angular subtense.

Gaussian. The number of random frames used to determine the aperture averaged mean squared phase error for both the G & R least squares and minimum variance methods was 100. In terms of the aperture averaged mean squared phase error, Figure 34 shows that the minimum variance reconstructor out performs the G & R least squares wavefront reconstructor over the useful range of  $\beta$ .

To investigate the first of the two shape mismatches between the theoretical and simulated object average reflectivities, the random simulated object average reflectivity was assumed to have the shape of a +. For a useful wavefront reconstructor, the reconstruction process should not be overly sensitive to mismatches between the theoretical and simulated shape of the object average reflectivity profile. The

theoretical object was assumed to have a Gaussian average reflectivity profile with infinite extent as described by equation (54). The parameter  $R$  was chosen so that the  $e^{-1}$  width of the theoretical object average reflectivity was  $1.300 \mu\text{rads}$ . The simulated object average reflectivity was the product of a unit magnitude average reflectivity in the shape of a cross with the Gaussian envelope function given by equation (54). Figure 35 shows the simulated object average reflectivity profile. The simulated object average reflectivity was set to zero outside the boundaries of the object support. The angular subtense of the simulated object was  $1.300 \mu\text{rads}$ .

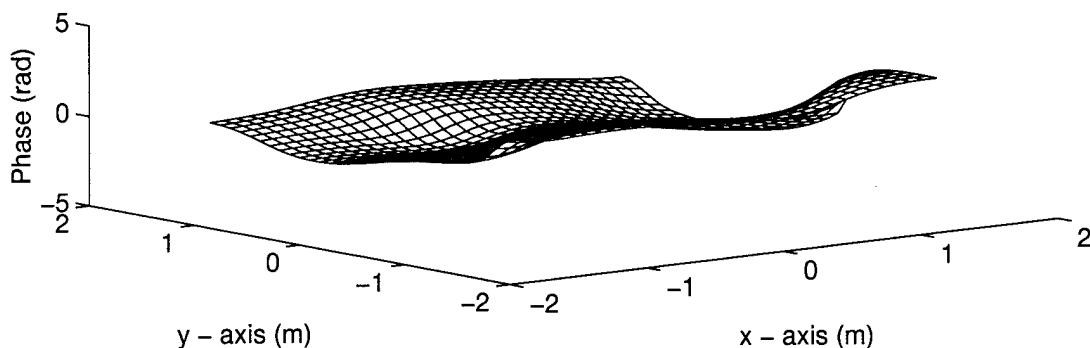
The random object field for the + object was Fourier transformed and the reference phase distribution was formed. The reference phase was unwrapped resulting in the measurement plane true phase. Figure 36 illustrates the (a) true phase and the (b) reconstructed phase for one measurement plane phase realization.

To see the differences between the true and reconstructed instantaneous phase maps pictured in Figure 36, a plot of the point-to-point phase error squared is useful. The phase error squared is the pointwise square of the difference between the true and the reconstructed phases. Figure 37 plots the phase error squared for the instantaneous phases depicted in 36. The increased error along the edge of the aperture results from errors estimating the edge points of the aperture. Estimates of points on the edge of the aperture have fewer neighboring measurement points than estimates in the interior of the aperture and are therefore less precise.

The instantaneous images were obtained by Fourier transforming the measurement plane fields. Averaging was accomplished by pointwise averaging the irradiance of 100 separate image frames. Figure 38 shows the true and reconstructed averaged images.

The features of the cross are distinguishable on the reconstructed object and true image. No measurement noise was assumed so the average true image represented the diffraction limited image of a random cross object obtained from a 3 m by 3 m square collecting aperture. To better see the differences between the true and

(a) True Phase (1.300 micro-radian: + object)



(b) Reconstructed Phase

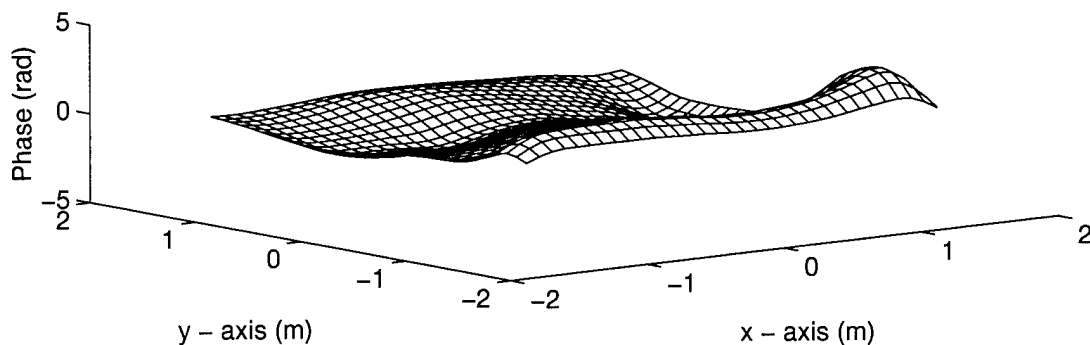


Figure 36. Measurement plane phase maps of (a) true phase and (b) reconstructed phase for  $1.300 \mu\text{rad}$  random cross object. The simulated average reflectivity profile was the product of a unit amplitude + object subtending  $1.300 \mu\text{rads}$  and a Gaussian envelope function. The simulated average reflectivity was zero outside the boundaries of the object support. The theoretical object average reflectivity was assumed a Gaussian with infinite spatial extent. The  $e^{-1}$  width of the theoretical object average reflectivity was  $1.300 \mu\text{rads}$ .

Phase Error Squared (1.300 micro-radian: + object)

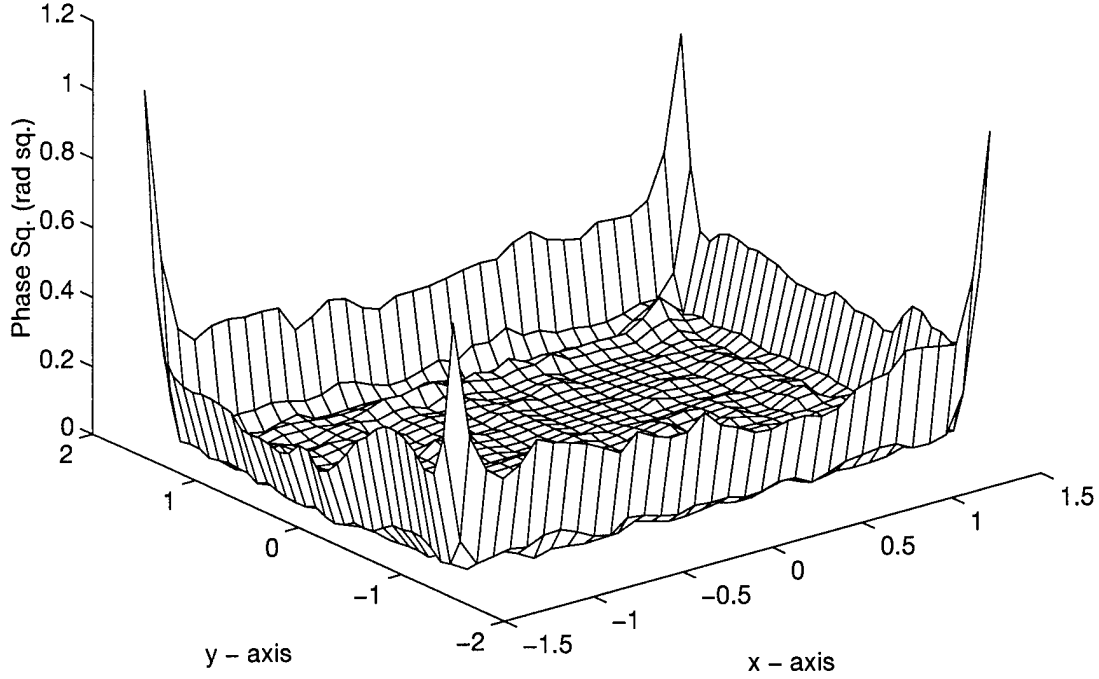


Figure 37. Measurement plane phase error squared for 1 frame of 1.300  $\mu\text{rad}$  random cross.

reconstructed images, a plot of the image error squared is provided. The point by point square of the difference between the averaged true and averaged reconstructed image was determined. The image error squared is shown in Figure 39.

The plot in Figure 39 shows that the reconstructed image formed by using 8 by 8 samples across the measurement plane aperture and the minimum variance wavefront reconstruction formalism produces a near diffraction limited image of the object in the noise free case. The magnitude of the image error is given by,

$$\epsilon_{img}(\vec{x}) = \left| \frac{I_t(\vec{x}_i)}{I_t(0)} - \frac{I_r(\vec{x}_i)}{I_r(0)} \right|, \quad (58)$$



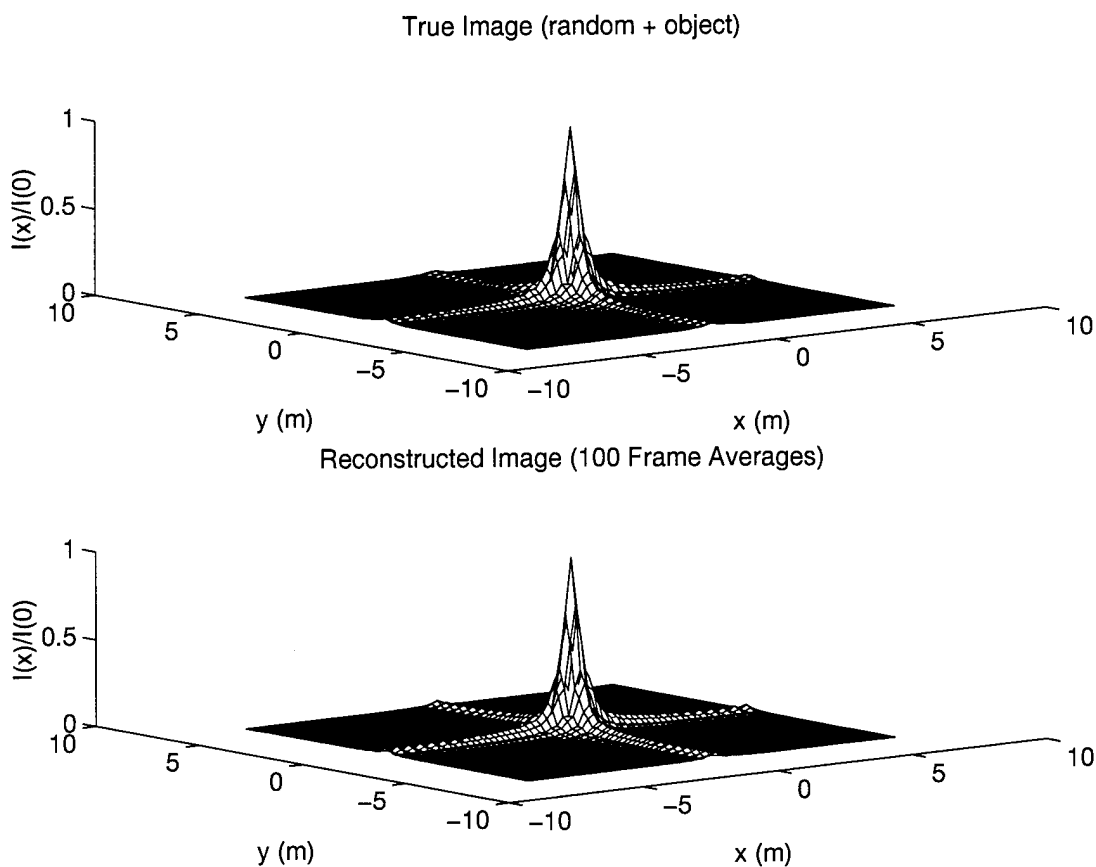


Figure 38. (a) True image and (b) reconstructed image for cross object with  $1.300 \mu\text{rad}$  finite extent. The measurement plane sampling density was 8 by 8 evenly spaced samples in a 3 m by 3 m square collecting aperture. The number of independent image frames used to average was 100.

Image Error Squared (1.300 micro-radian: + object)

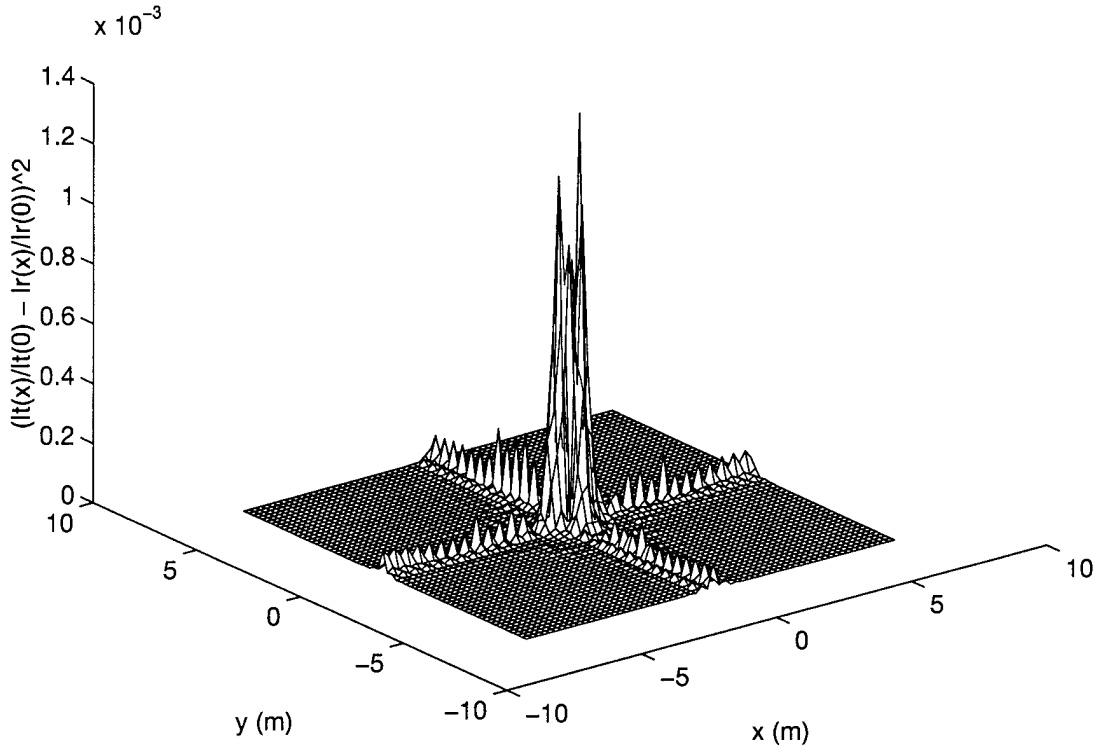


Figure 39. Image error squared for an object with a Gaussian average reflectivity profile and spatial structure in the form of a +. The object had a 1.300  $\mu\text{rad}$  angular subtense. The quantities,  $I_t(x)$ , and,  $I_r(x)$ , are the true and reconstructed image irradiance at a point, respectively.

where,  $I_t(\vec{x}_i)$ , is the true irradiance at image plane spatial coordinate  $x_i$ . The quantity,  $I_r(\vec{x}_i)$ , is the reconstructed image plane irradiance using the minimum variance formalism. By evaluating equation (58), the maximum difference between the true and reconstructed averaged irradiance values was determined to be 3.72 % ( $[\epsilon_{img}(\vec{x})]_{max} = 0.0372$ ). The reconstructed image is pointwise equal to the diffraction limited image to within this percentage.

By looking at the true and reconstructed averaged images in Figure 38, the features of the cross are apparent. To demonstrate that the cross features of the true and reconstructed averaged images are reproductions of object features and not

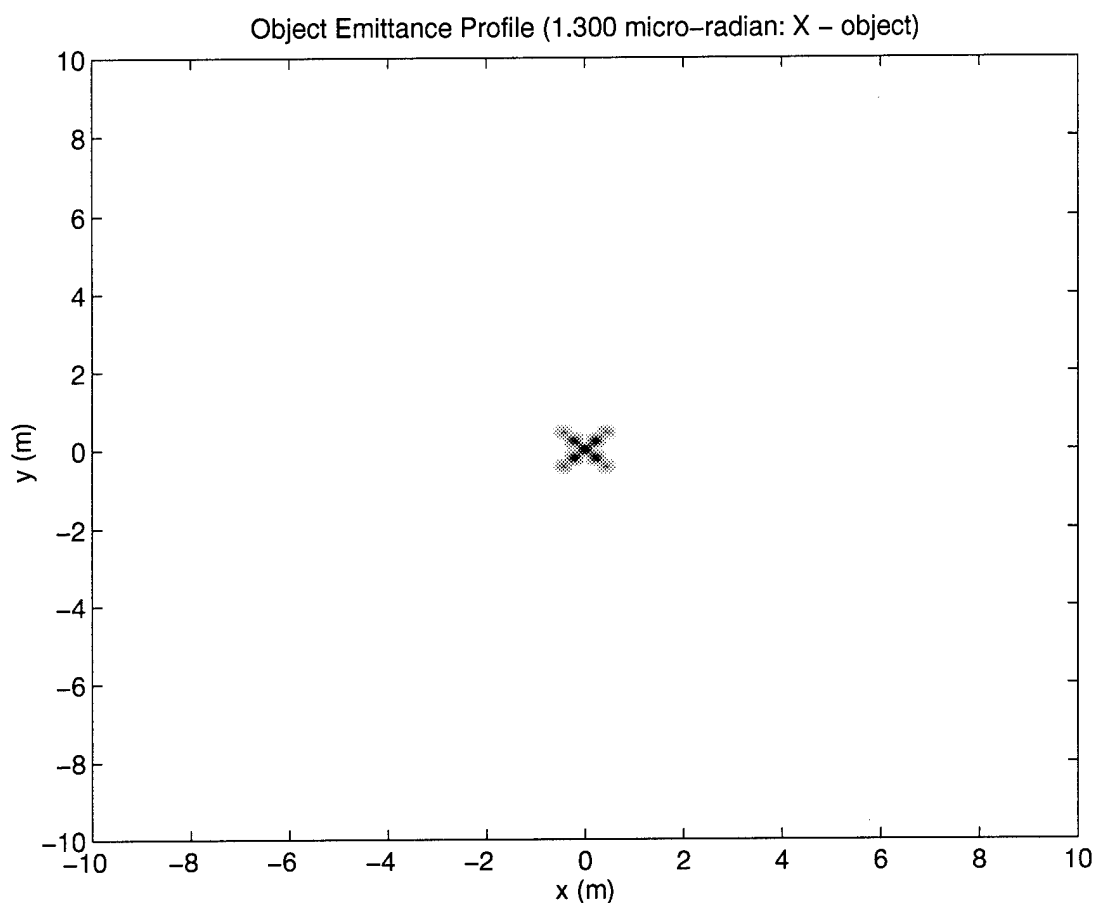


Figure 40. Average reflectivity distribution for a random  $\times$  object with  $1.300 \mu\text{rad}$  angular subtense.

measurement plane aperture effects, the  $+$  object will be rotated 45 degrees and the simulation repeated. If features appear in the true and reconstructed averaged images along the rotated axis then the structural features of the object are being sensed by the image detection process.

Figure 40 shows an object average reflectivity profile for an object which looks like an  $\times$  but has a spatial average reflectivity distribution given by equation (54) along the surface of the  $\times$ .

The simulated average reflectivity profile is the product of the Gaussian envelope function given in equation (54) and a unit amplitude random  $\times$  object. The average reflectivity profile is set to zero outside the boundaries of the object support.

The average reflectivity at the tips of the  $\times$  is smaller than the on axis average reflectivity by approximately 63 %. The true and reconstructed averaged images were determined for 100 independent image frames. No measurement noise was assumed so the averaged true image represented the diffraction limited simulated image of the  $\times$  object obtained from a 3 m by 3 m square collecting aperture. Figure 41 shows the a) true and b) reconstructed averaged images for 100 frame averages. In both the true and reconstructed averaged images, a bulge appears in the expected position of the  $\times$ . This bulge was absent from the averaged true and reconstructed images corresponding to the  $+$  object in Figure 38. Detailed features of the cross are not present in the true and reconstructed averaged images because the separation of the tips of the  $\times$  object is equal to the diffraction limit of the imaging system. The true and reconstructed images are unresolved and only gross features are discernible. The presence of the bulge in the true and reconstructed averaged images corresponding to the  $\times$  object indicates the presence of spatial object features in the true and reconstructed averaged images.

The point by point square of the difference between the averaged true and averaged reconstructed image corresponding to the random  $\times$  simulated object was determined. The image error squared is shown in Figure 42.

The plot in Figure 42 shows that the reconstructed image formed by using 8 by 8 samples across the measurement plane aperture and the minimum variance wavefront reconstruction formalism produces a near diffraction limited image of the object in the noise free case. By evaluating equation (58), the maximum difference between the true and reconstructed averaged irradiance values was determined to be 3.65 % ( $[\epsilon_{img}(\vec{x})]_{max} = 0.0365$ ). The reconstructed image is pointwise equal to the diffraction limited image to within this percentage. The small differences between the true and reconstructed averaged images indicates that the reconstruction process does not require a detailed description of the theoretical average reflectivity profile to reconstruct spatial average reflectivity features in the simulation.

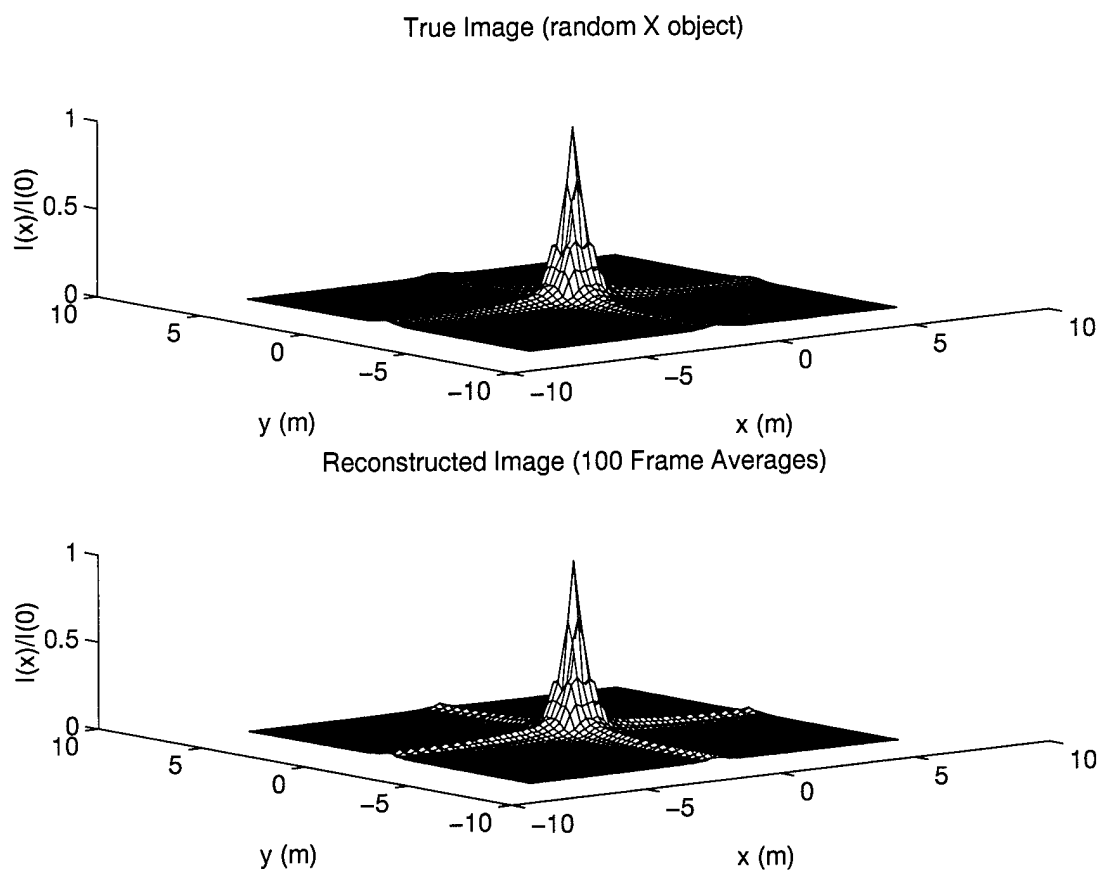


Figure 41. (a) true image and (b) reconstructed image for  $\times$  object with  $1.300 \mu\text{rad}$  finite extent. The measurement plane sampling density was 8 by 8 evenly spaced samples in a 3 m by 3 m square collecting aperture. The number of independent image frames used to average was 100.

Image Error Squared (1.300 micro-radian: X - Object)

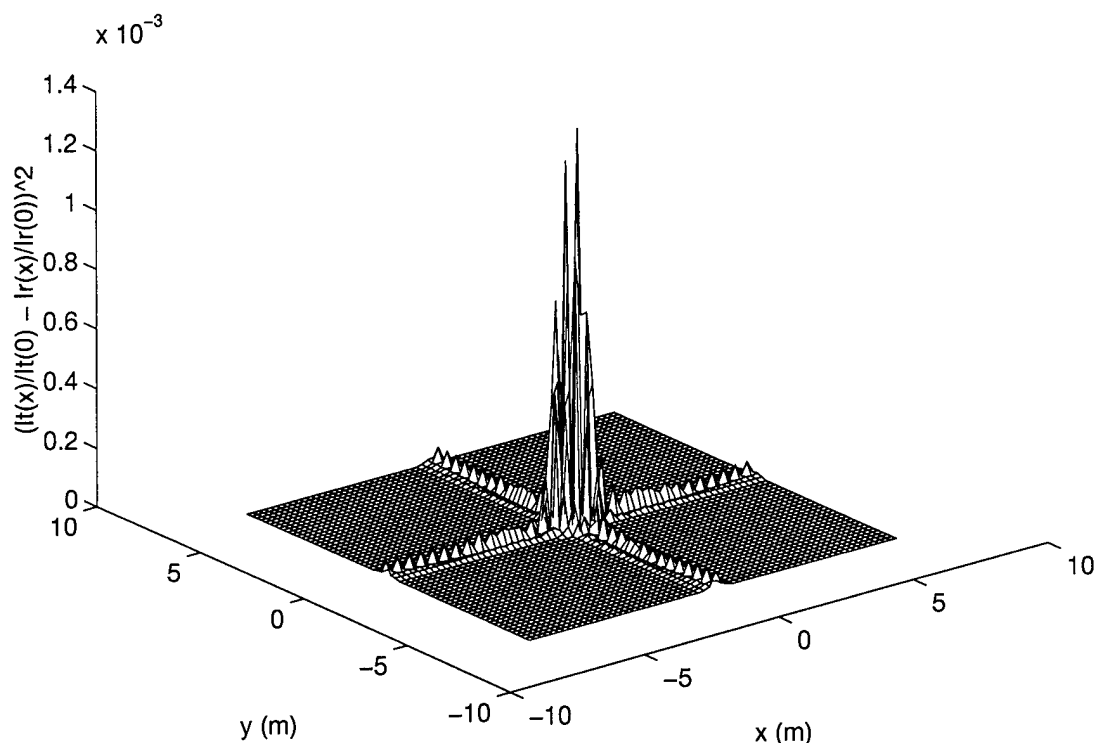


Figure 42. Image error squared for an object with a Gaussian average reflectivity profile and spatial structure in the form of an  $\times$ . The object had a 1.300  $\mu$ rad angular subtense. The quantities,  $I_t(x)$ , and,  $I_r(x)$ , are the true and reconstructed image irradiance at a point, respectively.

The second shape mismatch between the theoretical and simulated object average reflectivities assumed the simulated object average reflectivity profile had a constant value over the support regions of the object. The theoretical object average reflectivity used to determine the optimal reconstruction matrix,  $M_{jn}$ , was assumed to be the spatially Gaussian average reflectivity profile given by equation (54). The average reflectivity profile of the simulated object was in the shape of a  $+$  but had a constant magnitude equal to the value of the on axis average reflectivity of the theoretical object. The average reflectivity profile of the simulated object is illustrated in Figure 43.

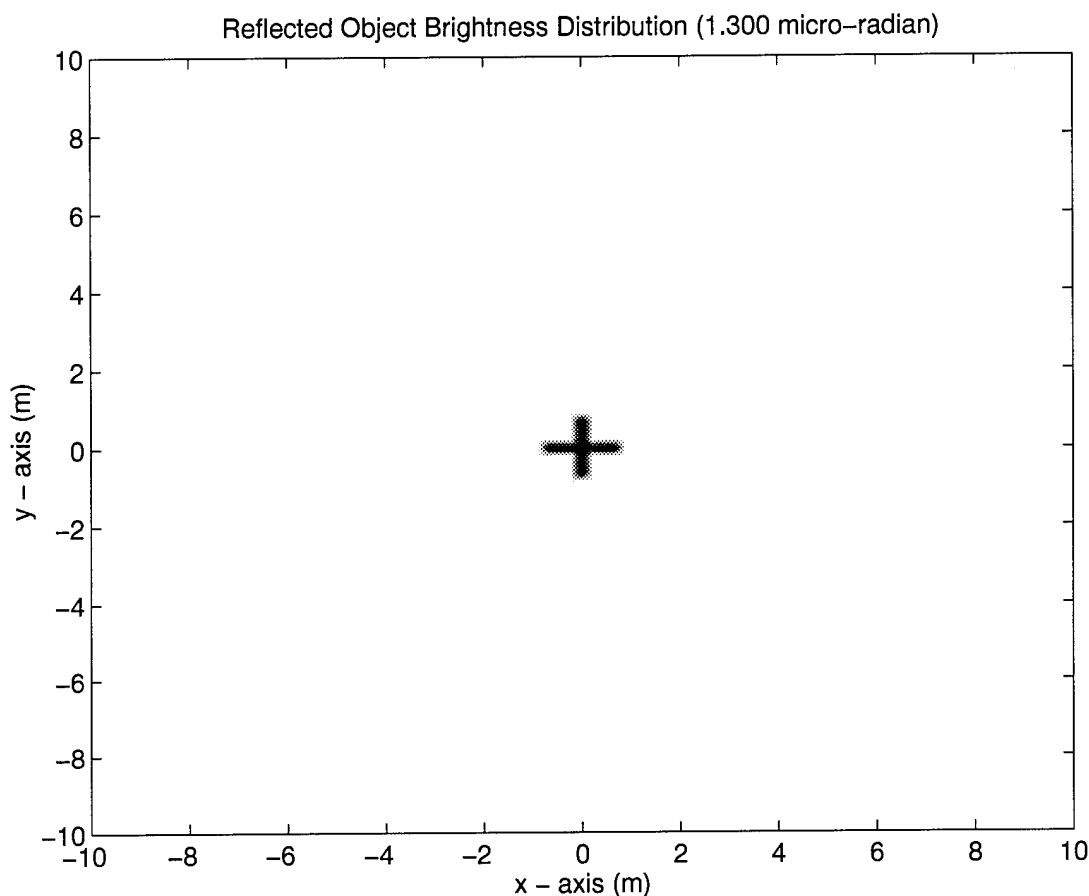
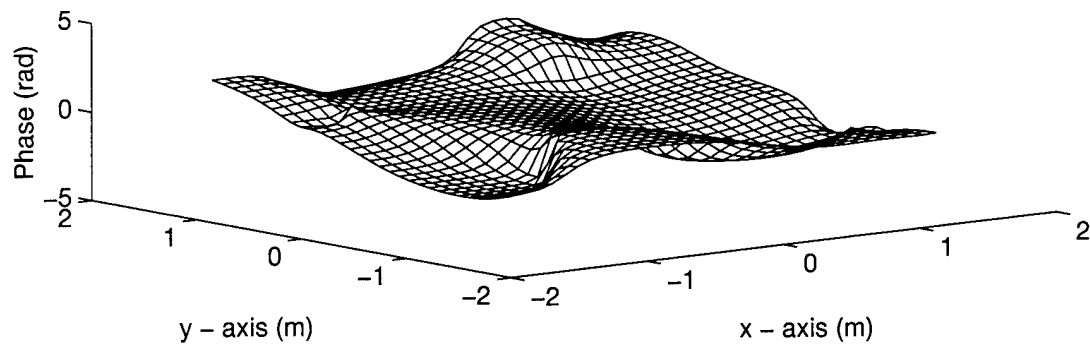


Figure 43. Average reflectivity distribution for a random cross object with 1.300  $\mu\text{rad}$  angular subtense and a constant average reflectivity. The theoretical object average reflectivity was a Gaussian with infinite extent. The simulated object average reflectivity was constant over the support regions of the object and zero elsewhere.

The random object field for the + object was Fourier transformed and the reference phase distribution was formed. The reference phase was unwrapped resulting in the measurement plane true phase. Figure 44 illustrates the (a) true phase and the (b) reconstructed phase for one measurement plane phase realization.

The differences between the true and reconstructed instantaneous phase maps pictured in Figure 44 are shown by plotting the phase error squared. Figure 45 plots the phase error squared for the instantaneous phases shown in 44. As illustrated by Figure 45, the true and reconstructed phases are similar to each other except along

(a) True Phase (1.300 micro-radian: cross object)



(b) Reconstructed Phase

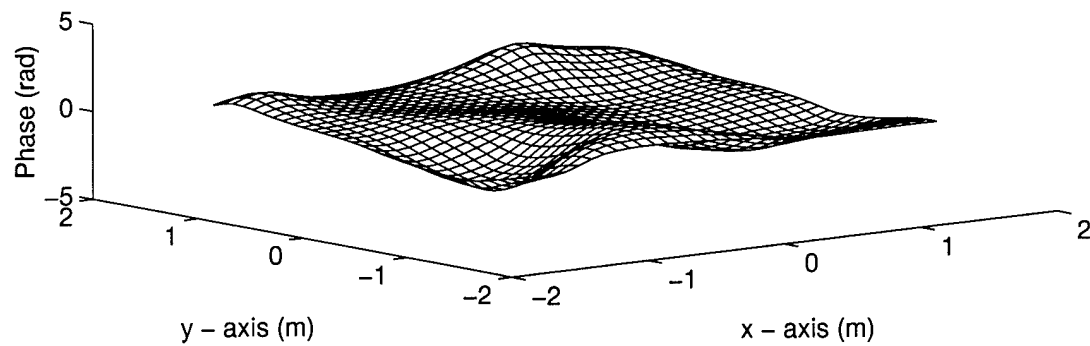


Figure 44. Measurement plane phase maps of (a) true phase and (b) reconstructed phase for 1.300  $\mu\text{rad}$  random cross object.



Phase Error Squared (1.300 micro-radian: Cross Object)

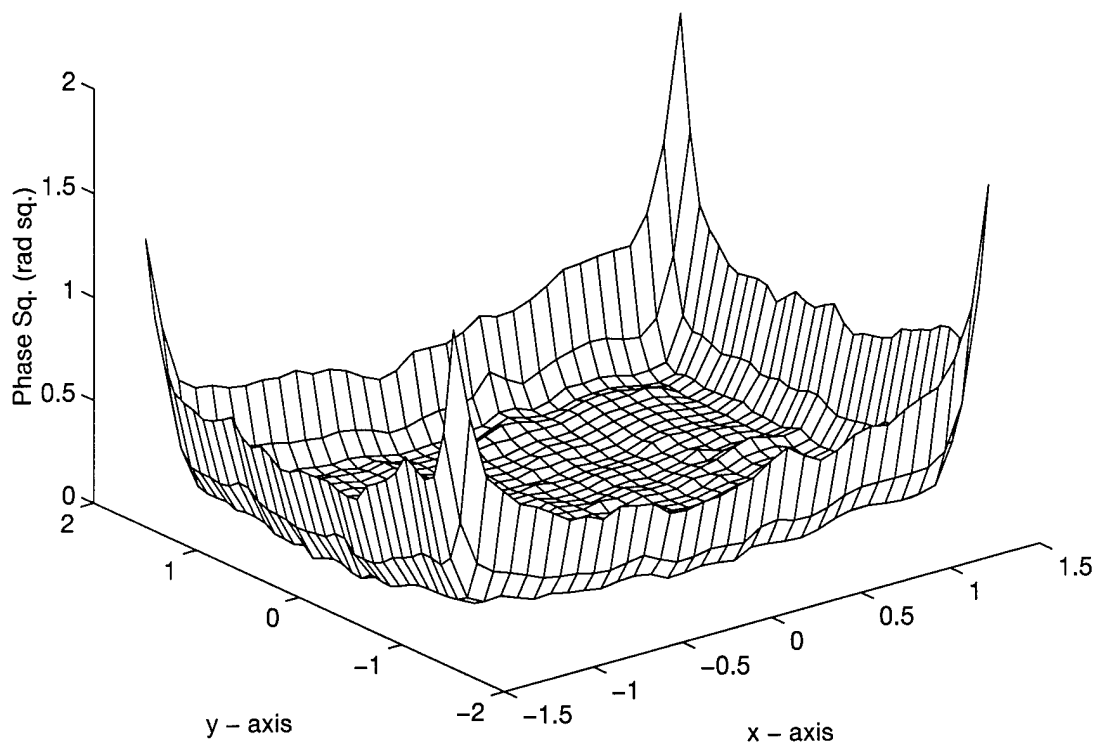


Figure 45. Measurement plane phase error squared for 1 frame of 1.300  $\mu\text{rad}$  random cross.

the edges of the collecting aperture. The instantaneous images were obtained by Fourier transforming the measurement plane fields. Averaging was accomplished by pointwise averaging the irradiance of 100 separate image frames. Figure 46 shows the true and reconstructed averaged images. The true and reconstructed averaged images appear similar to one another. To better see the differences between the true and reconstructed averaged images, the image error squared was determined. The image error squared is shown in Figure 47.

Figure 47 shows that the reconstructed averaged image and the diffraction limited averaged image of the cross are qualitatively similar. The maximum difference between any spatial point of the true image and the reconstructed image in accordance with equation (58) was 8.24 % ( $[\epsilon_{img}(\vec{x})]_{max} = 0.0824$ ). Furthermore,

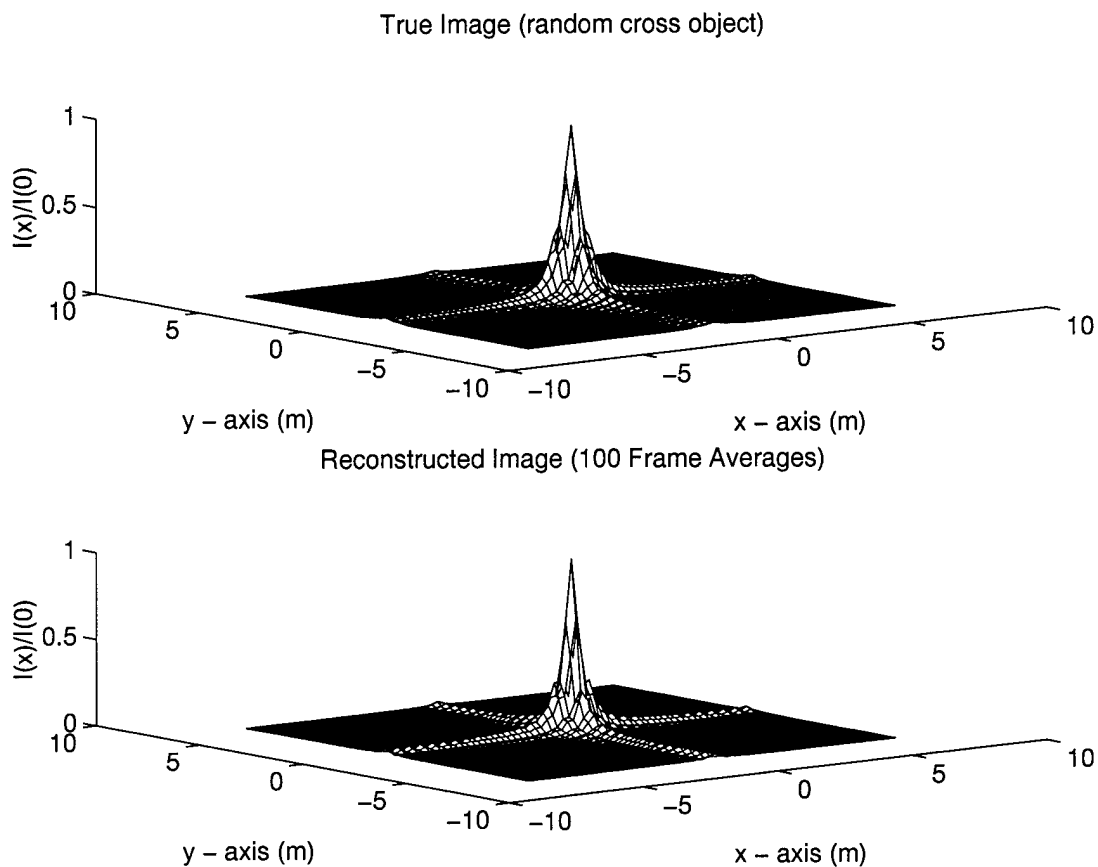


Figure 46. (a) True image and (b) reconstructed image for cross object with  $1.300 \mu\text{rad}$  finite extent. The measurement plane sampling density was 8 by 8 evenly spaced samples in a 3 m by 3 m square collecting aperture. The number of independent image frames used to average was 100.

Image error Squared (1.300 micro-radian: Cross Object)

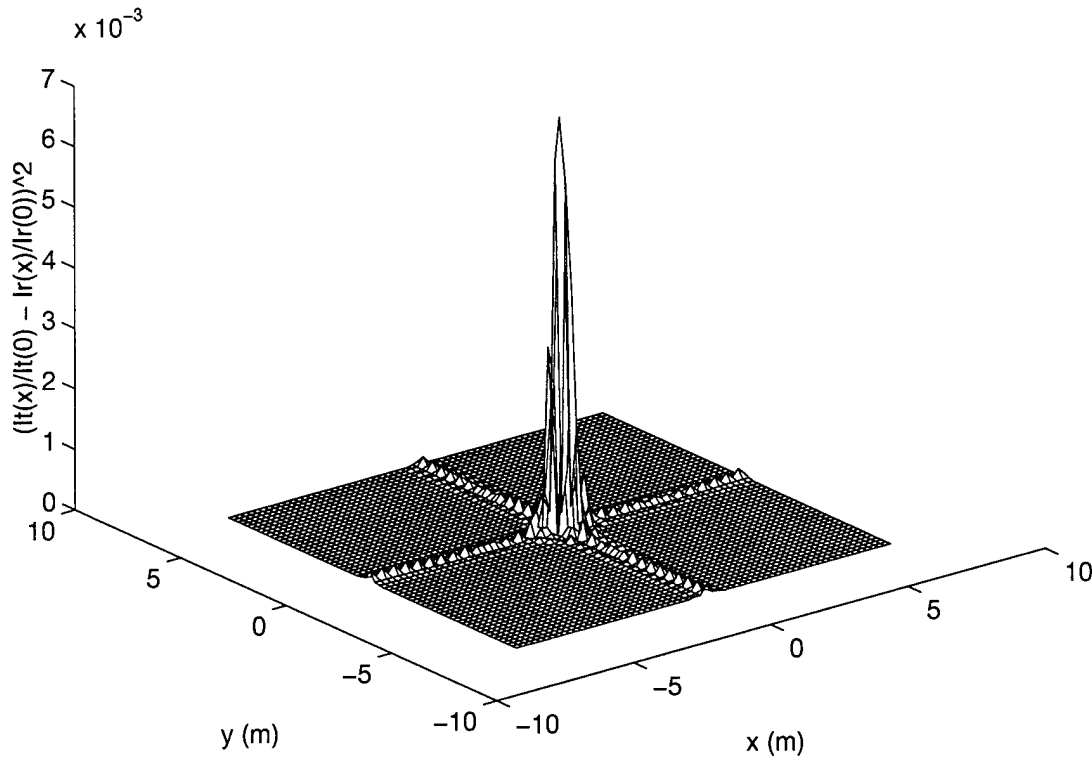


Figure 47. Image error squared for 100 frames of 1.300  $\mu\text{rad}$  random cross object. The quantities,  $I_t(x)$ , and,  $I_r(x)$ , are the image plane irradiances at a point for the true image irradiance and the reconstructed image irradiance, respectively.

this illustrates that the reconstructor performance is not substantially degraded by mismatches in the magnitude between the theoretical and simulated average reflectivities for objects with similar spatial features.

The third estimation error investigated involved mismatches between the theoretical and simulated object sizes. A fundamental assumption in determining the optimal reconstruction matrix,  $M_{jn}$ , in the minimum variance formalism is the dimensions and shape of the average reflectivity distribution of the object. It is reasonable to have some prior knowledge about the object support such as the general shape (circle, rectangle, square). However, a desirable reconstruction process should not be

overly sensitive to mismatches between the expected size of the object and the actual size of the object. To test the sensitivities of the aperture averaged mean squared phase error to mismatches between the theoretical and simulated object sizes, the optimal reconstruction matrix,  $M_{jn}$ , was determined for an object subtending  $1.7333 \mu\text{rad}$ . In the theoretical determination of  $M_{jn}$ , a Gaussian object average reflectivity profile with infinite extent was assumed in accordance with equation (54). The phase covariance was then determined for objects subtending  $1.7333$ ,  $2.1667$ ,  $2.600$ ,  $3.0333$  and  $3.4667 \mu\text{rad}$ . These angles of subtense correspond to object size mismatches of  $0$ ,  $25$ ,  $50$ ,  $75$ , and  $100$  percent. Phase covariances for smaller object size mismatches ( $-25$  and  $-50$  percent) were also determined and similar results were obtained. A fixed  $M_{jn}$  corresponding to a  $1.7333 \mu\text{rad}$  object was used in equation (40) along with the various phase covariances to calculate the aperture averaged mean squared phase error as a function of a mismatch between the theoretical object size and the simulated object size. In the simulation, truncated Gaussian average reflectivities were used with angular subtenses of  $1.7333$ ,  $2.1667$ ,  $2.600$ ,  $3.0333$  and  $3.4667 \mu\text{rad}$ , respectively.

Figure 48 shows the theoretical sub-optimal (solid line) aperture averaged mean squared phase error as a function of object size mismatch. For reference the optimal aperture averaged mean squared phase error for equal theoretical and simulated object size is shown by the dashed line. The aperture averaged input phase variance for a  $1.7333 \mu\text{rad}$  object (dotted line) is also illustrated.

The aperture averaged mean squared phase error is not strongly affected by mismatches between the expected size of the object and the actual size of the object. Errors in size estimation of up to  $100$  percent produce relatively small changes in  $\langle \epsilon^2 \rangle$ . For larger size mismatches, the sampling error begins to dominate and so the relative difference between the optimal and sub-optimal aperture averaged mean squared phase error decreases.

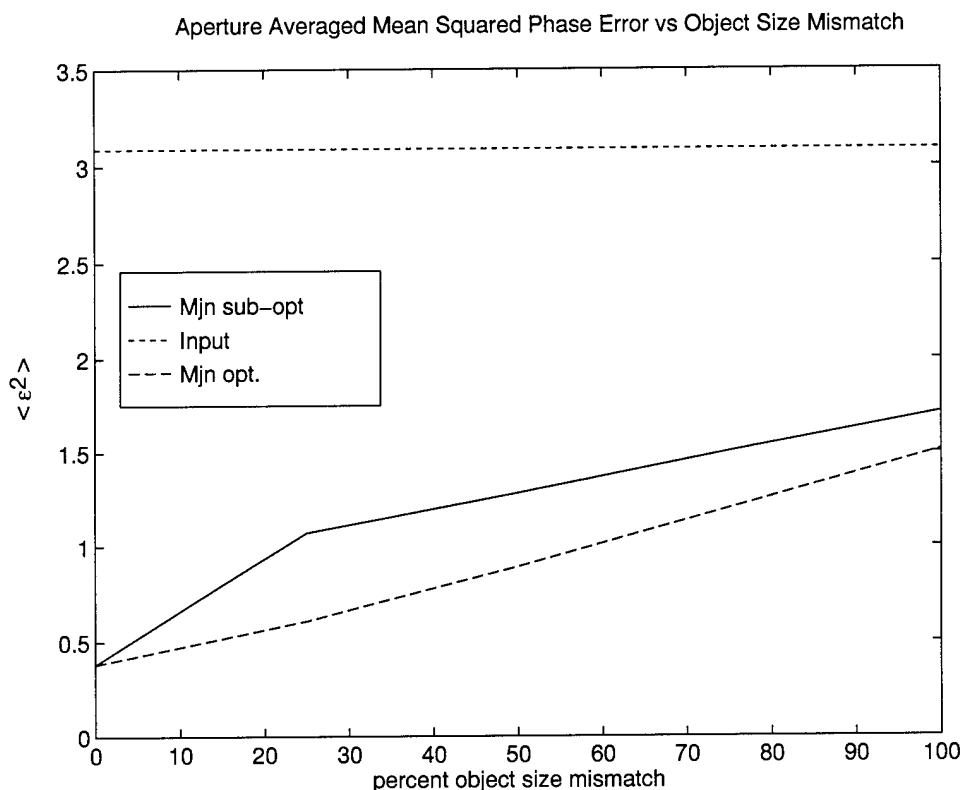


Figure 48. Aperture averaged mean squared phase error as a function of mismatch between expected object size and actual object size. Optimal reconstruction matrix was determined for an object subtending  $1.7333 \mu\text{rad}$ . Horizontal axis shows percentage of mismatch between the assumed object size and the actual object size. The dotted line shows the aperture averaged input phase variance for a  $1.7333 \mu\text{rad}$  object. The solid line shows  $\langle \epsilon^2 \rangle$  as a function of expected to actual object size mismatch. The dashed line shows  $\langle \epsilon^2 \rangle$  for a perfect object size estimation. The theoretical average reflectivity profile was a Gaussian with infinite extent and the simulated average reflectivity profile was a truncated Gaussian.

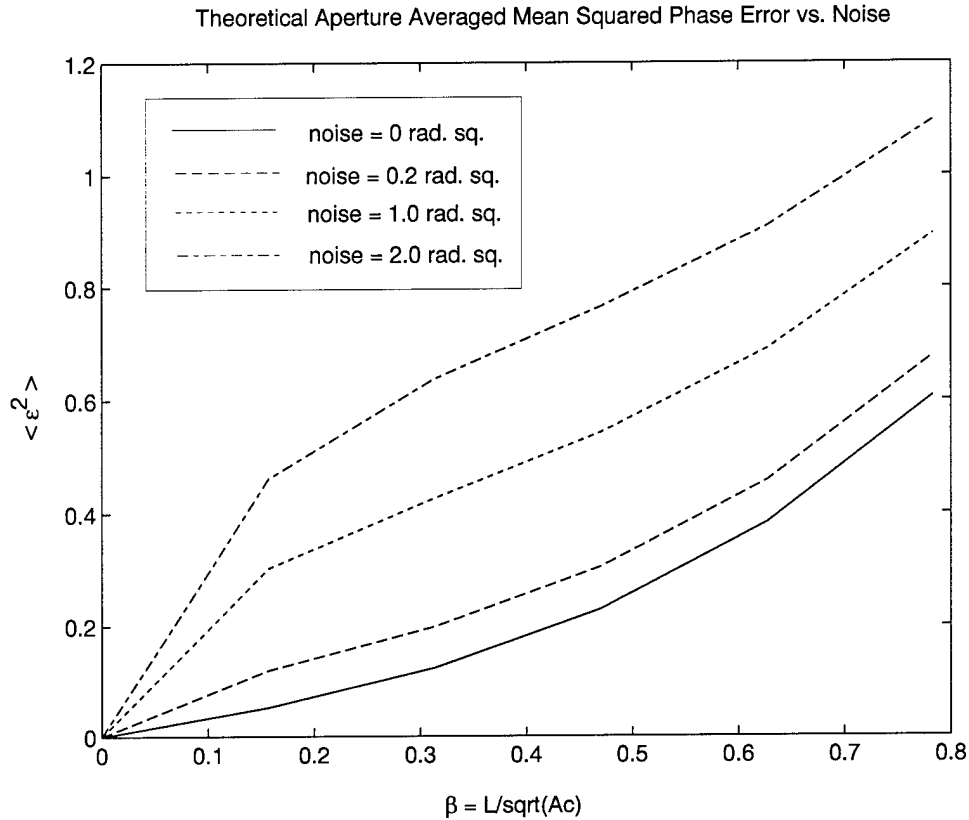


Figure 49. Theoretical minimum variance aperture averaged mean squared phase error as a function of noise level and sampling parameter,  $\beta$ . Additive white Gaussian noise levels were 0 (bottom line), 0.2 (second line from bottom), 1 (third line from bottom), and 2 (top line) radians squared.

Thus far, the results presented have been for noise free cases. The presence of additive white Gaussian noise such as discussed in chapter III will degrade a reconstructors performance. The theoretical determination of the optimal reconstruction matrix was modified in accordance with the discussion outlined in Section 3.6. Equation (53) was used to modify the diagonal terms of the phase difference correlation matrix,  $\Phi_{nm}$ . Figure 49 shows the theoretical aperture averaged mean squared phase error for the minimum variance reconstructor for noise level variances,  $\sigma_n^2$ , of 0, 0.2, 1, and 2 radians squared. The reference phase map was used to determine the phase differences used as inputs to the minimum variance wavefront reconstructor. The

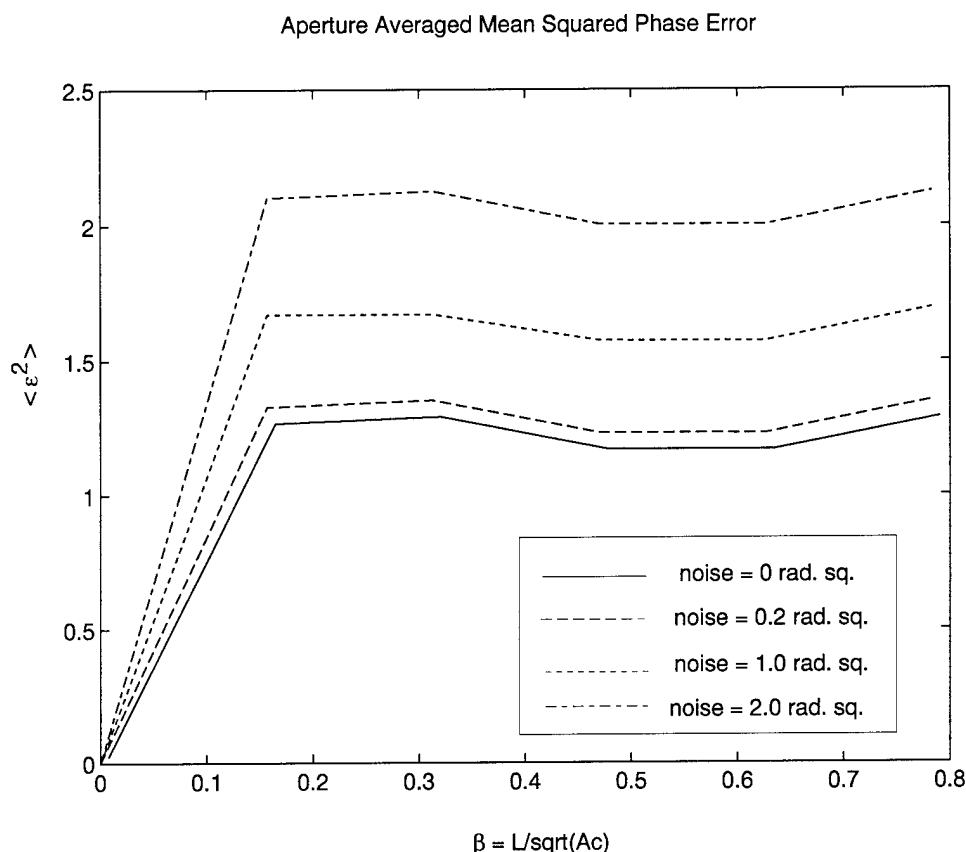


Figure 50. Theoretical new least squares aperture averaged mean squared phase error as a function of noise level and sampling parameter,  $\beta$ . Additive white Gaussian noise levels were 0 (bottom line), 0.2 (second line from bottom), 1 (third line from bottom), and 2 (top line) radians squared.

horizontal axis is the sampling parameter,  $\beta$ . As expected, the aperture averaged mean squared phase error increases for an increase in the noise.

A plot of the theoretical aperture averaged mean squared phase error for the least squares reconstructor of Section 3.4 is shown in Figure 50. Curves are shown for additive white Gaussian noise levels of 0, 0.2, 1, and 2 radians squared. The aperture averaged mean squared phase error increases as the noise level increases.

Figure 51 shows a comparison between the simulated minimum variance and G & R least squares aperture averaged mean squared phase error as a function of noise and sampling parameter,  $\beta$ . The reference phase map was used to determine

the phase difference inputs used to estimate  $\langle \epsilon^2 \rangle$ . The variance of the additive white Gaussian noise was 0.2 radians squared. The aperture averaged mean squared phase error was simulated on the identical coarse sampling grid for both the minimum variance and G & R least squares reconstructors. The aperture averaged input phase variance is shown for reference (top line). In terms of  $\langle \epsilon^2 \rangle$ , the minimum variance reconstructor out-performs the G & R least squares reconstructor over the useful ranges of  $\beta$ .

Figure 52 compares the simulated aperture averaged mean squared phase error of the minimum variance and G & R least squares methods for an additive Gaussian noise variance,  $\sigma_n^2$ , of 1 radian squared. The results are plotted against the sampling parameter  $\beta$ . As expected, both the simulated minimum variance and G & R least squares aperture averaged mean squared phase errors are higher than for the no noise case and the  $\sigma_n^2 = 0.2$  case. The simulated aperture averaged mean squared phase error for the minimum variance method is lower than for the G & R least squares wavefront reconstructor for the values of  $\beta$  shown.

Finally, Figure 53 shows the results for the simulated aperture averaged mean squared phase error for an additive white Gaussian noise variance,  $\sigma_n^2$ , of 2 radians squared. The aperture averaged mean squared phase error for both the minimum variance and G & R least squares wavefront reconstructors is pointwise higher than the corresponding curves for lower noise values.

The performance of the minimum variance reconstructor under various noisy conditions was demonstrated. The theoretical aperture averaged mean squared phase error was presented as a function of noise and sampling parameter,  $\beta$ , for both the minimum variance and least squares methods. The simulated aperture averaged mean squared phase error was determined as a function of various noise levels and  $\beta$  values for the minimum variance and G & R least squares methods. In both theory and simulation the minimum variance reconstructor had a lower aperture averaged mean squared phase error than the corresponding least squares method.



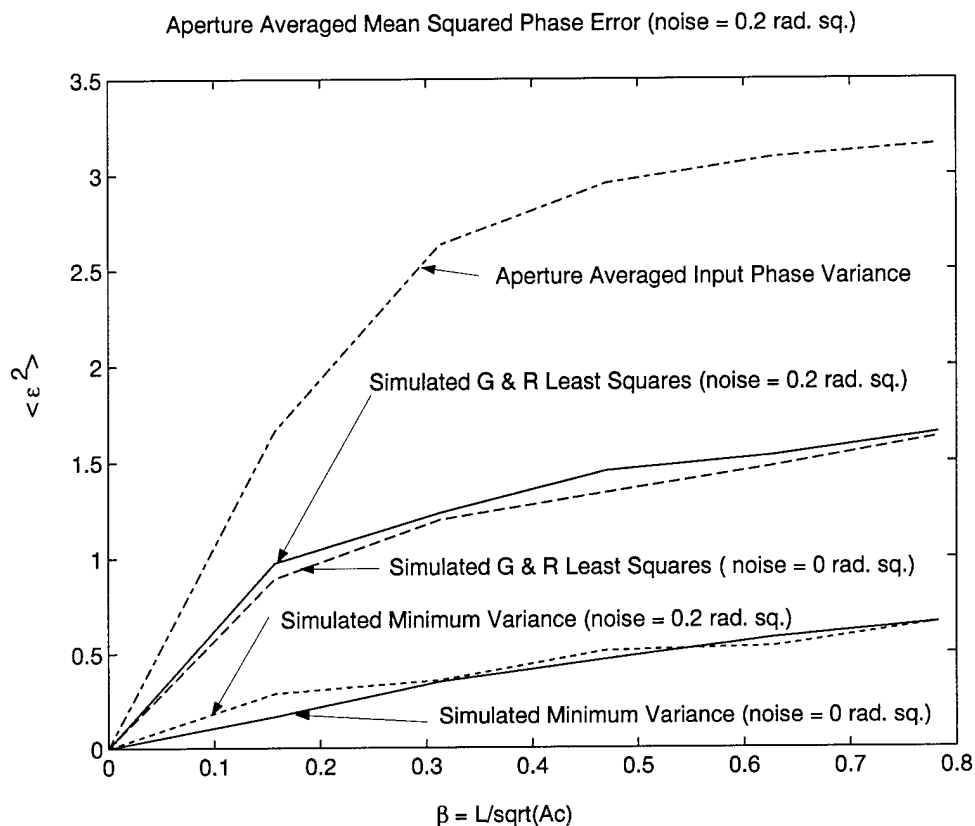


Figure 51. Simulated aperture averaged mean squared phase error for minimum variance and G & R least squares methods as a function of noise level and sampling parameter,  $\beta$ . Additive white Gaussian noise levels were 0.2 radians squared. The bottom solid line indicates the simulated aperture averaged squared phase error for the minimum variance reconstructor and no noise. The dashed line second from the bottom represents the minimum variance simulated aperture averaged mean squared phase error with  $\sigma_n^2 = 0.2$  radians squared. The third line from the bottom is the simulated G & R least squares results and no noise. The fourth line from the bottom shows the simulated performance of a G & R least squares reconstructor with the same noise variance as the minimum variance reconstructor. The top line shows the aperture averaged input phase variance for no noise.

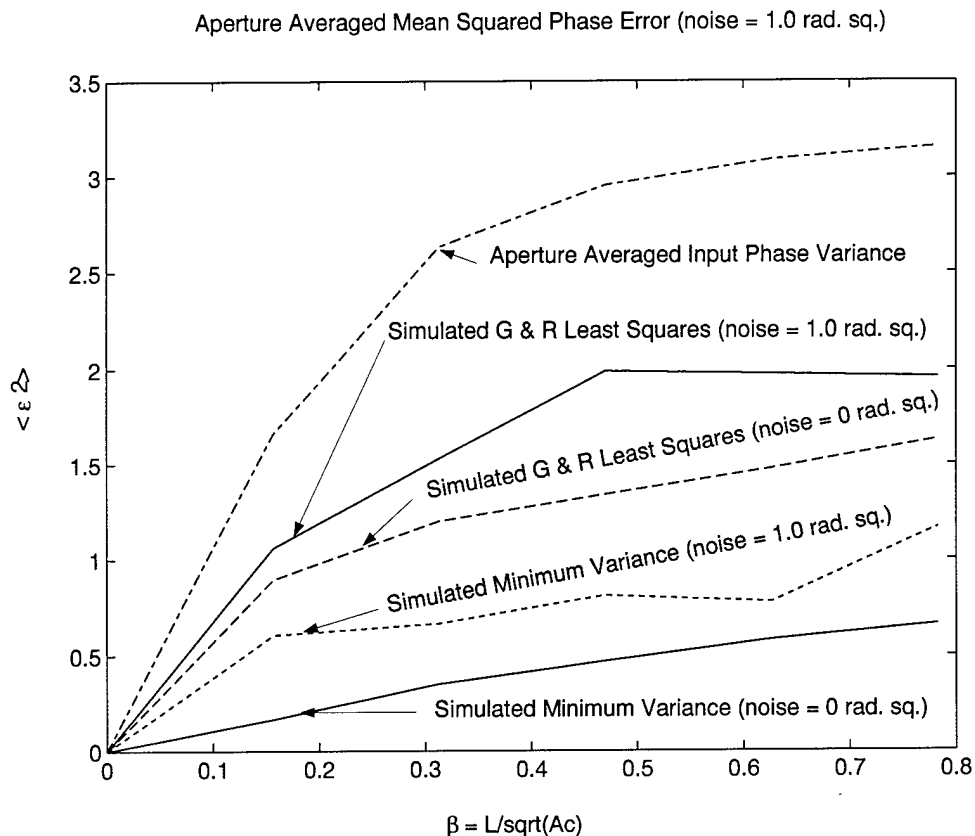


Figure 52. Simulated aperture averaged mean squared phase error for minimum variance and G & R least squares methods as a function of noise level and sampling parameter,  $\beta$ . Additive white Gaussian noise levels were 1.0 radians squared. The bottom solid line indicates the simulated squared error for the minimum variance reconstructor and no noise. The dashed line second from the bottom represents the minimum variance simulated aperture averaged mean squared phase error with  $\sigma_n^2 = 0.2$  radians squared. The third line from the bottom is the simulated G & R least squares results and no noise. The fourth line from the bottom shows the simulated performance of a G & R least squares reconstructor with the same noise variance as the minimum variance reconstructor. The top line shows the aperture averaged input phase variance for no noise.

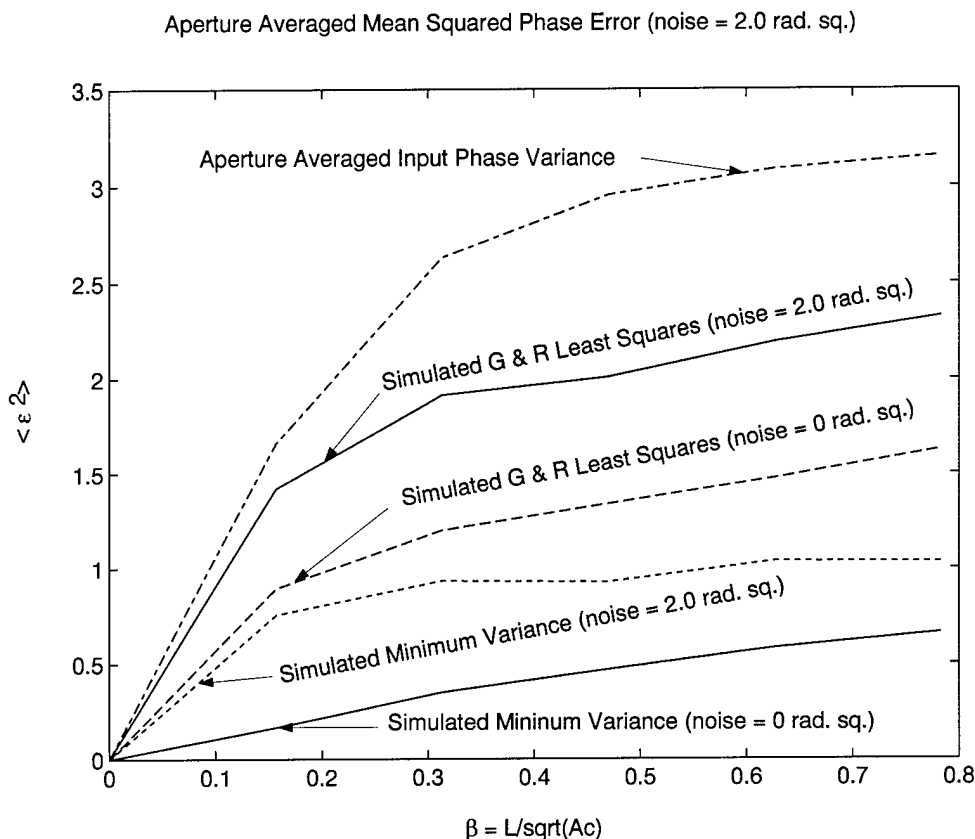


Figure 53. Simulated aperture averaged mean squared phase error for minimum variance and G & R least squares methods as a function of noise level and sampling parameter,  $\beta$ . Additive white Gaussian noise levels were 2.0 radians squared. The bottom solid line indicates the simulated squared error for the minimum variance reconstructor and no noise. The dashed line second from the bottom represents the minimum variance simulated aperture averaged mean squared phase error with  $\sigma_n^2 = 0.2$  radians squared. The third line from the bottom is the simulated G & R least squares results and no noise. The fourth line from the bottom shows the simulated performance of a G & R least squares reconstructor with the same noise variance as the minimum variance reconstructor. The top line shows the aperture averaged input phase variance for no noise.

#### 4.5 Summary

This chapter presented results on the performance of the minimum variance reconstructor for a variety of object classes. Throughout this chapter, the theoretical average reflectivity profile assumed to calculate the optimal reconstruction matrix,  $M_{jn}$ , was Gaussian with infinite spatial extent. In general, the simulated average reflectivity profiles were different than the assumed theoretical model. In Section 4.1, the simulated average reflectivity profile was a truncated Gaussian with spatial features. Objects which have surface profiles that are smooth on the scale of an optical wavelength were discussed and good reconstructions for a simulated doughnut and tri-bar object average reflectivities were demonstrated. Section 4.2 discussed a simple diffuse reflector such as a pair of random point sources. The separation of the simulated random point sources was equal to the  $e^{-1}$  width of the Gaussian average reflectivity profile used in the theoretical determination of  $M_{jn}$ . The random double point source object demonstrated the near diffraction limited resolution of the minimum variance reconstructor under noiseless conditions. A point of interest is that only 64 evenly spaced sample points were used in the measurement plane to determine the near diffraction limited image. Section 4.3 showed results for extended objects. For sampling reasons, a Gaussian reflected average reflectivity profile with infinite extent was modeled in the simulation. This section had an optimal match between the theory and simulation and no noise effects were included. The theoretical aperture averaged mean squared phase error was determined as a function of sampling parameter,  $\beta$ , for both the minimum variance and least squares methods. The least squares implementation discussed in Section 3.4 was used to do the theoretical comparisons. Simulated comparisons between the minimum variance and G & R least squares reconstructor were presented for various values of  $\beta$  and no noise. In both theory and simulation, the minimum variance wavefront reconstructor outperformed the corresponding least squares reconstructor. The last section illustrated the performance of the minimum variance reconstructor under sub-optimal condi-

tions. The simulated aperture averaged mean squared phase error was determined as a function of  $\beta$  for a simulated object with a truncated Gaussian average reflectivity profile. Some structure was added (  $\times$  and  $+$  object) to demonstrate that the reconstructor was able to reproduce surface features for diffuse scatterers. Variations in object average reflectivity of up to 63 percent (along the most distant points along the boundary of the object support) was shown to have negligible effect on the quality of the reconstruction of the  $+$  image. Mismatches between the expected object size and the actual object size were shown to have a small effect on the aperture averaged mean squared phase error. Finally, the aperture averaged mean squared phase error was determined as a function of the sampling parameter,  $\beta$ , for additive, white, Gaussian noise levels of  $\sigma_n^2 = 0, 0.2, 1.0$ , and  $2.0$  radians squared. The minimum variance reconstructor had a pointwise lower aperture averaged mean squared phase error than the corresponding least squares reconstructor for comparable noise values.

## *V. Conclusions*

A new wavefront reconstructor has been developed for a synthetic aperture coherent imaging system. The reconstructor uses atmospheric distortion free phase differences obtained from the Sheared Coherent Interferometric Photography (SCIP) technique discussed in Chapter II. The phase differences are used in a new minimum variance technique to estimate the 2D measurement plane phase. Key results of this work are reviewed in this chapter, conclusions are presented, and possible future directions for research in this area are discussed.

### *5.1 Results and Conclusions*

The minimum variance reconstructor was developed in chapter III and preliminary testing of the reconstructor was accomplished. The scaling and throughput (implementation of the linear algebra) of the minimum variance reconstructor was demonstrated by successfully reconstructing the measurement plane 2D phase map for an off-axis point source object. The statistical aspects of the minimum variance wavefront reconstructor were validated by comparing the fundamental equations in the reconstructor to numerical integrations in widely available mathematical software packages including MathCad and Mathematica. The good results from the throughput and statistical assessments, and the reconstruction of a simple deterministic object average reflectivity profile leads to the conclusion that the theoretical equations and their implementation in the minimum variance wavefront reconstructor are correct.

Measurement plane 2D phase maps were successfully reconstructed for (a) an optically smooth object with a doughnut average reflectivity distribution and (b) an optically smooth tri-bar object. The reconstructed phase maps for both cases had the character of low pass versions of the true phase. The images associated with the reconstructed phases were similar to the average reflectivity profile for the respective

objects. The good agreement between the true and reconstructed images leads to the conclusion that the minimum variance reconstructor can successfully reproduce images of optically smooth objects with spatial features.

A random double point source object was used to demonstrate the resolution of the minimum variance wavefront reconstructor. The term random point source refers to an object that is optically rough but has physical dimensions that are much smaller than the resolution of the optical system. The random double point source had two random point sources symmetrically spaced about the object plane origin. The separation of the points was set equal to the diffraction limited resolution of a 3 m by 3 m square collecting aperture in a coherent imaging system. The reconstructed image of the point sources for 100 independent image frame averages reproduced the gap between the sources. The peak-to-peak point separation of both the true and reconstructed images was 0.85 m. This separation is within 2 % of the theoretically determined diffraction limit of a 3 m by 3 m filled square aperture in a coherent imaging system. The FWHM measurement of the image corresponding to one lobe from the random double point source object was 0.42 m for the true image and 0.62 m for the reconstructed image. The accuracy of the measurement was  $\pm 0.025$  m. The resolution of the gap between the double point sources indicates that for only 8 equally spaced measurement plane samples in a given linear direction, the minimum variance wavefront reconstructor is capable of producing nearly diffraction limited images for the case of no noise.

An extended optically rough object with a Gaussian average reflectivity distribution was reconstructed for an object subtending  $0.4333 \mu\text{rad}$ . The reconstructed object appeared similar to the averaged coherent image formed by a 3 m by 3 m square aperture. The reconstructed field used SCIP phase difference information from an 8 by 8 point measurement grid to estimate the 2D phase map. The reconstructed phase map and the measurement plane field amplitude information were used to form the measurement plane reconstructed field. The reconstructed image

was obtained by averaging 100 reconstructed images in an analogous fashion as for the true image. The visual quality of the true and reconstructed averaged images combined with the low theoretical and simulated aperture averaged mean squared phase error for this object leads to the conclusion that the minimum variance wavefront reconstructor works for small, featureless random extended objects.

Several measurement plane 2D phase maps were reconstructed for differing object sizes. The reconstructed phase maps were compared to the true phase map obtained by unwrapping the reference phase with a 2D phase unwrapping utility. Favorable comparisons between the true and reconstructed phases were observed for sampling parameter,  $\beta$ , values in the range of  $\beta \leq 0.47$ . The sampling parameter,  $\beta$ , is defined as the sample spacing,  $L$ , divided by the square root of the coherence area of the object in the measurement plane,  $\sqrt{A_c}$ . For larger values of  $\beta$  the measurement plane sampling was no longer dense enough to reliably reproduce the true phase.

The theoretical and simulated aperture averaged mean squared phase error was determined as a function of  $\beta$  and compared with the theoretical and simulated aperture averaged mean squared phase error for the least squares reconstructor discussed in Section 3.4. Perfect agreement between the theory and simulation and no measurement noise was assumed. The simulated aperture averaged mean squared phase error was also compared to the simulated aperture averaged mean squared phase error for the G & R least squares wavefront reconstructor. The G & R least squares reconstructor represents a specific implementation of the class of conventional least squares reconstructors discussed in Section 2.2. In terms of the aperture averaged means squared phase error metric, the minimum variance reconstructor provides better performance than the corresponding least squares reconstructors over the useful range of  $\beta$ . Differences between the theoretical and simulated results are attributable to,

1. The finite (instead of infinite) number of averages used in approximating  $\langle \epsilon^2 \rangle$ .



2. Precision errors in calculating the measurement plane phase covariances. Individual phase covariances are accurate to the fourth decimal place. Processing limitations determined the precision of the phase covariances.
3. Small differences between the theoretical and simulated average reflectivity profiles. The theoretical average reflectivity profile was a Gaussian with infinite extent. The simulated average reflectivity profile was a Gaussian which was truncated at the boundaries of the object support (valid for Section 4.4 only).
4. The presence of branch cut and phase wrap discontinuities in the simulation. The theory used to develop the phase covariances does not predict branch cuts.

By relating the object coherence area to the physical dimensions of the object, the expected error can be determined in terms of object size and measurement plane sample spacing. Smaller objects and smaller sample spacings lead to lower expected aperture averaged mean squared phase errors.

An optically rough extended object with a Gaussian average reflectivity profile in accordance with equation (54) and spatial details resembling an  $\times$  was successfully reconstructed and shown to be nearly equivalent to the diffraction limited image produced by a 3 m by 3 m square collection aperture. For 100 image frames, the averaged coherent true image was, in accordance with equation (58), identical to the reconstructed image to within 3.65 %. Varying the object size in the average reflectivity profile in the simulation while holding the optimal reconstruction matrix,  $M_{jn}$ , constant was characterized in terms of the aperture averaged mean squared phase error. Variations in the magnitude of the object average reflectivity was shown to have negligible affect. The Gaussian average reflectivity profile given in equation (54) was used in the theoretical development of  $M_{jn}$  and a constant object average reflectivity profile resembling a  $+$  was used in the simulation process. The difference between the expected (theoretical) average reflectivity illustrated in equation (54) and the constant simulated average reflectivity was as high as 63 % at the tips of the  $+$  object and still a near diffraction limited image was produced. The maximum

pointwise difference between the diffraction limited image irradiance and the reconstructed image irradiance for the average reflectivity mismatched case was 8.24 %. From these results it is concluded that the minimum variance reconstructor is not highly sensitive to the average reflectivity model of the object.

Theoretical plots of the aperture averaged mean squared phase error were presented for both the minimum variance wavefront reconstructor and the least squares reconstructor discussed in Section 3.4. In the theoretical results, additive white Gaussian noise was incorporated into the measurement process. Plots of  $\langle \epsilon^2 \rangle$  versus  $\beta$  showed an increase in the expected squared error for increases in the noise variance,  $\sigma_n^2$ . Four separate curves were plotted corresponding to noise variances of 0, 0.2, 1, and 2 radian squared. Each subsequent curve had a pointwise higher value of  $\langle \epsilon^2 \rangle$  for every value of  $\beta$ . However, even for the highest noise variance ( $\sigma_n^2 = 2$ ), the maximum value of  $\langle \epsilon^2 \rangle$  was still less than the aperture averaged input phase variance of 3.2 radians squared. The minimum variance theoretical aperture averaged mean squared phase error was less than the theoretical least squares aperture averaged mean squared phase error for all values of  $\beta$  shown. Comparisons of the simulated aperture averaged mean squared phase error between the minimum variance and both least squares reconstructors (discussed in Sections 2.2 and 3.4) showed a corresponding lower aperture averaged mean squared phase error for the minimum variance wavefront reconstructor over the given values of  $\beta$ .

## 5.2 Contributions

The most important results obtained during the course of this research are listed below. The contributions are not listed in any order of precedence.

1. The minimum variance wavefront reconstructor is the first coherent wavefront reconstructor which uses statistical information (in the form of measurement plane phase covariances) to estimate the wavefront in the measurement plane of a synthetic aperture coherent imaging system. The impact of measurement

noise and imprecise knowledge of the object average reflectivity profile was evaluated.

2. The minimum variance reconstructor, unlike a conventional least squares reconstructor, allows for interpolation between reconstructed measurement plane phase estimates.
3. The performance of the minimum variance reconstructor in terms of the theoretical and simulated aperture averaged mean squared phase error is better than the performance of conventional least squares reconstructors.
4. The aperture averaged mean squared phase error is related to measurement plane sampling requirements and object dimensions through the sampling parameter,  $\beta = \frac{L}{\sqrt{A_c}}$  for a specific object. The quantity,  $L$  is the distance between sample points in the measurement plane and  $A_c$  is the coherence area of the object in the measurement plane.
5. A new least squares reconstructor was developed which provides for interpolation between reconstructed measurement plane phase estimates.

These results represent the highlights of the contributions made during the evaluation of the minimum variance wavefront reconstructor. The next section describes future areas of study identified during the course of this research.

### 5.3 *Future research directions*

The following list describes potentially beneficial areas of research related to the coherent imaging area. The topics described were identified during the course of this research and merit further consideration.

1. Development of a full field wavefront reconstructor. Determine the covariances of the real and imaginary parts of the measurement plane field and use the minimum variance formalism developed by Wallner to estimate the real and imaginary parts of the field. The inputs to the full field minimum variance

wavefront reconstructor can be the point irradiances on a measurement plane sampling grid. The measurement plane point irradiance is given by multiplying the real and imaginary parts of the measurement plane field by their complex conjugates. The field at any given sampling point can be described by circularly complex Gaussian random variables. The aperture averaged mean squared field error and the optimal reconstruction matrix can be determined in a similar fashion using the methods of Wallner [12]. Instead of requiring the measurement plane phase covariances, the covariances of all possible combinations of the real and imaginary part of the field are required. The advantage of the full field reconstructor is that the real and imaginary parts of the field are continuous. The full field reconstructor would not suffer from discontinuities and ambiguities ( $\pm m2\pi$ ) in the measurement plane 2D phase function.

2. Further investigate sampling requirements in the minimum variance wavefront reconstructor. The implementation of the minimum variance wavefront reconstructor needs to be optimized for speed. Use of table look ups, faster integration routines, and re-assessing the indexing scheme would lead to a faster version of the minimum variance reconstructor. The increase in speed would permit investigating the reconstruction of more spatially complicated objects.
3. Incorporate amplitude statistics in the minimum variance wavefront reconstructor. In the current minimum variance wavefront reconstructor, the amplitude estimates are assumed to be perfectly known. In actuality, the amplitude of the complex representation of the measurement plane field is also a random quantity and should be included in the estimation process.
4. Include the effect of finite pixel width in the measurement plane detection process. The interpolation feature of the minimum variance and new least squares elementary functions allows for modeling and assessing the performance of the reconstructor for detectors with finite dimensions such as Charge-Coupled Device (CCD) cameras. In a sparsely sampled aperture such as the coarse grid,

relay optics can be used to map measurement plane sample points to center pixel values on a CCD camera. The projection of the pixel into the measurement plane gives each measurement plane sampling element finite extent. The finite detector pixel widths will blur the estimates of the phase differences. The phase difference blurring introduces an error into the reconstruction process which needs to be characterized. Incorporating the effect of the finite dimensions of the measurement plane sampling elements requires integration over the measurement plane. The minimum variance and new least squares reconstructor readily permits this integration since the elementary functions are defined everywhere in the measurement plane. For a conventional least squares reconstructor as discussed in Section 2.2, either additional sampling is required or an interpolation feature needs to be added to allow the measurement plane integration.

5. Investigate the performance of the minimum variance reconstructor under low light level conditions.
6. Investigate extending the range of the detectable phase difference measurements in the SCIP technique to the region of  $\pm 2\pi$ . The extension of the range appears to improve the quality of the reconstruction. Trade-off studies between increased illuminator complexity and a potential relaxation of sampling requirements in the measurement plane can be accomplished.
7. Evaluate the performance of the minimum variance reconstructor for other techniques besides SCIP.

The above list describes some of the more interesting areas of research identified during the course of this work. The potentially most useful topic is the development of the full field wavefront reconstructor discussed in item (1). A specific implementation based on non-SCIP phase differences (phase differences which are sensitive to atmospheric aberrations) seems feasible.

## Bibliography

1. F. Roddier, "The effects of atmospheric turbulence in optical astronomy," *Progress in Optics*, vol. XIX, pp. 283-375, 1981.
2. C. S. Gardner, B. M. Welsh, and L. A. Thompson, "Design and performance analysis of adaptive optical telescopes using laser guide stars," *Proc. IEEE*, vol. 78, pp. 1721-1743, 1990.
3. J. H. Hardy, "Active optics: A new technology for the control of light," *Proc. IEEE*, vol. 66, pp. 78-87, 1978.
4. M. C. Roggemann, "Limited degree-of-freedom adaptive optics and image reconstruction," *Applied Optics*, vol. 30, pp. 4227-4233, Oct. 1991.
5. R. A. Hutchin, "Sheared coherent interferometric photography: A technique for lensless imaging," *Proc. IEEE*, vol. 2029, pp. 161-168, 1993.
6. D. C. Ghiglia and L. A. Romero, "Robust two-dimensional weighted and unweighted phase unwrapping that uses fast transforms and iterative methods," *J. Opt. Soc. Am. A*, vol. 11, pp. 107-117, Jan. 1994.
7. P. S. Idell and J. D. Gonglewski, "Image synthesis from wave-front sensor measurements of a coherent diffraction field," *Optics Letters*, vol. 15, pp. 1309-1311, Nov. 1990.
8. H. Takajo and T. Takahashi, "Least-squares phase estimation from the phase difference," *J. Opt. Soc. Am. A*, vol. 5, pp. 416-425, Mar. 1988.
9. S. Lowenthal and H. Arsenault, "Image formation for coherent diffuse objects: Statistical properties," *J. Opt. Soc. Am.*, vol. 60, pp. 1478-1483, Nov. 1970.
10. J. W. Goodman, *Topics in Applied Physics: Laser Speckle and Related Phenomena*, vol. 9, ch. 1, pp. 35-46. New York: Springer-Verlag, 1975. Edited by J. C. Dainty.
11. D. Middleton, *An Introduction to Statistical Communications Theory*. Cambridge: McGraw-Hill Book Company, Inc., 1990.
12. E. P. Wallner, "Optimal wave-front correction using slope measurements," *J. Opt. Soc. Am.*, vol. 73, pp. 1771-1776, 1983.
13. J. W. Goodman, *Statistical Optics*, ch. 7. New York, NY: Wiley-Interscience Publications, 1990.
14. D. G. Voelz, J. D. Gonglewski, and P. S. Idell, "Scip computer simulation and laboratory verification," *SPIE Proc. on Digital Image Recovery and Synthesis II*, vol. 2029, pp. 169-176, 1993.
15. D. L. Fried, "Least-squares fitting a wavefront distortion estimate to an array of phase-difference measurements," *J. Opt. Soc. Am.*, vol. 67, pp. 370-375, 1977.

16. R. H. Hudgin, "Wave-front reconstruction for compensated imaging," *J. Opt. Soc. Am.*, vol. 67, pp. 375-378, 1977.
17. B. R. Hunt, "Matrix formulation of the reconstruction of phase values from phase differences," *J. Opt. Soc. Am.*, vol. 69, pp. 393-399, 1979.
18. B. L. Ellerbroeck, "Comparison of least squares and minimal variance wavefront reconstruction," report no. tr-721r, The Optical Science Company, July 1986.
19. M. S. Scivier and M. A. Fiddy, "Phase ambiguities and the zeros of multidimensional band-limited functions," *J. Opt. Soc. Am. A*, vol. 2, pp. 693-697, May 1985.
20. J. W. Goodman, *Fourier Optics*, ch. 4. New York: McGraw-Hill, 1968.
21. A. Papoulis, *Probability, Random Variables, and Stochastic Processes*, ch. 10. New York, NY: McGraw-Hill, Inc., 1991.
22. B. M. Welsh and C. S. Gardner, "Performance analysis of adaptive-optics systems using laser guide stars and slope sensors," *J. Opt. Soc. Am. A*, vol. 6, pp. 1913-1923, 1989.
23. M. C. Roggemann, "Optical performance of fully and partially compensated adaptive optics systems using least-squares and minimum variance phase reconstructors," *Computers Elect. Engng.*, vol. 18, no. 6, pp. 451-466, 1992.
24. S. Wolfram, *Mathematica: A system for Doing Mathematics by Computer*. New York: Addison Wesley, 1991.
25. I. MathSoft, *Mathcad 4.0*. Cambridge, Mass.: MathSoft, Inc, 1993.
26. R. D. Hudson, *Infrared Systems Engineering*, ch. 8, pp. 310-314. New York: John Wiley and Sons, 1969.
27. D. L. Fried and J. L. Vaughn, "Branch cuts in the phase function," *Applied Optics*, vol. 31, pp. 2865-2882, May 1992.
28. D. K. C. Mac Donald, "Some statistical properties of random noise," *Proc. Cambridge Phil. Soc.*, vol. 45, p. 368, 1949.

| REPORT DOCUMENTATION PAGE  |   |  | Form Approved<br>OMB No. 0704-0188                      |  |
|--|---|--|---|--|
| Public reporting burden for this collection of information is estimated to average 1 hour per response, including the time for reviewing instructions, searching existing data sources, gathering and maintaining the data needed, and completing and reviewing the collection of information. Send comments regarding this burden estimate or any other aspect of this collection of information, including suggestions for reducing this burden, to Washington Headquarters Services, Directorate for Information Operations and Reports, 1215 Jefferson Davis Highway, Suite 1204, Arlington, VA 22202-4302, and to the Office of Management and Budget, Paperwork Reduction Project (0704-0188), Washington, DC 20503.   |   |  |   |  |
| 1. AGENCY USE ONLY (Leave blank)   |   | 2. REPORT DATE<br>26 MAY 95                                | 3. REPORT TYPE AND DATES COVERED<br>Final JUN 92-JUN 95 |  |
| 4. TITLE AND SUBTITLE<br>Optimal Wavefront Reconstruction For A<br>COHERENT DIFFRACTED FIELD   |   |  | 5. FUNDING NUMBERS                                      |  |
| 6. AUTHOR(S) WILLIAM WOLFGANG ARRASMITH<br><br>Advisor: Major Michael C. Roggemann   |   |  |   |  |
| 7. PERFORMING ORGANIZATION NAME(S) AND ADDRESS(ES)<br>AFIT/ENP<br>WRIGHT-Patterson AFB OH 45433  |   |  | 8. PERFORMING ORGANIZATION<br>REPORT NUMBER             |  |
| 9. SPONSORING/MONITORING AGENCY NAME(S) AND ADDRESS(ES)<br>Phillips Lab / LIMI<br>Kirtland AFB NM 87117  |   |  | 10. SPONSORING/MONITORING<br>AGENCY REPORT NUMBER       |  |
| 11. SUPPLEMENTARY NOTES  |   |  |   |  |
| 12a. DISTRIBUTION/AVAILABILITY STATEMENT   |   |  | 12b. DISTRIBUTION CODE                                  |  |
| 13. ABSTRACT (Maximum 200 words) In sheared coherent beam interferometric imaging, an estimate of the average reflectivity profile of the object can be computed from measurements of point-to-point phase differences in the far-field interference pattern and a suitable phase reconstruction technique. The phase difference information is encoded in the irradiance of three identical, shifted and superimposed spotted laser beam patterns. A minimum variance phase reconstruction technique is presented to estimate the phase of the field in the measurement plane from the phase differences and evaluate its performance. Prior knowledge of the phase covariance is used in the minimum variance reconstructor. Analytic calculations and computer simulations are used to evaluate phase reconstruction errors as a function of object coherence area and spatial sample spacing in the measurement plane. The performance of the minimum variance reconstructor is compared to two least squares implementations. Computer simulation is used to illustrate the performance of the minimum variance reconstructor in the presence of additive white Gaussian noise and estimation errors. |   |  |   |  |
| 14. SUBJECT TERMS<br>SCIP, Phase Estimation, Statistical Estimation,<br>Shearing Interferometer  |   |  | 15. NUMBER OF PAGES<br>143                              |  |
|  |   |  | 16. PRICE CODE  |  |
| 17. SECURITY CLASSIFICATION<br>OF REPORT<br>UNCLASSIFIED   | 18. SECURITY CLASSIFICATION<br>OF THIS PAGE<br>UNCLASSIFIED | 19. SECURITY CLASSIFICATION<br>OF ABSTRACT<br>UNCLASSIFIED | 20. LIMITATION OF ABSTRACT<br>UL                        |  |